The Design, Fabrication, and Magnetic Actuation of a Microactuator to Accomplish Propulsion and Large Deflection in Viscous and Elastic Environments

Briana Lee Fiser

A dissertation submitted to the faculty of the University of North Carolina at Chapel Hill
in partial fulfillment of the requirements for the degree of Doctor of Philosophy
in the Department of Physics and Astronomy.

Chapel Hill
2012

Approved by:

Dr. Richard Superfine

Dr. Michael Falvo

Dr. Greg Forest

Dr. Fabian Heitsch

Dr. Laura Miller

Abstract

BRIANA LEE FISER: The Design, Fabrication, and Magnetic Actuation of a Microactuator to Accomplish Propulsion and Large Deflection in Viscous and Elastic Environments
(Under the direction of Dr. Richard Superfine)

Biomimetics is the study of the structure and function of biological organisms, properties, or substances to inform or inspire the creation of artificial mimics. Nature's evolutionarily evolved answers to its own obstacles can become great solutions to our problems in the fields of physics, materials science, and engineering. The field of biomimetics has both led to technological advances and utilized biomimetic systems to glean knowledge about their biological inspirations. I have developed a single biomimetic system which both mimics a biological system well enough to inform biology and is capable of advancing technology. This biomimetic system is composed of novel core-shell microrods that closely mimic the size of biological cilia and generate fluid transport in both viscous and viscoelastic fluids. Complex biological processes such as the determination of left-right asymmetry in the vertebrate embryonic node and mucociliary clearance in the lung are dependent on the successful transport of fluids, both buffer-like and viscoelastic. A biomimetic system such as the one I have developed allows us to compare cilia-driven transport in both aqueous and viscoelastic fluids. In addition, I have used arrays of these core-shell microrods, comprising a flexible poly(dimethylsiloxane) core surrounded by a 100 nm shell of nickel, to assess the time evolution of fluid properties at the microscale, such as the formation of blood clots, which act to stem the flow of blood in the event of trauma or tissue damage. Using this

system as an assay for the onset of clot development results in clinically relevant clotting time measurements. I will discuss these applications for the use of this biomimetic cilia system, as well as the system's design parameters and the fabrication procedure.

Acknowledgments

This work could not have been completed without the knowledge and support of the group of faculty and students with whom I have worked in the fishbowl of Chapman Hall. My advisor, Rich Superfine, has taught me several of the most valuable lessons learned at Chapel Hill, one of which is how to always have fun with science. His energy and excitement about everything science is encouraging, and I hope to always have that same exuberance. Mike Falvo and Sean Washburn have also been great advisors during my time with the group, always willing to take a few minutes to answer questions or talk about data analysis. Also, thank you to Greg Forest for always taking an interest in the biomimetic systems I have developed and being positive in every interaction we have had.

As for the students, I will never work with a better group - Jerome Carpenter, Lamar Mair, Vinay Swaminathan, Ricky Spero, Kwan Skinner, and everyone else in NSRG. The sense of community and the eagerness of all of us to help each other and work together made it a wonderful place to go to work every day for the last five years. Jeremy Cribb was a lifesaver when it came to teaching me Matlab and how to code the first summer I joined the lab. Ben Evans and Adam Shields (also NSRGers) were my cilia co-conspirators. Ben spent his last summer with the group training me how to take his place (a difficult feat that no one could ever really accomplish), and Adam spent the next year teaching me everything he knew about cilia.

I am eternally grateful to my family and friends, who have constantly encouraged me throughout my life and most especially the last six years. Thank you to my mother for not only her strong support and confidence in me, but also her willingness to read through this dissertation more than once. To my father, I truly appreciate his making the twelve hour drive every summer to visit, but still understanding my need to stay in the lab until midnight taking data with a great sample. Thank you to my sister for not taking my graduate school frustrations too seriously and starting her own graduate career, and to Samantha Hammond, who began graduate school with me six years ago and will be hooded with me this spring, for her continued friendship and support. Finally, thank you to my husband Rip Fiser, for his constant and unwavering belief in my abilities. I cannot imagine how the last year especially would have been without him.

Table of Contents

List of Tables

List of Figures

List of Abbreviations

AAO	anodic aluminum oxide
APTT	activated partial thromboplastin time
ASL	airway surface liquid
CF	cystic fibrosis
CPD	critical point dry
DCM	dichloromethane
De	Deborah number
EDS	Energy Dispersive X-ray Spectroscopy
FFPDMS	ferrofluid-poly(dimethylsiloxane)
FFPDMS-NH_2	ferrofluid-aminopropylmethysiloxane-dimethylsiloxane
GUI	graphical user interface
HBE	Human Bronchial Epithelial
MSD	mean square displacement
NaOH	sodium hydroxide
NVP	nodal vesicular parcel
PBS	Dulbecco's Phosphate Buffered Saline
PCD	primary ciliary dyskinesia
PCTE	polycarbonate track-etched
PCL	periciliary layer
PDMS	poly(dimethylsiloxane)
PDMS-NH_2	aminopropylmethylsiloxane-dimethylsiloxane

PEG	poly(ethylene) glycol
POC	point of care
PT	prothrombin time
PVP	Poly(vinylpyrrolidone)
Re	Reynolds number
ROTEM	rotational thromboelastometry
TEG	thromboelastography
TIC	trauma induced coagulopathy
TF	tissue factor
tPA	tissue plasminogen activator
VHA	viscoelastic haemostatic assay
We	Weissenberg number

List of Symbols

α	angle of magnetic moment of rod
A	cross sectional area
b	damping coefficient
$\vec{B}$	applied magnetic field
$\vec{B}_T$	total applied magnetic field
$\nabla\vec{B}$	magnetic field gradient
δ	phase angle
d	diameter
η	dynamic fluid viscosity
E	elastic modulus
f	magnetic loading, volume fraction
f_{CS}	volume fraction of core-shell cilia
F_0	driving force magnitude
γ	damping factor
G'	storage modulus
G''	loss modulus
I	second moment of inertia
κ	curvature
k	spring constant
l, L	length
L_{Ni}	length of core-shell Ni tube

L_{PDMS}	length of core-shell pure PDMS segment
m	mass
$\vec{m}$	magnetic moment
$\vec{M}$	magnetization per unit volume
μ_0	permeability of free space
ν	kinematic fluid viscosity
ϕ	bend angle of a rod
ρ	density
ψ'	angle of magnetic field gradient
r	radius
$R, R(s)$	radius of curvature
τ, N	torque
t	Ni tube thickness
$U_A(\vec{B}_A)$	energy of applied magnetic field
U_B	magnetic energy
U_E	elastic energy
$U_I(\vec{B}_I)$	internal energy of the rod
$U_N(\vec{B}_N)$	magnetic field energy felt from neighboring rods
v	velocity
V	volume
ω	angular frequency
ω_0	characteristic angular frequency

Chapter 1

Introduction

Biomimetics is the study of the structure and function of biological organisms, properties, or substances to inform or inspire the creation of artificial mimics. The word was first coined by Otto Schmitt whose doctoral research in 1957 comprised the development of a device which mimicked a nerve's electrical actions (Bhushan, 2009). Schmitt was heard using the term 'biomimetics' as a substitute for 'bionics' when discussing the utilization of insights obtained from the study of biological phenomenon to develop unique systems which mimic that phenomenon (Vincent et al., 2006). The creation of biomimetic devices or platforms may be fueled by the desire for new technology or a simpler, more elegant answer to a common problem. Nature's evolutionarily evolved answers to its own obstacles can become great solutions to our problems in the fields of physics, materials science, and engineering.

Multiple examples exist in biomimetics where biology's inspiration has fueled a useful technological advance. One such example is velcro, invented by Swiss engineer George de Mestral in 1948 after a hunting trip with his dog. de Mestral's inspiration was a type of stubborn bur caught in his dog's fur. As he studied the burs under a microscope, he determined the cause of their "stickiness" to be the presence of tiny hooks at the end of

each spine. After several engineering attempts with different materials, nylon velcro was born.

A second example is the lotus leaf, with its superhydrophobicity, a property which has been studied in great detail and applied to various commercial products. A surface is considered hydrophobic if the static contact angle between the surface and a water droplet is greater than 90° and superhydrophobic if the contact angle is greater than 150°. The lotus leaf's structure, at the microscale, comprises bumps approximately 4 μm in size spread across the leaf's surface. The presence of these structures along with a hydrophobic wax-like coating, repels water and aids in the self-cleaning of the leaf. The properties of superhydrophobicity and self-cleaning are highly desirable in many instances, most especially in applications where biofouling, the accumulation of microorganisms or plants on a surface, is a hindrance. Biofouling on large ships or boats increases the vessel's drag in the water; building a vessel with an antifouling, or self-cleaning, surface would reduce drag, creating more fuel efficient vessels. Other applications which have been commercially produced are self-cleaning paints, windows, and roofing tiles (Bhushan, 2009).

A number of reviews expound upon the vast array of biological inspirations that have led to technological advances including everything from airplanes to special drag-reducing swimsuits (Bhushan, 2009; Vincent et al., 2006). However, the biomimetic system that mimics biology so well it can be utilized to inform or even answer the questions asked about its biological inspiration is rare, and even rarer still is a biomimetic system which can do both – inform biology and serve as a new technology. I have designed such a biomimetic system, and it is the design, fabrication, magnetic actuation, and application of

this system to both biology and technology which is the subject of this dissertation.

My biomimetic system is inspired by and seeks to inspire an appendage which is ubiquitous in nature – the biological cilium. Biological cilia are present in nearly every organ in vertebrates and are responsible for a multitude of different tasks including cell motility, fluid propulsion, mechanical sensing, and chemosensation, a task only recently attributed to cilia. In the last two years, ciliated cells in the human airway were found to express bitter taste receptors which localized along the length of cilia. The introduction of a bitter compound increased ciliary beat frequency thereby confirming the ability of airway cilia to sense noxious substances upon entrance into the lungs (Shah et al., 2009).

Biological cilia can be divided into two large classes: motile and non-motile. The difference between motile and non-motile cilia is the presence or absence of the motor protein axonemal dynein. A cilium's structure, also called the axoneme, may be either '9+0' or '9+2', the first number indicating the number of microtubular doublets around the periphery of the cilium and the second number indicating the number of microtubular singlets in the cilium's center. Motile cilia have axonemal dyneins attached to the microtubular doublets that walk on neighboring microtubules, resulting in the bend of the cilium (Satir and Christensen, 2008) and are responsible for a number of biological functions, including mucociliary clearance in the lung (Satir and Sleigh, 1990), the establishment of the left-right asymmetry in vertebrate embryos (Nonaka et al., 1998), the motility of sperm (Neugebauer et al., 1990), the transport of fertilized eggs to the uterus (Shi et al., 2011), and the flow of cerebrospinal fluid in the brain (Worthington and Cathcart, 1963). If typically motile cilia suffer from immotility, the consequences can be severe and include airway infections,

situs inversus, infertility, hydrocephalus, and death (Afzelius, 2004). Non-motile cilia are typically responsible for sensing applications, including smell, light perception, and flow sensing within the kidneys. If non-motile cilia are not formed correctly or incapable of performing their various functions, the consequences could include anosmia, blindness, or polycystic kidney disease, a disease which includes the development of large cysts on the kidneys (Pan et al., 2005; Satir and Christensen, 2008).

Part of my research has focused on the design, fabrication, magnetic actuation, and application of a biomimetic cilia system to develop a deeper understanding of motile biological cilia responsible for two functions in particular: (i) mucociliary clearance in the lung, and (ii) the development of left-right asymmetry during vertebrate embryogenesis. Both of these biological functions require motile cilia to propel fluid flow in a particular direction. For the lung, viscoelastic mucus must be propelled up and out of the lung by beating cilia to clear our lungs of pathogens. In the vertebrate embryo, a Newtonian fluid must be transported from the right side of the embryo to the left by beating cilia to establish the asymmetry of the embryo. The benefits of utilizing a biomimetic system to ask the questions which biology is currently asking are enormous. Biomimetic systems allow for the exploration of the impact of individual parameters on the system as a whole. How does altering the beat frequency affect fluid transport? How does a different fluid restrict or enhance the mobility of a cilium or alter the cilium's ability to transport that fluid? How does the beat shape of an array of cilia affect the velocity of transport? All of these questions can be answered with the use of my biomimetic cilia arrays, which consist of individual flexible and magnetic rods on the same scale as the biological system. Building a biomimetic array

of cilia with dimensions that are a true mimic of biological cilia is integral to answering these questions and more as fluid at the microscale is distinctly different from fluid at the macroscale.

The system I have designed consists of an array of individual rods that are ten microns tall and 0.55 μm in diameter, spaced approximately 7-10 μm apart. These rods are both flexible and magnetic, capable of deforming in response to an applied magnetic field. They are capable of performing various beat shapes, as all biological cilia do not beat in the same manner. Both the flexibility and magnetic property of a biomimetic cilium arises from the combination of materials utilized in the fabrication process. The use of a soft, elastic polymer poly(dimethylsiloxane) supplies biomimetic cilia with flexibility, and introducing a magnetic material, such as nickel or iron oxide, provides a convenient method of controlling the cilia array through the use of a magnetic field. By fabricating a novel core-shell structure, such that a single cilium consists of a polymer core with a nickel shell surrounding its upper portion, I have created an array of highly responsive rods capable of bending such that their tips contact the substrate to which they are attached. The highly responsive nature of these core-shell biomimetic cilia allows me to explore and inform the biological questions I posed previously, as even within fluids as viscous and elastic as mucus and sputum, I am able to actuate biomimetic cilia arrays, both detecting and measuring biomimetic cilia amplitude and the resulting cilia-driven fluid flow.

In addition to answering these biological questions, my research has focused on utilizing arrays of biomimetic cilia as a technological device for the measurement and quantification of fluid properties. The ability to detect and measure amplitude changes in highly

viscous fluids lends itself to a new application, one in which the motion of a single cilium is employed to monitor changes in the viscosity or elasticity of the fluid in which it sits. More specifically, this system, as an array of rods, shows potential as a technological advance in the world of point-of-care devices for measuring the coagulation of blood clots.

Blood clots form to stem the flow of blood from damaged blood vessels. If clotting occurs too slowly, increased bleeding or hemorrhaging may occur, and conversely, if clotting occurs too quickly, patients are at an increased risk of developing blood clots, which could impair the flow of blood within the veins. These two possibilities are only two in an entire class of bleeding or clotting disorders known as coagulopathies. Either of these scenarios may result in death as coagulopathies are a leading cause of morbidity in the world (Hess et al., 2008). One in four trauma patients admitted to the emergency room, which account for 90% of emergency room admissions, is admitted with a coagulopathy and has a corresponding four fold mortality increase (Hess et al., 2008; Niles et al., 2008). By monitoring the change in amplitude as a blood clot forms, biomimetic cilia arrays are capable of measuring the clotting time for blood, and as I will discuss, are more sensitive to the onset of blood clotting than traditional coagulation assays.

Statistics such as these indicate the necessity of diagnostic tests with the ability to rapidly assess clot-related parameters for the treatment of patients suffering from trauma. Several such diagnostic tests are currently on the commercial market; however, these tests are not packaged in a portable way such that they may be used at the location of the patient directly after injury is suffered. Immediate diagnosis of a coagulopathy is necessary to avoid treatments which may aggravate the coagulopathy and worsen patient symptoms.

Devices capable of transport to the site of the patient are called point-of-care devices, and no such point-of-care devices currently exist for monitoring blood coagulation. Due to the nature of the fabrication process for my biomimetic cilia arrays, the size of the array can very easily be varied from one square millimeter to sheets as large as the size of the equipment utilized in the fabrication process. As such, a device can be constructed to fit in the palm of one's hand to maximize transportability of the diagnostic test.

1.1 Organization of the Thesis

I begin this thesis with a chapter on the biological cilium within the context of mucociliary clearance and embryogenesis. The biological cilium is an amazing structure, and as the majority of my work has been designing and fabricating a biomimetic system to better understand biological cilia, I will start by giving the reader a more thorough understanding of the inspiration for this work. In the third chapter, I will discuss the design parameters that are considered when fabricating an array of rods, as the rods must be both highly flexible and highly magnetic to maximize their response to an applied magnetic field in fluids as viscoelastic as mucus and sputum. Increasing magnetic content to increase responsiveness typically causes a corresponding increase in stiffness such that the rod becomes less responsive. Devising the core-shell structure, as I describe in Fiser et al., a prepared manuscript detailing the design and fabrication of these biomimetic cilia, is a smart method to separate, as much as possible, the contributions of the magnetic content to the stiffness of the rod (Fiser et al., 2012).

In Chapter 4, I will detail the fabrication process of biomimetic cilia for three dif-

ferent types of materials: maghemite ferrofluid-poly(dimethysiloxane) (FFPDMS), magnetite ferrofluid-poly(dimethylsiloxane) (FFPDMS-NH_2), and poly(dimethylsiloxane) core - nickel shell. The first two materials are suspensions of magnetic nanoparticles within a polymer matrix, and the third is a core-shell structure. FFPDMS cilia were developed prior to my joining the lab by Ben Evans and Adam Shields and are discussed in Evans et al., 2007. However, these cilia have been utilized in some experiments discussed in both this thesis and the publication Shields, Fiser, et al., 2010. In addition, the fabrication process for FFPDMS cilia is similar to the process I have devised for FFPDMS-NH_2 and core-shell biomimetic cilia.

A second material utilized in the fabrication of biomimetic cilia is FFPDMS-NH_2, though these cilia were not used in experiments. The composite material is an improvement upon FFPDMS; rather than a simple suspension of nanoparticles within a polymer matrix, individual nanoparticles in FFPDMS-NH_2 have polymer strands adsorbed onto their surfaces, a process described in Evans, Fiser, et al., 2012. This adsorption of polymer onto nanoparticle prevents aggregation, thereby allowing for a slightly higher magnetic content within each cilium without an appreciable increase in stiffness, generating larger rod responses. The third material, poly(dimethylsiloxane) core - nickel shell, is an improvement on both FFPDMS and FFPDMS-NH_2, as the polymer and magnetic material are separate and thus an increase in magnetic content has little effect on the flexibility of the cilium. Core-shell cilia are capable of actuating in highly viscoelastic fluids, a feat which could not be accomplished by FFPDMS cilia. Because of this, core-shell cilia are ideal actuators for exploring viscoelastic fluid transport, which I discuss in Chapter 6.

After detailing the fabrication process for biomimetic cilia, Chapter 5 explores various techniques for cilia actuation. The beat shape employed to address the biological questions I have posed in this Introduction (which will be addressed in Chapter 6) is called the 'tilted conical beat' and is performed by vertebrate nodal embryonic cilia. The beat shape employed in the new technology capable of measuring viscoelastic fluid properties and blood coagulation (which will be addressed in Chapter 7) is called the 'linear' beat and is a beat shape performed by lung epithelial cilia.

Before presenting the results and discussion for biomimetic cilia-driven fluid flow, in the beginning of Chapter 6, I will provide a brief overview of fluid flow at the microscale and discuss the concept of the Reynolds number and the fundamental equation of motion for fluids, the Navier-Stokes equation. Various solutions to the Navier-Stokes equation for both purely viscous and viscoelastic fluids will be examined as the solutions are utilized to describe fluid motion driven by an array of biomimetic cilia. After the introduction to microhydrodynamics, Chapter 6 is broken down into two further parts: aqueous fluid transport and viscoelastic fluid transport. Section 6.2 describes the fluid flow above and below biomimetic cilia tips in a purely viscous fluid as well as the implications I draw from these results for both biology and technology. For biomimetic cilia-driven viscoelastic fluid flow, Section 6.3 considers the viscoelastic fluid agarose, which is used in experiments, the comparison of flow between a viscous and viscoelastic fluid, and again, the implications of these results for biology and technology.

Finally, in Chapter 7, I move from discussion of the biomimetic cilia array as a platform to study biology to the utilization of biomimetic cilia as a new technology with the

potential for commercialization. Before applying biomimetic cilia arrays as measuring devices for the quantification of the viscous and elastic components of a fluid, and especially before arrays become available as commercial point-of-care devices, more research must be performed. I discuss this future research in the end of Chapter 7.

Chapter 2

The Biological Cilium

Biological cilia can be motile or non-motile, a determination made by the presence or absence of axonemal dynein motor proteins which allow them to bend. The biological cilia I seek to mimic, those responsible for mucociliary clearance in the lung and the development of left-right asymmetry during vertebrate embryogenesis, are both motile and possess axonemal dyneins; however, each cilium's internal structure is distinctly different. The internal structure of a cilium is called the axoneme, and it stems from the basal body, a structure anchored to the cell's surface by the basal foot. The delineation for the different internal structures is based on whether or not the cilium is a '9+2' structure or a '9+0' structure. Initially only 9+2 cilia were considered motile and 9+0 cilia, or primary cilia, were assumed to be non-motile; however, with the discovery of nodal embryonic cilia, which are motile and have a 9+0 ultrastructure, cilia are more often described as motile or non-motile than '9+0' or '9+2' (Satir and Christensen, 2008). Both cilium types consist of nine outer doublet microtubules that extend along the length of the cilium. In addition to these nine doublets, the 9+2 cilium contains two microtubule singlets in the axoneme's center. Figure 2.1 depicts a schematic of the cross-section of a 9+2 cilium's axoneme (Fauci and Dillon, 2006).

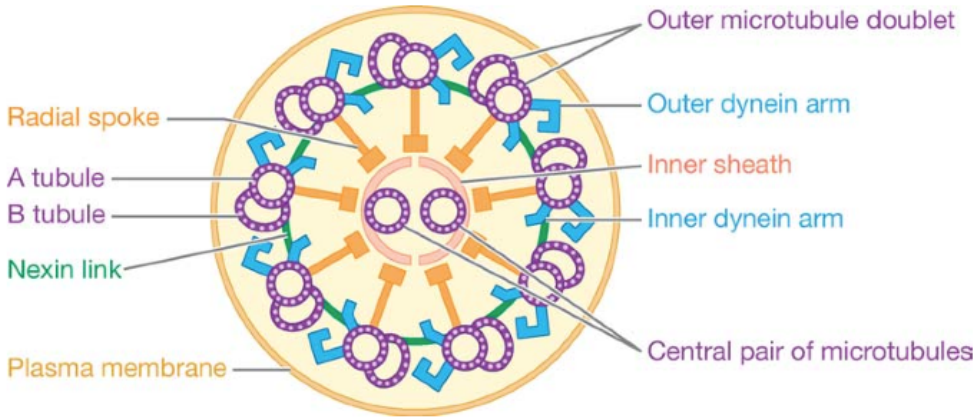

Figure 2.1: Reprinted from Fauci et al. (2006). Schematic of the axoneme for a 9+2 cilium. The significant difference between 9+2 and 9+0 cilia is the presence of the central microtubules (Fauci and Dillon, 2006).

The nine outer microtubule doublets are connected by nexin links, preventing them from exhibiting motion with respect to a microtubule neighbor. In addition to these links, dynein arms are present on each microtubule doublet. The motion of these dynein arms is driven by ATP, which causes them to walk on the surface of a neighboring microtubule. This walking produces the bending motion of a cilium. Four doublets on one side operate to produce the effective stroke, and five doublets on the other side operate to produce the recovery stroke. The effective stroke occurs in the direction of fluid motion, and during the recovery stroke, the cilium is typically close to the cell surface. Dynein arms come in two sets: the inner dynein arms which are thought to control the beat shape and the outer dynein arms which are thought to control the beat frequency (Fauci and Dillon, 2006; Satir and Christensen, 2008).

In the 9+2 axoneme, the outer nine microtubule doublets are linked to the central pair of singlet microtubules by radial spokes. These radial spokes and central pair of singlets are not present in 9+0 cilia. Because of these structural differences, the motion of 9+2 cilia

such as those found in the lung and 9+0 cilia such as those found in the embryonic node is markedly different. The radial spokes in 9+2 cilia serve to reinforce the structure of the cilium and likely contribute to the planar shape of the 9+2 beat. In 9+0 cilia, the lack of microtubules in the central region likely contributes to the conical shape of the 9+0 beat.

2.1 Bronchial epithelial cilia

Bronchial epithelial cilia, with a 9+2 ultrastructure, are primarily responsible for filtering and removing pathogens from the lung in order to prevent infection and illness. This complex process of clearing the lung is called mucociliary clearance. Lining the lung's conducting airways are cilia and the airway surface liquid (ASL), a layered fluid composed of a watery-like periciliary layer (PCL) and the viscoelastic fluid mucus, as illustrated in Figure 2.2A. The side of the mucus layer not in contact with the PCL is exposed to air. Human bronchial epithelial cilia are typically 7 μm tall, 250 nm in diameter, and grow in patches on the apical surface of the cell, as shown in Figure 2.2B and C. The PCL in which cilia sit is also approximately 7 μm high. In a healthy system, mucus, which has been secreted by goblet cells, traps inhaled contaminants and is transported out of the airway by contact with the beating cilia tips (Boucher, 2004).

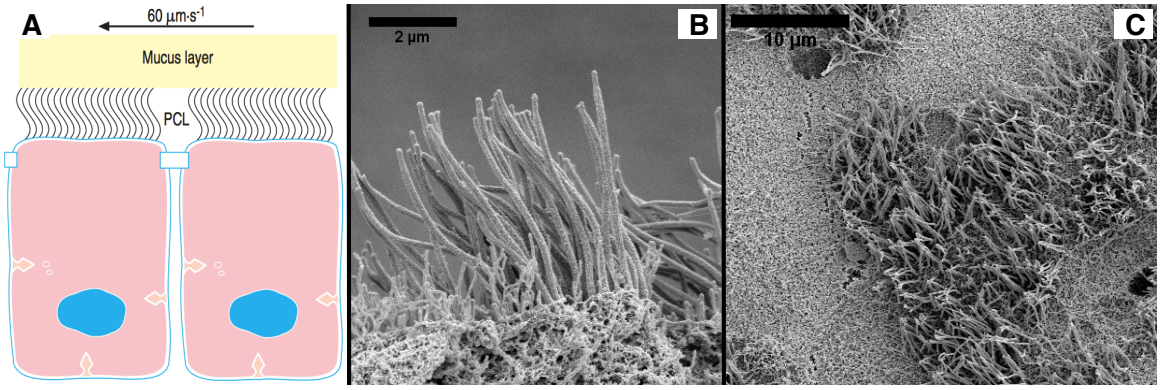

Figure 2.2: (A) Reprinted from Boucher et al. (2004). Schematic of cells in the lung. The cilia sit in a layer of fluid called the PCL, above which is the mucus layer (Boucher, 2004). (B-C) Scanning electron micrographs of human airway cilia, which are typically 7 μm tall and 250 nm in diameter. Lung epithelial cilia grow in patches on the apical cell surface.

Healthy airway cilia beat with an effective stroke, in which a cilium straightens vertically, followed by a recovery stroke, in which bending occurs and the cilium remains near the cell surface. This beat is almost entirely planar, and the effective stroke occurs in the direction of fluid motion, driving the fluid upward and out of the lung. This asymmetry in the cilium's beat shape is critical for the net transport of mucus out of the lung, as the cilia exist in a low Reynolds number environment where inertia plays no role.

The mechanism of this transport, however, is still poorly understood. There remain many open questions concerning interactions between cilia and the mucus layer. When cilia come into contact with the mucus layer during the effective stroke, what mechanical interactions occur? The mucus layer in the upper airways is thought to begin at the cilia tips and extend 15-20 μm above (Boucher, 2004). Within the airways, does this entire layer move? Must the entire layer of mucus move to clear our lungs of pathogens? My biomimetic cilia system is poised to answer these questions.

A number of disorders exist which can significantly hamper the mucociliary clearance

process, two of which are cystic fibrosis (CF) and primary ciliary dyskinesia (PCD). CF is essentially a disease caused by the failure of the mucociliary process, as patients are born with healthy lungs, but over the years acquire bacterial infections within their airways. Normal functioning of the mucociliary process is dependent on a number of factors including regulation of the PCL height. Without the PCL, cilia are immersed in mucus and become inefficient at clearing mucus from the lungs. Patients with CF suffer from a depleted PCL, resulting in a much-thickened mucus, and the mechanical process of mucociliary clearance no longer works effectively to clear the lungs of pathogens (Boucher, 2004). Biomimetic cilia immersed in a viscoelastic fluid such that the fluid fills the space throughout and above the cilia layer (an experiment I discuss in Section 6.3) could contribute to our understanding of this clearance inefficiency. In this experiment, the rate of net transport of the viscoelastic fluid was determined to be $1/12$ that of buffer, indicating a lack of clearance. Before interpreting and applying results such as these constructively to the biological system, more experiments would be needed to further elucidate the mechanical interaction between the cilium and the viscoelastic fluid as a function of viscoelasticity. In addition, as transport rates may vary in the presence of a layered fluid, it would be informative to investigate the effect of different layer thicknesses on transport. Again, the biomimetic cilia system is poised to contribute insight to these biological phenomena.

A second disorder that hampers mucociliary clearance is primary ciliary dyskinesia, which affects the assembly or function of axonemal dynein, leading to a change in the beat of cilia including the potential for complete impairment of the beat. Patients who exhibit PCD may suffer a number of problems other than impaired mucociliary clearance,

including male infertility and hydrocephalus (Satir and Christensen, 2008).

The linear beat shape employed by airway cilia is mimicked by biomimetic cilia with the use of a passing permanent magnet (described in Section 5.2.1), as biomimetic cilia are magnetic and seek to align themselves with the direction of an applied magnetic field. However, they are currently incapable of accurately mimicking the complexity of the beat shape exhibited by biological airway cilia; biomimetic cilia act as stiff projections from the substrate.

2.2 Vertebrate embryonic nodal cilia

The second biological cilium mimicked by biomimetic cilia is the vertebrate embryonic nodal cilium. The human body has three different axes – the anterior-posterior axis, the dorsal-ventral axis, and the left-right axis – which are determined during the course of embryogenesis. The anterior-posterior and dorsal-ventral axes are determined randomly, though perpendicular to one another. The left-right axis is the final axis to be determined, and it must be determined with respect to the other two axes. Vertebrate embryonic nodal cilia, with a 9+0 ultrastructure, play a vital role in determining this left-right axis, which refer to the left and right sides of a vertebrate embryo, during embryogenesis (Hirokawa et al., 2009). They produce a leftward flow of extraembryonic fluid in the ventral embryonic node which is critical for proper determination of the left-right axis of the embryo. A conservation of this leftward flow has been shown among multiple species, including the rabbit, medakafish, and mouse (Okada et al., 2005).

Embryonic nodal cilia are located within the embryonic node, a recessed pit on the

ventral side of the embryo. Figure 2.3 depicts the embryonic node and nodal cilia of a mouse. The node comprises a number of cells, each with a single cilium projecting from its surface. These nodal cilia are approximately 5 μm long and 300 nm in diameter. Because their ultrastructure is 9+0, they lack a central pair of microtubules and thus do not employ the planar beat exhibited by 9+2 cilia. Embryonic nodal cilia employ the 'the tilted conical beat', a conical beat that orbits about a tilted axis, typically tilted 40° from the vertical (Hirokawa et al., 2009). The cilium is most efficient at propelling fluid at the top of its beat, as when the cilium passes near the cell surface, a no-slip boundary condition is in play. In theoretical treatments, this tilted axis of rotation is critical to the production of directional flow, as in low Reynolds number environments where viscous forces dominate over inertial forces, asymmetry is critical in producing net displacement (Cartwright et al., 2007; Smith et al., 2008).

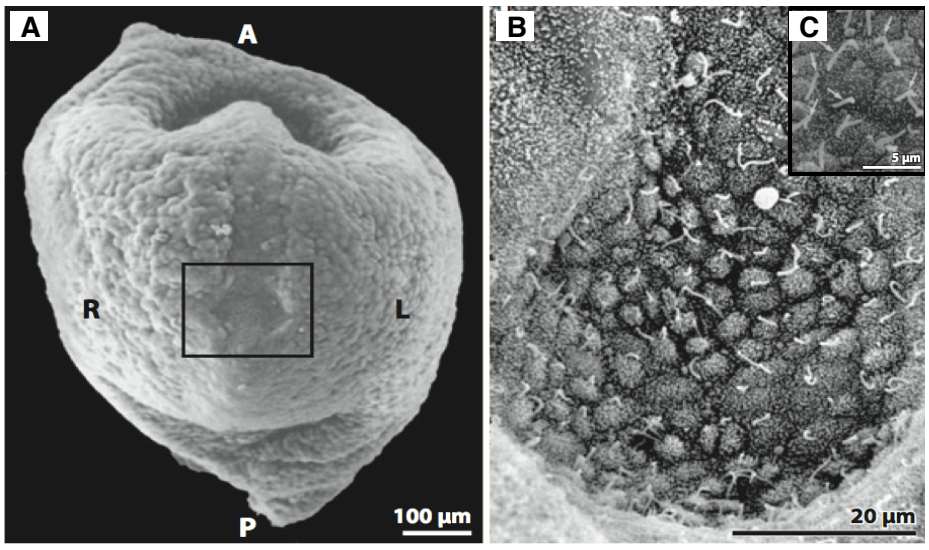

Figure 2.3: Reprinted from Hirokawa et al. (2009). Scanning electron micrographs of a mouse embryo. (A) View of the ventral side of a mouse embryo at 7.5 days post-coitum. *A* indicates the anterior side of the embryo, *P* is the posterior side, *R* is the right side, and *L* is the left side of the embryo. (B-C) Magnified views of the nodal pit (Hirokawa et al., 2009).

The leftward driven fluid flow controls determination of the left-right axis, a result discovered in 2002, when application of an external fluid flow produced predictable left-right axes (Nonaka et al., 2002). However, the method through which this mechanical flow is converted into a chemical signal remains unknown. The current hypothesis relies on the presence of nodal vesicular parcels (NVPs), membrane-sheathed particles which were recently discovered within the node. NVPs are hypothesized to be released from the cell surface, transported leftward within the node carrying morphogens, and ruptured upon contact with cilia or the left nodal wall, leading to a morphogen gradient (Tanaka et al., 2005). Biomimetic cilia arrays are capable of replicating the tilted conical beat employed by nodal cilia. With this beat shape, we have explored biomimetic cilia-driven flow in fluid of a similar viscosity to fluid in the node (Section 6.2), and our experiments support the establishment of a long range chemical gradient by cilia-driven flow. These results are presented in Shields, Fiser, et al., and this biomimetic system is primed for experiments which delve deeper into this hypothesis (Shields et al., 2010).

The leftward flow produced by cilia specifies the location of the heart and organs within the body, and thus in animals that lack nodal cilia, the location of these organs is random. In 99% of the human population, the heart is located on the left side of the body, and the liver is on the right. Situs inversus totalis is a condition in which the heart is located on the right side of the human body and the liver on the left, in essentially a mirrored replica of healthy individuals (Hirokawa et al., 2009). The exact mirroring of organ locations is unlikely to cause complications; however, nearly half of all patients who suffer from situs inversus totalis also suffer from Kartagener syndrome, which is characterized by bronchiectasis and

sinusitis. In general, these individuals exhibit symptoms associated with immotile-cilia syndrome (Afzelius, 2004).

The ubiquity of the cilium as well as the hugely damaging impact improperly functioning cilia have on the quality of human life make the cilium an ideal candidate for the construction of a biomimetic cilia system. The following chapter details the design of such a biomimetic system.

Chapter 3

Designing the Ideal Actuator

Responsive micro- and nanostructures are critical to the future of many technologies due to their uses as sensors and actuators, providing means for interactions between a system and its environment. Technologies at the micro- and nanoscale in general are revolutionizing the future of electronics and devices, requiring less in the way of materials. This equates to lower fabrication costs, and having the benefit of easy dissemination due to their size leads to a potentially higher impact on human lifestyles globally. Micro- and nanoscale actuating structures specifically provide precise control and manipulation in small length scale environments (Sahu et al., 2010). Magnetically driven actuation of these micro- and nanoscale actuators is particularly appealing because it has the potential to achieve large displacements without internal on-chip power sources or wires.

To design the ideal magnetic microactuator, it is important to understand the competition between magnetic and elastic forces within an actuator. An applied magnetic field produces a torque on the actuator which may result in a deflection provided the elastic modulus of the actuator is not so large such that the elastic energy is much greater than the energy supplied to the actuator through the magnetic field. The optimal magnetic loading for a given geometry which will yield a responsive actuator with some flexibility must be

determined. Figures of merit for such a determination have been developed by both Cebers et al. (Cebers, 2005) and Evans et al. (Evans, 2008; Evans and Superfine, 2011). I will discuss the latter model, modifying it to apply to core-shell actuators in addition to the homogeneous actuators for which it was created. It determines the maximum bend angle an actuator can achieve by minimizing the sum of an actuator's elastic energy, 'field energy', and 'gradient energy', where the field energy refers to the magnetic torque on the rod and the gradient energy refers to effect of the magnetic field gradient on the rod. This model considers only the static responsiveness of an actuator, or steady-state maximum amplitude achieved at an applied force. The dynamic responsiveness, or actuator amplitude at an applied force, oscillating with a given frequency, is an additional factor to consider when designing a microactuator. Many of the artificial cilia structures I will describe in Section 3.1 suffer from limited static and/or dynamic responsiveness. There exists an inherent limitation to the static responsiveness of micron-sized actuators in their small volumes and thus only limited driving forces may be applied. The small actuator volume also limits the dynamic responsiveness as does the presence of strong viscous damping in air or liquid environments. A basic treatment of artificial cilia-like structures as overdamped, driven harmonic oscillators demonstrates a need to maximize both static and dynamic responsiveness in actuator design.

We model our artificial cilia as slender cantilevered rods; thus, after giving a brief overview of current microactuators, I will discuss the mechanical model of artificial cilia as slender cantilevered rods, a model which combines the beam equation and the equation for a driven, overdamped harmonic oscillator. Assuming small angle deflections, these equa-

tions together serve as a basic model to understand cilia amplitude in a dynamic context in a purely viscous fluid. Chapter 7 expounds upon the application of this model to data taken in fluids with different viscosities. Following the discussion of dynamic responsiveness, which does not assist in the determination of material parameters, I will utilize Ben Evan's energy minimization model and the relationship for magnetic torque on a rod-shaped actuator to determine the appropriate magnetic and elastic material parameters which will maximize the static responsiveness of an actuator. In addition, because I am designing an array of microactuators with higher aspect ratios (length/diameter), adhesive forces play a significant role and must be considered as they contribute to both ground collapse and lateral collapse of the microactuators against one another. All of these characterizations will contribute to a better understanding of the parameter space for an ideal microactuator.

3.1 Current microactuators for use as artificial cilia

The design of actuators at the microscale has garnered much interest in the literature in the last five years especially. The biological cilium has been the inspiration for many of these microactuators, as it is a micron-sized actuator with the capacity to perform a large number of functions including the mixing and pumping of fluids and chemical sensing. With the increased demands for new microfluidic technologies that facilitate the study of small volumes of fluids within sub-millimeter sized channels, new methods must be devised for the manipulation of these fluids at this small scale. Artificial cilia have been developed as an answer to fluidic manipulation need and are often responsible for mixing and pumping in microfluidic settings. Experimental fabrication of cilia-like actuators has been explored

in depth, and many actuation techniques have been employed including electrostatics (den Toonder et al., 2008), the use of visible and UV light (van Oosten et al., 2009), SEM electron beams (Pokroy et al., 2009), PZT microstages (Oh et al., 2009; Oh et al., 2010), electromagnets (Fahrni et al., 2009b), and permanent magnets (Shields et al., 2010; Fiser et al., 2012).

I will address these different actuation methods in the following sections, but first, note that I refer to these microactuators as "artificial" cilia and not "biomimetic" cilia, as many of them do not accurately replicate or mimic their biological inspiration with respect to actuator size, beat shape, or drive frequency. Most of the artificial cilia I describe here are hundreds of microns in at least one dimension and are typically driven at tens of hertz. These differences in scale and actuation mean artificial cilia are capable of faster fluid transport and more efficient fluid mixing, and many of the artificial cilia below do drive fluid transport more rapidly than my arrays. However, the scale, beat shape, and driving frequency of my core-shell cilia arrays closely replicate the biological cilia system, and thus I use the term "biomimetic" to describe my system. In addition, of the present artificial cilia systems, few have been shown to produce fluid flow in Newtonian fluids and none have indicated flow in a viscoelastic fluid.

3.1.1 Actuation with electrostatics

In 1997, Suh et al. created thin-film artificial cilia by layering polyimides with different coefficients of thermal expansion onto aluminum electrostatic electrodes. The combination of polyimides and electrodes produced thin-film cilia capable of achieving large deflection

and lifting sizable loads. Each actuator consisted of four paddle-like structures ~430 μm long, each capable of 95-125 μm displacements and lifting loads as large as 500 mg (Suh et al., 1997).

In 2008, den Toonder et al. described an electrostic artificial cilium 100 μm wide by 20 μm long, consisting of a 1 μm layer of polyimide and a 20 nm conductive layer of chromium. These cilia were constructed on an indium tin oxide (ITO) electrode to which a voltage was applied at a given frequency, causing the cilium to curl and uncurl. At a driving frequency of 50 Hz, these large cilia generated fast pumping and mixing. However, because of the paddle's fast actuation speed, the local Reynolds number around each cilium was greater than one, creating an environment distinctly different from the low Reynolds number ($\sim 10^{-3}$) in which cilia live (Khatavkar et al., 2007; den Toonder et al., 2008).

3.1.2 Actuation with UV-Visible light

In 2009, van Oosten et al. introduced the first light-sensitive artificial cilia constructed with liquid-crystalline polymers. Liquid-crystalline polymers are highly ordered polymers that change shape when their molecular order is altered and are capable of exhibiting large deformations in response to many different types of stimuli including light, heat, and the chemistry of their environment. By mixing crystalline polymers with azobenzene dyes, which assist with shape deformations due to light exposure, van Oosten et al. created liquid-crystalline actuators 1 mm long by 100 μm wide by 20 μm thick capable of bending approximately 50° when exposed to ultraviolet light. Figure 3.1 depicts a side view of the actuation caused by exposure to ultraviolet light. These liquid crystalline cilia were

fabricated using an inkjet deposition method where the dye is deposited directly onto a layer of polyimide (van Oosten et al., 2009).

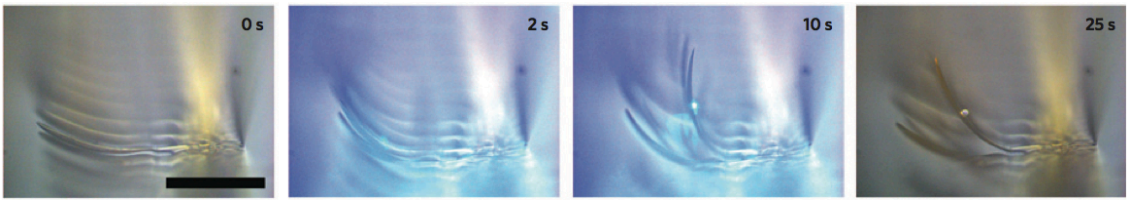

Figure 3.1: Reprinted from van Oosten et al. (2009). Liquid-crystalline artificial cilia actuated by exposure to ultraviolet light. Artificial cilia are 1 mm long by 100 μm wide by 20 μm thick. The scale bar is 500 μm (van Oosten et al., 2009).

3.1.3 Actuation with a piezo stage

Oh et al. developed a method for the actuation of polydimethylsiloxane (PDMS) artificial cilia by attaching cilia to a lead-zirconate-titanate (PZT) microstage and driving the stage at a given frequency. Artificial cilia were tall rectangular structures, 800 μm long by 10μm wide with a depth of 75 μm, driven from 40−140 Hz and exhibiting resonance at 95 Hz. These artificial cilia were capable of mixing two different fluids an order of magnitude faster than could be accomplished by mixing through diffusion alone (Oh et al., 2009; Oh et al., 2010).

3.1.4 Actuation with magnetics

One of the more popular methods of artificial cilia actuation is the utilization of a magnetic driving force. The use of magnetics requires no internal on-chip power or leads and will not affect any sensitive chemistries within an experiment. Magnetic artificial cilia make up by far the largest class of artificial cilia in the literature. Within this class, there exist

two main methods of fabrication: (i) loading elastic polymers with varying concentrations of magnetic particles (Evans et al., 2007a; Fahrni et al., 2009b), and (ii) chemically or magnetically linking paramagnetic beads (Furst et al., 1998; Singh et al., 2005; Vilfan et al., 2010). Both the ability to vary the magnetic loading within a flexible polymer matrix and the use of linker molecules of varying molecular weight between magnetic beads creates a more flexible artificial cilium. In addition, for linked beads, the length and diameter are easily controlled parameters set by the number and diameter of linked beads, respectively.

The first application of a crosslinked magnetic composite material for the fabrication of artificial cilia was presented in 2007 by Evans et al. (Evans et al., 2007a). Superparamagnetic nanoparticles were dispersed within a hydrophobic polymer matrix (PDMS), and the mixture was templated into 800 nm diameter by 25 μm tall cylindrical pores. As I utilized this fabrication method to obtain results presented in this thesis, further discussion of this method will occur in Chapter 4. Following the 2007 publication, Fahrni et al. used a similar magnetic composite material composed of Fe-C ferromagnetic particles and PDMS to fabricate artificial cilia 300 μm long by 100 μ wide by 15 μm thick. These cilia were actuated with a rotating magnetic field, resulting in a torsional motion that induced vortical movement of fluid around each cilium (Fahrni et al., 2009b).

The other prevalent class of magnetic cilia-like actuators surfaced in 1998 when Furst et al. presented a method for the synthesis of chains of paramagnetic beads. Amine and carboxylic acid surface functionalized polystyrene beads (1 μm in diameter) were deposited into a flow cell of a given height, and a magnetic field was applied perpendicular to the flow cell. Beads aggregated into chains, and with the introduction of glutaraldehyde to

the flow cell, a covalent chemical linkage between neighboring beads was formed. These chains were not anchored to a substrate, and the average length of the chain was not well controlled in this fabrication process, as reported length averages exhibited large error, such as 14 ± 7 μm (Furst et al., 1998).

The fabrication process detailed in Singh et al. in 2005 improved upon Furst et al.'s first design of linked paramagnetic beads by tethering large arrays of linked chains to a glass substrate. This tethering was achieved by patterning the glass substrate with amine groups and utilizing carboxylated polystyrene beads ~790 nm in diameter coated with 25 nm magnetic nanoparticles. The linkage between beads was formed with poly(ethylene glycol) (PEG) diamine and the application of a magnetic field perpendicular to the glass substrate. After the creation of chains $12-75$ μm in length, deflection was obtained by applying a magnetic field to the chain array. In addition to the benefit of being tethered to a substrate, the flexibility of these artificial cilia was easily tunable by modifying the molecular weight of the PEG diamine crosslinking molecule (Singh et al., 2005).

Most recently, Vilfan et al. described the fabrication, actuation, and fluid propulsion abilities of paramagnetic chains 31 μm long and 4.4 μm in diameter secured to a substrate at one end (Vilfan et al., 2010). This report on artificial cilia is the closest in size to biological cilia other than those I will describe in the next chapter which were developed in our research group. In addition, this is also the only report, other than Shields, Fiser, et al., which utilizes a biologically relevant beat shape to drive a net fluid flow. These artificial cilia are driven at 1 Hz by an electromagnet in a tilted conical beat shape similar to the beat shape of vertebrate embryonic nodal cilia. With this actuation, Vilfan et al. obtained

a net flow ten microns above artificial cilia tips. The array size of these artificial cilia is unfortunately only 3x3, nine cilia total, spanning approximately 50 μm, and little mention is made of constructing much larger arrays to study fluid flow. Figure 3.2 shows the 3x3 array of paramagnetic chains and the resulting fluid flow above cilia tips, as tracked by the addition of tracer particles to the fluid (Vilfan et al., 2010).

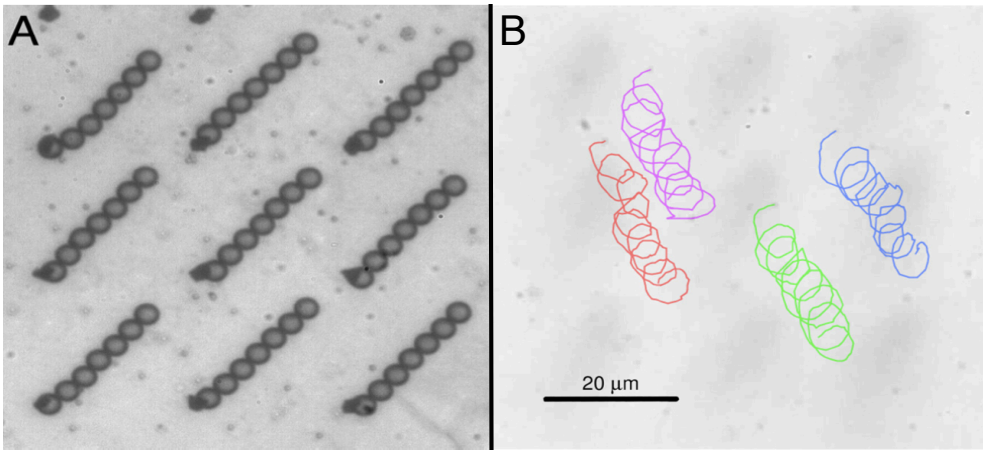

Figure 3.2: Reprinted from Vilfan et al. (2009). (A) Artificial cilia, 31 μm long by 4.4 μm in diameter, are capable of propelling fluid flow at a velocity of 3.3 ± 0.2 μm/s when driven at 1 Hz with a tilted conical beat shape. The tracks shown in (B) are those of tracer particles added to the fluid (Vilfan et al., 2010).

3.2 Cantilevered beams as damped, driven harmonic oscillators

Both biological and biomimetic cilia can be modeled as high aspect ratio rods; thus, it is important to understand the mechanical properties of slender rods, including how the deflection of a rod is determined by its load. A cilium can be represented as a cantilevered beam clamped and immobile at one end and free at the other. For smaller forces, the

beam's response, or curvature, will be fairly linear with the torque applied. Cantilevers are characterized by a curvature κ and a bending moment M. For a purely elastic cantilever, κ and M are analogous to x and F in Hooke's law for a spring. The beam equation for a slender, cantilevered beam experiencing a small force and exhibiting a small deflection is (Howard, 2001)

$$M = EI\kappa. \tag{3.1}$$

Like Hooke's law, which has a constant of proportionality called the spring constant k, the beam equation has a constant of proportionality called the flexural rigidity EI. The flexural rigidity is a quantity which characterizes all beams by taking into account both the Young's modulus E of the beam material and the second moment of inertia I relating to the beam's cross section. If a beam's cross-sectional shape is non-circular, the flexural rigidity may depend on the direction of the bend. For example, a long rectangular beam like a wooden coffee stirrer is easier to bend about one axis than the other. The curvature κ of the beam is the inverse of the radius of curvature R and is effectively a measure of how a line tangent to the beam's curve changes as it is measured at various points on the curve.

Figure 3.3 is the coordinate system used in defining the differential equation for all beams. The beam's deflection is y, and θ is the angle between the x-axis and a tangent line drawn at any point m on the deflected beam. The radius of curvature R is then defined as the change in the angle θ, or $d\theta$, over an arc length ds which is between two points, m_i and m_j, on the deflected beam's curve.

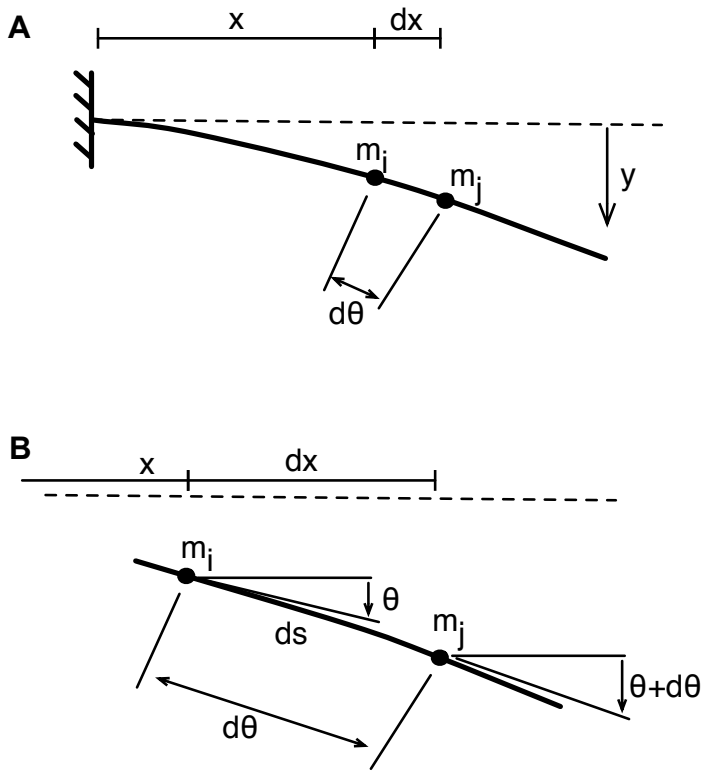

Figure 3.3: (B) Depicts a portion of the cantilever represented in (A). Further details in the text (Gere and Timoshenko, 1990).

Since $\kappa = 1/R$, we can write (Gere and Timoshenko, 1990)

$$\kappa = \frac{1}{R} = \frac{d\theta}{ds}. \tag{3.2}$$

For small angles, I assume $cos\ \theta \approx 1$, and thus the geometrical relationship $ds = dx/cos\ \theta$ seen in Figure 3.3 becomes $ds \approx dx$. Equation 3.2 is then

$$\kappa = \frac{d\theta}{ds} = \frac{d\theta}{dx}. \tag{3.3}$$

In addition, the slope of the deflection curve is its first derivative, and from Figure 3.3, we

see $dy/dx = tan\theta$. This relation combined with the small angle approximation $tan\,\theta \approx \theta$ gives

$$\kappa = \frac{d\theta}{dx} = \frac{d^2y}{dx^2}. \tag{3.4}$$

Equation 3.4 provides us with a relation between the beam's curvature and its deflection and is valid for any beam material. However, it is useful only when θ is small. If we are working with a linearly elastic beam, then Equation 3.4 reduces to Equation 3.1 presented previously. When the deflection of the beam is not small, we cannot assume that $d\theta/ds \approx d\theta/dx$ and must instead use the expression for curvature exactly shown in Figure 3.3. The differential beam equation then becomes (Gere and Timoshenko, 1990)

$$\kappa = \frac{\frac{d^2y}{dx^2}}{\left(1 + \left(\frac{dy}{dx}\right)^2\right)^{3/2}}. \tag{3.5}$$

For simplicity of the model, I will assume a small deflection, thus using Equation 3.4. In addition to the mechanical properties of the rod, I need to consider its hydrodynamic properties. The interaction, such as drag, between a cilium and its surrounding fluid, will affect cilium response. The deflection of a cantilevered beam with both viscous damping and an external excitation force $f(x,t)$ per unit length is given by (Brücker et al., 2007)

$$EI\frac{\partial^4 y(x,t)}{\partial x^4} + m_{acc}\frac{\partial^2 y(x,t)}{\partial t^2} + \frac{4\pi\eta}{ln(L/2D)}\frac{\partial y(x,t)}{\partial t} = f(x,t) \tag{3.6}$$

where m_{acc} is the accelerated mass, η is the fluid viscosity, and L and D are the cantilever length and diameter. Equation 3.6 must be integrated over the entire length L of the can-

tilever to determine deflection curve of the beam and is valid only for low frequencies and small deflection amplitudes. The third term which represents the drag on the cantilever was originally derived by Venier et al. in 1994 for microtubules (Venier et al., 1994).

Following the treatment of Br*ü*cker et al., 2007, note the similarity between this slender beam equation and the one-dimensional harmonic oscillator. The flexural rigidity is analogous to the spring constant k; a mass term is present; the third term represents the drag force; and $f(x,t)$ is the external force acting on the oscillator. Thus, we approximately have the following (Brücker et al., 2007):

$$k^*\tilde{y} + m^*\frac{\partial^2\tilde{y}}{\partial t^2} + c^*\frac{\partial\tilde{y}}{\partial t} = f(t). \tag{3.7}$$

I can treat the coordinate $\tilde{y}$ as the one-dimensional cartesian coordinate y. For completeness, I will briefly discuss the general solution for a damped, driven harmonic oscillator, after which, I will return to Equation 3.6 to explore the relationship between amplitude and frequency for my biomimetic cilia system.

3.2.1 The damped and driven harmonic oscillator

The equation of motion for a damped, driven harmonic oscillator includes a driving force, a damping force, and a restoring force. My experiments utilize a driving force which oscillates in time which I will approximate as sinusoidally varying with some frequency ω. The damping force is applied by the actuator's environment, and for a viscous environment, it is linearly proportional to the fluid's viscosity. (I will use the term 'oscillator' and 'actuator' interchangeably as the actuators I discuss in this thesis are oscillating actuators.)

The restoring force of the oscillator is approximated as the spring force. Assuming the oscillation occurs in y as I previously assumed beam deflection in the y direction,

$$F = -ky - c\dot{y} + F_0 cos(\omega t) \tag{3.8}$$

where the first term is the restoring force with spring constant k, the second term represents the damping force with damping coefficient c, and the third term is the sinusoidal driving force with amplitude F_0 and drive frequency ω. The damping force is a viscous retarding force represented by c, which in turn is proportional to fluid viscosity; the value of this term will depend on the geometry of the oscillator and fluid environment. Dividing by the oscillator's mass m, and letting $F = m\ddot{y}$ gives

$$\ddot{y} = -\frac{k}{m}y - \frac{c}{m}\dot{y} + \frac{F_0}{m}cos(\omega t). \tag{3.9}$$

Let ${\omega_0}^2 = k/m$, $\gamma = c/2m$, and $A = F_0/m$ where ω_0 is the characteristic angular frequency of the oscillator without any damping, and γ is the damping factor. After some rearrangement,

$$\ddot{y} + {\omega_0}^2 y + 2\gamma\dot{y} = Acos(\omega t) \tag{3.10}$$

The solution to Equation 3.10 is a two part solution: a transient part and a steady state part. Transient effects that will die out after some given time; the steady state represents the natural frequency of the oscillator. For a short period of time, the oscillator's frequency is a linear superposition of its natural frequency and the driving frequency. As long as the

time $t >> 1/\gamma$, I can ignore the transient portion of the solution and focus on the steady state solution (which is caused by the driving force) for $y(t)$,

$$y(t) = \frac{A}{\sqrt{(\omega_0{}^2 - \omega^2)^2 + 4\omega^2\gamma^2}} cos(\omega t - \delta) \tag{3.11}$$

where δ is the phase difference between the drive force and resultant motion, evaluated as

$$\delta = arctan\left(\frac{2\omega\gamma}{\omega_0{}^2 - \omega^2}\right). \tag{3.12}$$

Because we are looking at the steady state solution, the oscillator should respond at the drive frequency ω. At low drive frequencies, we expect an oscillator to have the ability to keep up with the drive force and thus the phase difference between the two equals zero. For higher drive frequencies, the acceleration will be large, and the phase difference may be as large as 180° as an oscillator's acceleration is out of phase with its displacement by 180°.

As I mentioned previously, the relationship among the amplitude, the damping factor γ, and the drive frequency ω are important in understanding how well an actuator will perform in a dynamic context with or without a highly viscous environment. Note that this is not a method for determining material parameters which go into fabrication, merely it is a predictor of responsiveness based on drive forces, drive frequencies, and actuator geometry. The amplitude of a damped, driven oscillator is

$$A(\omega) = \frac{F_0/m}{\sqrt{(\omega_0{}^2 - \omega^2)^2 + 4\omega^2\gamma^2}}. \tag{3.13}$$

When the drive frequency is nearly equal to the undamped natural frequency ω_0, a phe-

nomenon called resonance occurs. Resonance results in a maximum amplitude, and we can determine the resonance frequency ω_r by differentiating Equation 3.13 and setting it equal to zero. For a simple harmonic oscillator, the resonance frequency is equal to the natural, undamped frequency, $\omega_0 = \sqrt{k/m}$. For a damped, driven oscillator, the resonance frequency ω_r becomes a combination of the undamped resonance frequency ω_0 and the damping factor γ:

$$\omega_r{}^2 = \omega_0{}^2 - 2\gamma^2. \tag{3.14}$$

If the damping factor is weak or goes to zero, $\omega_r \rightarrow \omega_0$, or if $2\gamma^2 > \omega_0{}^2$, we have the case of strong damping and no resonance in our system. When $\gamma > \omega_0$, a harmonic oscillator is considered overdamped, and the amplitude will decrease as the drive frequency ω increases. This relationship is evident if we consider the limiting case $\gamma^2 = \omega_0{}^2/2$; Equation 3.13 then becomes

$$A(\omega) = \frac{F_0/m}{\sqrt{(\omega_0{}^4 - \omega^4)}} \tag{3.15}$$

where $A(\omega)$ clearly decreases as ω increases.

Recall that Brücker's treatment of the beam equation for a damped, driven cantilever clamped at one end (Equation 3.6) drew several analogues between the deflection of a beam due to an excitation force and the equation of motion for a damped, driven harmonic oscillator (Equation 3.8). Following his treatment and including the mass within the square root, we can write the amplitude and phase for a damped, driven harmonic cantilever as the

following (Brücker et al., 2007):

$$A(\omega) = \frac{F_0}{\sqrt{\left(k^* - m^*\omega^2\right)^2 + c^{*2}\omega^2}}. \tag{3.16}$$

$$\delta = arctan\left(\frac{\omega c^*/m^*}{\left(\frac{k^*}{m^*}\right)^2 - \omega^2}\right). \tag{3.17}$$

where the constants are defined as (Brücker et al., 2007)

$$k^* = \frac{60}{11}\frac{EI}{L^3}, \quad m^* = \frac{13}{33}LA\rho_p, \quad c^* = \frac{52}{33}\frac{\pi\eta L}{ln(L/2D)}. \tag{3.18}$$

For the constants defined above, A is the cantilever's cross-sectional area, ρ_p is the density of the material, η is the fluid viscosity, and L and D are the length and diameter of the cantilever. Equation 3.16 with the constants defined in Equation 3.18 model the dependence of the amplitude of a cantilevered rod on frequency and fluid viscosity. For a rod at low Reynolds number (as discussed in Chapter 6), the mass term in Equation 3.16 can be neglected due to its small size (on the order of 10^{-14}) and the amplitude becomes

$$A(\omega) = \frac{F_0}{\sqrt{k^{*2} + c^{*2}\omega^2}}. \tag{3.19}$$

With the constants included, Equation 3.19 is

$$A(\omega) = F_0\left(\left(\frac{60}{11}\frac{EI}{L^3}\right)^2 + \left(\frac{52}{33}\frac{\pi\eta L}{ln(L/2D)}\right)^2\omega^2\right)^{-1/2}. \tag{3.20}$$

The first term represents the mechanical properties of the actuator and is on the order of $\sim 10^{-10}$ after being squared and considering the contributions from the second mo-

ment of inertia ($\sim 10^{-26}$), the cube of the length scale ($\sim 10^{-15}$), and the elastic modulus, which is approximately 10^6 for a pure PDMS rod. The second term considers the effect of the fluid (hydrodynamic properties) and the drive frequency. For buffer of viscosity $\eta = 1$ cP=10^{-3} Pa·s, the damping coefficient squared is on the order of 10^{-16} due to contributions from the viscosity and rod length ($\sim 10^{-6}$). The drive frequency ranges from 1−32 Hz, making the second term on the order of $\sim 10^{-14}$. It is evident in buffer that the first term ($\sim 10^{-10}$) dominates compared to the second term $\sim 10^{-14}$, and an increase in drive frequency with the frequency range of my experiments will have little effect on the amplitude of the actuator. As viscosity increases and the rod's elastic properties remain constant, an increase in drive frequency does begin to affect rod amplitude. For example, with a viscosity increase of 100 cP (0.1 Pa·s), the second term is then on the order of $\sim 10^{-10}$, and we must consider the effect of viscosity and increasing drive frequency.

In addition, for a cantilevered rod, the natural undamped frequency is $\omega_0 = \sqrt{k/m}$, and for $k \sim 10^{-3}$ and $m \sim 10^{-15}$, $w_0 \sim 10^5$. For an oscillator to be overdamped, $\gamma > \omega_0$. For a buffer of viscosity $\eta = 1$ cP, $\gamma = c/(2m) \sim 10^6$; thus in buffer, which is the lowest viscosity fluid other than air in which biomimetic cilia oscillate, this system is overdamped.

The following figure represents a survey of cantilevered rod amplitudes in various viscosities as a function of frequency. In the experiments detailed in Chapters 6 and 7, I utilized three different biomimetic cilia lengths and diameters: 25 μm by 2 μm, 25 μm by 1 μm, and 10 μm by 0.55 μm. Thus, I model the amplitude dependence for two of these rod geometries, 25 μm by 1 μm and 10 μm by 0.55 μm. The force on the rod is in the form of a torque acting at the rod's tip, generated by a 10 mT applied magnetic field. Ex-

perimentally, I apply an oscillating magnetic field ranging from 10−125 mT. Because the magnetic dipoles within a rod-shaped actuator align head-to-tail along the rod's long axis, when a magnetic field is applied, a torque is generated as the dipoles within the rod seek to minimize the discrepancy between the applied field direction and the rod's long axis. Magnetic torque is discussed in more detail in the next section, as it is a useful parameter for understanding the limits of an actuator's ability for force application on a fluid, regardless of the fluid. In this model, magnetic force is a numerical value dependent on the rod's magnetic moment, the applied field, and the location of subsequent torque application.

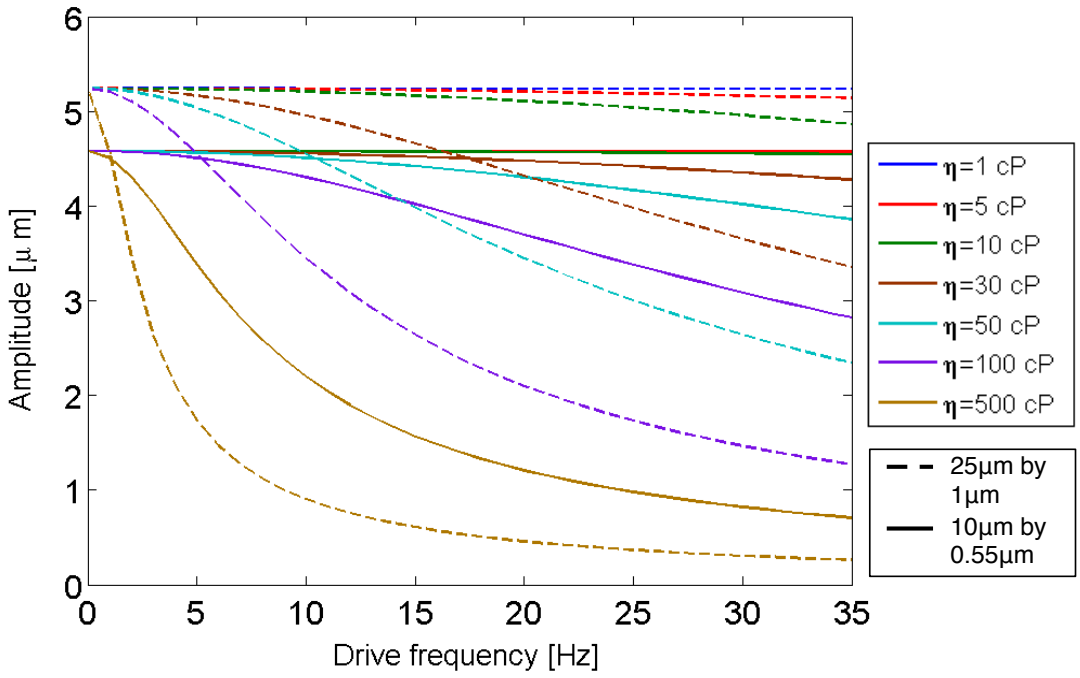

Figure 3.4: Core-shell rod amplitude dependence on frequency for varying fluid viscosities (1 cP, 5 cP, 10 cP, 30 cP, 50 cP, 100 cP, and 500 cP). Notice that the longer rod length may initially have a larger amplitude; however, as viscosity increases, the amplitude is damped out much more quickly than for the shorter, smaller diameter rods. In addition, the model indicates that core-shell oscillators are overdamped for fluids with $\eta \geq 1$ cP.

The beam equation and the solution for the damped, driven harmonic oscillator are both

important tools for understanding amplitude dependence on frequency in order to gauge the dynamic responsiveness of an oscillating actuator. However, these tools do not assist in determining fabrication parameters such as the amount of magnetic material which will optimize the response of an actuator in both its elasticity and magnetic permeability. For these considerations, I turn to an energy minimization model first proposed by Evans et al. in 2007 (Evans et al., 2007a).

3.3 Figure of Merit for Actuators

To be responsive, the flexibility and magnetic permeability of an actuator must be balanced. Achieving this balance, especially in at small scales can be difficult. For many microactuators, increasing the amount of magnetic material (or magnetic loading) increases the amount of force one can apply, but also leads to a decrease in the flexibility of the actuating structure. Therefore, it is important to design an actuator such that the highest response possible is obtained. Current designs for actuating structures include chemically or magnetically linked paramagnetic beads (Furst et al., 1998; Singh et al., 2005; Vilfan et al., 2010), thin magnetic films deposited onto flexible substrates (Judy et al., 1995; Liu, 1998; Khoo and Liu, 2001; Kudo et al., 2006), elastic polymers loaded with varying concentrations of magnetic particles (Evans et al., 2007a; Pirmoradi et al., 2010; Fahrni et al., 2009b; Fuhrer et al., 2009; Olsson et al., 2010; Evans et al., 2012), and polymer core-metal shell structures with varying metal shell lengths (Fiser et al., 2012).

In this section, I will explore a figure of merit derived from an energy minimization model developed by Ben Evans et al. to evaluate the responsiveness of both homogeneous

and core-shell rod-shaped actuators. The maximum bend angle, or static response, of a rod-shaped actuator is predicted based on the actuator's magnetic loading, saturation magnetization, and elastic modulus (Evans et al., 2007a; Evans, 2008; Evans and Superfine, 2011).

3.3.1 Energy minimization model

Ben Evans' energy minimization model was originally designed for a homogeneous material, an example of which is the composite ferrofluid-PDMS (FFPDMS) I will describe in Section 4.2. This FFPDMS material is a suspension of magnetic nanoparticles within a flexible polymer matrix. With a few small substitutions, I am able to apply this model to a core-shell structure.

In this energy model, the first of its kind to include the effect of the magnetic field gradient, the total energy of the rod system is defined as the sum of the elastic energy U_E of the bent rod and the magnetic energy U_B of the rod in the applied magnetic field. The magnetic energy U_B is a combination of the energy due to the applied field $U_A(\vec{B}_A)$, the energy due to the rod's internal magnetic field $U_I(\vec{B}_I)$, and the energy due to the field felt from neighboring rods $U_N(\vec{B}_N)$ where B represents the magnetic field for each energy. The rod itself is modeled as a rod with constant curvature to determine the elastic energy and a straight rod with diameter d and length L, as shown in Figure 3.5, to determine the magnetic energies.

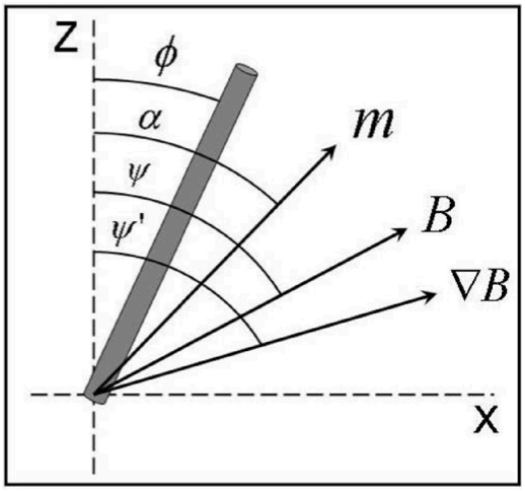

Figure 3.5: Reprinted from Ben Evans et al., 2007. Physical parameters in the energy minimization model. The vector $\vec{m}$ is the rod's magnetic moment, $\vec{B}$ is the applied magnetic field, and $\nabla\vec{B}$ is the magnetic field gradient. All angles shown are with respect to the vertical axis. The angle ϕ is the bend angle of the rod, α is the angle of the rod's moment m, ψ is angle of the applied field, and ψ' is the angle of the magnetic field gradient (Evans et al., 2007a).

The elastic energy for a uniform rod of circular cross section is defined as (Evans et al., 2007a)

$$U_E = \frac{\pi}{2}\frac{Er^4}{L}\phi^2 \tag{3.21}$$

where E is the elastic modulus, r is the radius of the rod, and ϕ is the rod's bend angle as indicated in Figure 3.5. The magnetic energy of the rod is defined as the sum of the energies due to the applied field, the rod's internal magnetic field, and the field felt from neighboring rods. For rod arrays such as mine with a rod spacing on the order of 10 μm, the field from the rod's nearest neighbor is at least two orders of magnitude less than the applied magnetic field and will be ignored. (For a detailed calculation of this, see Evans 2008.) The remaining two energies are termed the 'gradient energy' and the 'field energy',

and are given as (Evans, 2008)

$$U_B = -\frac{1}{2} m \nabla B L cos\left(\psi' - \phi\right) - \frac{\mu_0 m^2}{4V} cos^2\left(\psi - \phi\right) \tag{3.22}$$

where μ_0 is the permeability of free space, V is the volume of the rod, and ∇B is the magnetic field gradient. All angles are defined in Figure 3.5. An applied magnetic field can act on magnetic rods in two ways – by inducing a torque or by applying a force. A torque is induced if there is misalignment between the rod's long axis and the direction of the applied magnetic field. This internal energy is designated the 'field energy' and is the second term in Equation 3.22. The first term is called the 'gradient energy' and is due to the pull of the magnetic field on the rod to areas of higher magnetic field.

The total energy of the rod, combining elastic and magnetic energies, is (Evans, 2008)

$$U_T = \frac{\pi}{2} \frac{E r^4}{L} \phi^2 - \frac{\mu_0 m^2}{4V} cos^2\left(\psi - \phi\right) - \frac{1}{2} m \nabla B L cos\left(\psi' - \phi\right). \tag{3.23}$$

The magnetic moment m is defined as $m = MVf$ where f is the magnetic loading, or volume fraction of magnetic material, and M is the magnetization per unit volume of the material in response to an applied field. The value for M is taken from SQUID magnetometry measurements of the pure magnetic material such as those discussed in Section 4.2 for maghemite and magnetite and Section 4.3.3 for nickel.

Evans showed in his thesis that the rod's moment aligns with the applied magnetic field under the condition $4B/[\mu_0 M(B) f] >> 1$. This condition does not depend on the actuator's geometry, but only the magnetic material. From magnetometry measurements of the ap-

plied magnetic field and resulting saturation magnetizations, for maghemite, $4B/[\mu_0 M(B)f] \sim 4.5\times10^6$, for magnetite $4B/[\mu_0 M(B)f] \sim 1.3\times10^6$ and for nickel $4B/[\mu_0 M(B)f] \sim 1.6\times10^6$. Thus, I can neglect the term in Equation 3.23 which represents the effect of the magnetic gradient on the actuator, and the equation for the total energy of a rod in an applied magnetic field becomes

$$U_T = \frac{\pi}{2}\frac{Er^4}{L}\phi^2 - \frac{\mu_0 M^2 f^2}{4} cos^2(\psi - \phi). \tag{3.24}$$

We can determine the torque on the rod and thus the rod's maximum bend angle ϕ by minimizing the rod's total energy with respect to the angle ϕ. This derivative gives the torque as

$$\frac{\partial U_T}{\partial \phi} = \frac{\pi E r^4}{L}\phi - \frac{\mu_0 M^2 f^2}{2} cos(\psi - \phi) sin(\psi - \phi), \tag{3.25}$$

If an optimal alignment of angles ϕ and ψ (the angular positions of the rod and applied field, respectively) is assumed such that the rod's axis is aligned with the field direction and $cos(\psi - \phi)sin(\psi - \phi) \rightarrow 1/2$, and if we solve for ϕ, the maximum bend angle of a rod-shaped actuator in response to an applied magnetic field is the following:

$$\phi = \frac{\mu_0 M^2 f^2}{E}\left(\frac{L}{d}\right)^2. \tag{3.26}$$

The first factor in Equation 3.26 represents only the material properties of the actuator, and the second factor considers the geometry of the rod-shaped actuator. For a more complete comparison among materials, the saturation magnetization M_{sat} is substituted for

M to consider an actuator's maximum actuation for a given material. If the magnetization, elastic modulus, and loading for a given rod geometry is known, the responsiveness of the actuator can be predicted, allowing for the design of new materials which will maximize ϕ. I would like to note before discussing the application of this equation to core-shell actuators that it appears the best way to increase actuator responsiveness for a given magnetic material is by increasing magnetic loading f. However, for many homogeneous composite materials, E increases when f increases. Several models have been established to explain the elastic modulus of a composite material as a function of f (Ahmed and Jones, 1990), and many of them demonstrate E's parabolic dependence on f. This dependence may signify that a small increase in f will result in an astronomical increase in E and a material which may no longer be workable.

Equation 3.26 was designed to facilitate comparisons of the responsiveness of homogeneous actuators. With some modification, it can be applied to core-shell rod structures to quantify differences among materials using the maximum bend angle, which I will do in Section 5.1. The most significant modification to Equation 3.26 will involve the volume fraction. For homogeneous materials, the first factor in Equation 3.26 considers only material properties; however, with the core-shell structure, I no longer have a single bulk composite material. The final actuator is a combination of two materials specifically deposited into a rod-shaped pore. Figure 3.6 is a diagram of a core-shell structure.

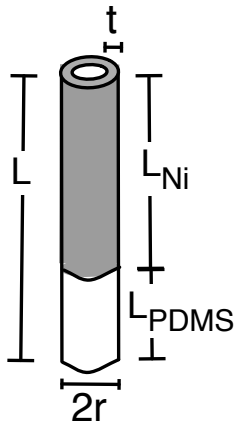

Figure 3.6: Core-shell rods of length L consist of a polymer core which spans the length of the entire rod and a nickel shell of length L_{Ni} and thickness t. The length of the pure PDMS portion is denoted L_{PDMS}.

The volume fraction of Ni is given by

$$f_{CS} = \frac{L_{Ni}}{L}\left(\frac{2t}{r} - \frac{t^2}{r^2}\right) \tag{3.27}$$

where r is the radius of the rod, L_{Ni} is the Ni tube length, t is the Ni tube thickness, and the CS subscript indicates f is for core-shell cilia. I take L in Equation 3.26 to equal the length of the PDMS portion, $L_{PDMS} = L - L_{Ni}$, as the portion of the rod surrounded by the Ni tube acts as a stiff projection from the rod's soft PDMS base. Substituting this and f_{CS} into Equation 3.26 gives

$$\phi_{CS} = \frac{\mu_0 M^2}{E}\left(\frac{t}{r^2} - \frac{t^2}{2r^3}\right)^2\left(L_{Ni} - \frac{L_{Ni}^2}{L}\right)^2. \tag{3.28}$$

From this result, it is clear there is some Ni tube length which optimizes the actuator's responsiveness. The elastic modulus E is also now uncoupled from f, changing only with

choice of polymer core, since solely the length of the PDMS portion changes as the L_{Ni} changes. The maximum of ϕ_{CS} with respect to L_{Ni} occurs at $L_{Ni} = 0.5L$. To achieve a maximum static bend angle, new core-shell actuators should include a nickel portion one-half the rod's entire length.

To determine both ideal and experimentally achievable bend angles for homogeneous and core-shell rod arrays with Equations 3.26 and 3.28, we first need to understand the relationship between E_{FFPDMS} and f. For lower volume fractions such as $f < 0.4$, the elastic modulus of homogeneous composite materials such as FFPDMS is thought to change very little (Guild and Young, 1989; Ahmed and Jones, 1990); however, many experimental composite elastomers have magnetic loadings less than 20% as $f > 0.2$ is difficult to achieve experimentally (Evans et al., 2012; Evans et al., 2007a; Fahrni et al., 2009a). In order to predict the elastic modulus at higher volume fractions, I utilize the Mooney equation, developed by M. Mooney in 1950 to describe rigid inclusions in a non-rigid matrix. For FFPDMS, the elastic modulus of maghemite nanoparticles is 10^5 times greater than the PDMS matrix in which they are entrapped. The Mooney equation is given by (Mooney, 1951)

$$G_c = G_m exp\left(\frac{2.5f}{1 - Sf}\right) \tag{3.29}$$

where $G_c = G_{FFPDMS}$ is the shear modulus of the composite material, $G_m = G_{PDMS}$ is the shear modulus of the matrix material, and S is the self-crowding factor. The self-crowding factor is a measure of the packing of the spherical particles (maghemite in FFPDMS) within the matrix material; it is the volume that the particles occupy/the actual physical volume of

the particles. For a loosely packed composite material, $S = 1.0$, and for a tightly packed material $S = 1.35$ (Mooney, 1951). For volume fractions from 0−0.7, Figure 3.7 illustrates the upper and lower bounds, provided by S, for the shear modulus of the FFPDMS composite material. The matrix modulus was taken as $G_{PDMS} = 0.83$ MPa ($E_{PDMS} = 2.5$ MPa).

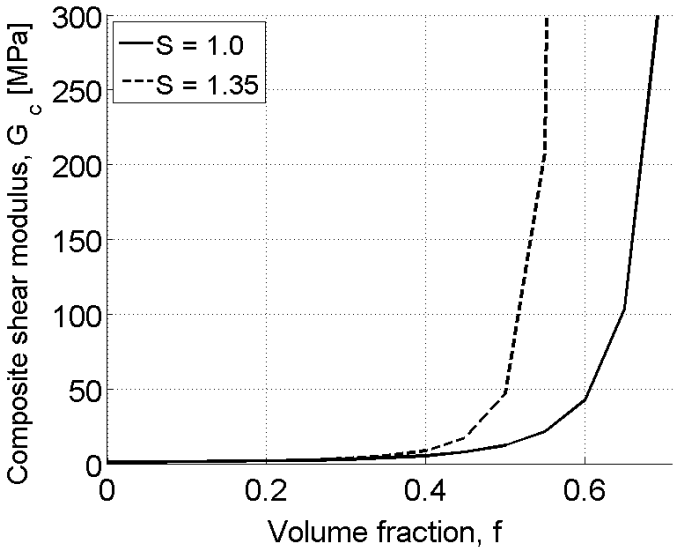

Figure 3.7: The Mooney equation (Equation 3.29), which represents the shear modulus of FFPDMS as a function of volume fraction, has been plotted for loosely packed spherical inclusions ($S = 1.0$,−) and tightly packed spherical inclusions ($S = 1.35$,−−) (Mooney, 1951).

Before substituting this relation for G_{FFPDMS} into Equation 3.26, the shear modulus must be converted to the elastic modulus by

$$E_{FFPDMS} = 2G_{FFPDMS}(1 + \nu) \tag{3.30}$$

assuming a Poisson ratio $\nu = 0.5$ for PDMS (Roca-Cusachs et al., 2005). Using this conversion, Equation 3.26 becomes

$$\phi = \frac{\mu_0 M^2 f^2}{2G_{FFPDMS}(1+\nu)}\left(\frac{L}{d}\right)^2. \tag{3.31}$$

The same can be done for core-shell cilia with Equation 3.28.

Figure 3.8 illustrates how homogeneous materials such as FFPDMS and FFPDMS-NH_2 in rod-shaped actuator form compare to core-shell actuators. Because my experiments utilize rods which are 10 μm and 25 μm in length by 0.55 μm$-$1.0 μm in diameter, Figure 3.8 plots the theoretical maximum bend angle for rod lengths 10 μm and 25 μm, a rod diameter ranging from 0.5-1.0 μm. As this energy minimization model gives no upper bounds for the bend angle, non-physical bend angles are not represented in the figures. For the smaller rod length of 10 μm, core-shell rods far surpass composite rods, with a maximum bend angle of 80° for a 500 nm rod. FFPDMS rods barely achieve a 45° bend angle; FFPDMS-NH_2 rods are capable of bending 65°. Note that the maximum bend angles are not necessarily achievable volume fractions for FFPDMS and FFPDMS-NH_2 cilia. The highest volume fractions achieved thus far are indicated on the figure as dashed vertical lines. For FFPDMS and FFPDMS-NH_2, they are $f = 0.04$ and $f = 0.17$; at these volume fractions, composite material bend angles are closer to 5° and 35°, respectively. Thus, the core-shell material has a wider advantage over the homogeneous composite material, as larger volume fractions and thus larger bend angles are experimentally achievable.

Considering the 25 μm length and excluding nonphysical bend angles (not shown), FFPDMS cilia achieve larger amplitudes than core-shell cilia for a given diameter. However, for FFPDMS, the volume fractions are as yet unachievable to produce these larger bend angles. Only when larger volume fractions become experimentally achievable will

the composite material prove advantageous in use with higher aspect ratio actuators.

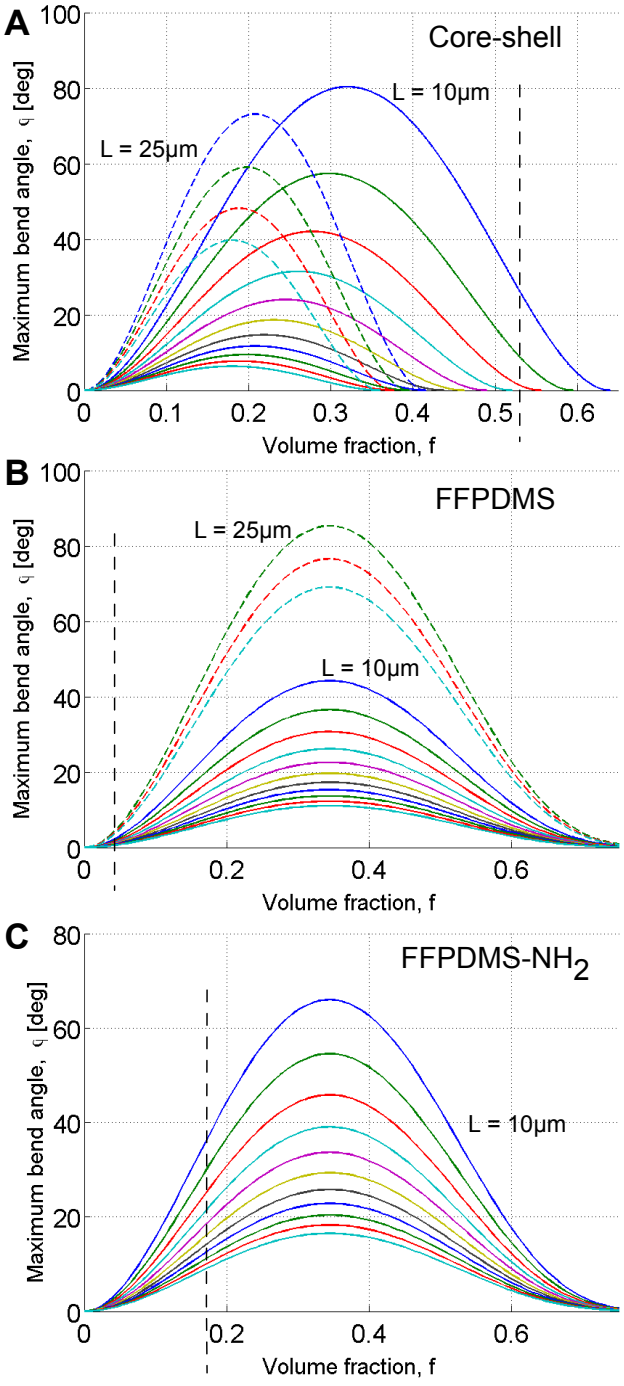

Figure 3.8: Bend angles for (A) core-shell, (B) FFPDMS, (C) FFPDMS-NH_2 rods with lengths 10 (–) and 25 (- -) μm and diameters 0.5-1.0 μm in 50 nm increments. The largest bend angle for $L = 10$ μm corresponds to $d = 0.5$ μm. For 25 μm, ϕ is largest when $d = 0.85$ μm in (A), 0.9 μm in (B), and in (C), FFPDMS-NH_2 rods have only non-physical bend angles and are not shown. For FFPDMS and FFPDMS-NH_2, bend angles are plotted with $S = 1.0$. Vertical lines in each plot indicate experimentally achieved volume fractions.

3.4 Torque on a Rod

Predicting the maximum bend angle with Evans' energy minimization model is an approach to quantify an actuator's static responsiveness. However, because an increasing drive frequency and strong environmental damping will cause a decrease in an overdamped oscillator's amplitude, it is additionally integral to compare actuators of different materials utilizing the magnetic torque which can be achieved. The magnetic torque quantifies an actuator's ability to apply forces to the fluid regardless of actuator load or drive frequency. Torque is dependent only on the magnetic material (and thus moment) of an actuator and the direction of the applied magnetic field. I examine the magnetic torque on a rod-shaped actuator by assuming a stationary, upright rod where the magnetic moment is optimally aligned with the applied field. Magnetic torque N on a dipole is written as (Jackson, 1998)

$$\vec{N} = \vec{m} \times \vec{B} = mBsin\left(\theta_{mB}\right)\hat{n} \tag{3.32}$$

where B is the applied field and $m = MVf$ is the magnetic dipole moment (as described in Section 3.3.1). M is the magnetization per unit volume (determined by SQUID magnetometry measurements), V is the rod volume, and f is the volume fraction of magnetic material. Torque is minimized when the rod aligns itself with the applied magnetic field, as the cross product is equal to zero when the the angle between the dipole moment and applied field is zero.

Torque depends on the particular magnetic material utilized in an actuator and the volume fraction of material, but does not depend on an actuator's geometry. A larger volume

fraction does supply a higher torque; however, a larger volume fraction also leads to a higher modulus and stiffer actuator. Utilizing the combination of bend angle and torque is best to optimize an actuator's magnetic loading.

Experimentally, the magnetic field B is typically on the order of 10 mT, though it may range from 1 mT−300 mT. Thus, in the calculation for torque, I let B=10 mT, and $M = M_{sat}$. To compare torque for composite materials and core-shell materials with volume fractions 0−1, the rod geometry will be identical to the geometry used for bend angle comparisons, 10 μm or 25 μm lengths and 0.5 μm diameter. The maghemite saturation magnetization is $M_{sat,Mh} = 3.8 \times 10^5$ A/m (used in FFPDMS), and for magnetite $M_{sat,Mn} = 4.6 \times 10^5$ A/m (used in FFPDMS-NH_2). Core-shell biomimetic cilia actuators are fabricated with nickel, $M_{sat,Ni} = 5.2 \times 10^5$ A/m. Additionally for the core-shell material, I assume the optimal nickel tube length $L_{Ni} = 0.5L$ (determined in Section 3.3.1).

Figure 3.9 displays the torque for all three materials: maghemite composite (red lines), magnetite composite (blue lines), and nickel core-shell (black lines). The two lengths 10 μm and 25 μm are represented by solid and dashed lines, respectively. In Figure 3.9, volume fractions from 0−1 are shown, but the highest volume fraction we have achieved thus far for FFPDMS is 0.04 and for FFPDMS-NH_2 is 0.20, severely limiting the torque on composite rods and potentially the actuation achievable in a more viscous environment. The highest volume fraction repeatably achieved for core-shell actuators thus far is ~0.6.

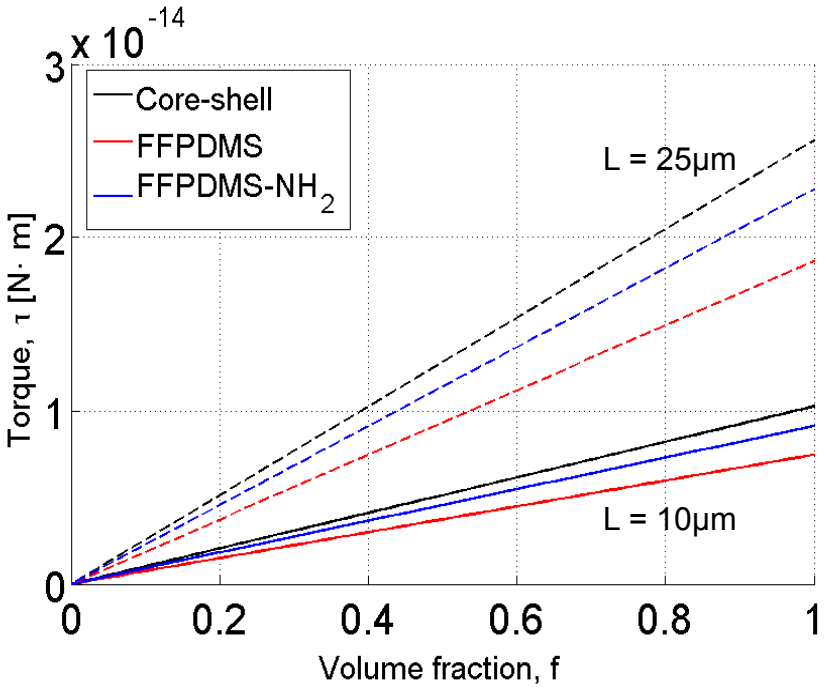

Figure 3.9: The torque of a rod-shaped actuator with diameter 0.5 μm as calculated by Equation 3.32. Solid lines are 10 μm long rods; dotted lines represent 25 μm rods. Across all volume fractions, the nickel core-shell actuator (black lines) outperforms both the maghemite composite (red lines) and magnetite composite (blue lines) actuators. Experimentally achieved volume fractions for maghemite, magnetite, and core-shell are 0.04, 0.20, and 0.60, respectively.

As the plot indicates, increasing f for FFPDMS, FFPDMS-NH_2, and core-shell cilia will continue to increase the torque on the cilium. However, a higher torque and therefore higher volume fraction does not guarantee larger deflection. We may look specifically at core-shell cilia to see this. Figure 3.10 plots both the bend angle curve and the relation for torque as functions of volume fraction. As we surpass 30% magnetic material by volume, the torque nearly doubles, but rod bend angle begins to decrease.

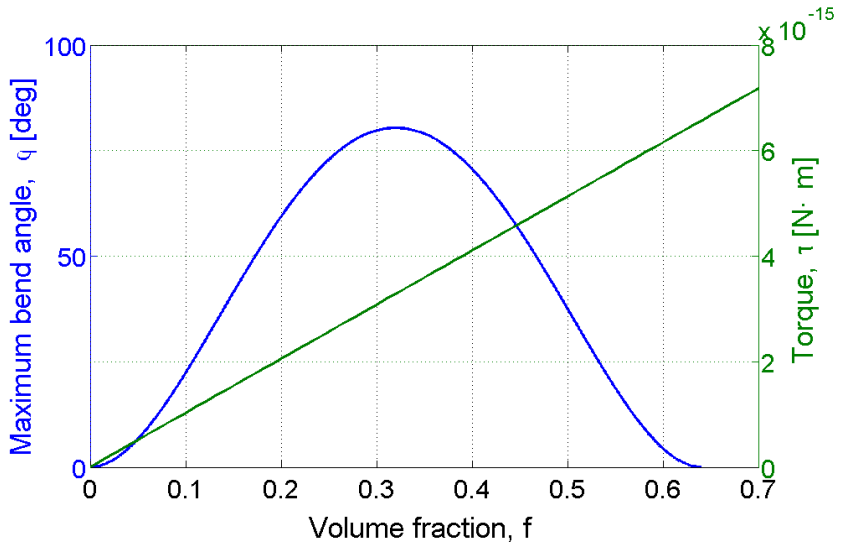

Figure 3.10: The torque and maximum bend angle as a function of volume fraction for core-shell cilia with a length of 10 μm and diameter of 500 nm. As torque on the rod increases, bend angle increases until $\sim f = 0.30$, when the bend angle begins to decrease. At this point, torque continues to increase, though the rod has become less responsive.

The design of various (FFPDMS, FFPDMS-NH_2, and core-shell) actuators is strongly dependent on the application for which they will be utilized; the sacrifice some amount of deflection to move in a higher viscosity fluid may or may not be a goal. Regardless, utilizing both the theoretical bend angle and torque to optimize magnetic loading is beneficial in designing a rod with maximal static responsiveness under potentially large loads. In conjunction with designing the actuator such that it has a high response, the actuator should be modeled using the driven, damped harmonic oscillator equations in the first sections of this chapter to determine whether or not the high static responsiveness will also translate into a large dynamic responsiveness in both aqueous and high viscosity environments.

3.5 Ground and Lateral Collapse

In addition to determining material contributions to the design of a more responsive actuator, it is important to understand the effect of forces at the micron scale on high aspect ratio fabricated structures. Rods with high aspect ratios are subject to adhesive forces which act to pull them either to the ground, known as ground collapse, or against their nearest neighbors, known as lateral collapse. The success of these adhesive forces tends to be proportional to a rod's aspect ratio; higher aspect ratios imply a higher likelihood of collapse. Collapse occurs because the elastic forces which work to keep a rod upright are weaker than the adhesive forces which work to keep a rod in contact with either the ground or another rod. This is particularly a problem with PDMS, the polymer utilized for both composite and core-shell biomimetic cilia, because of its hydrophobic nature and lower affinity for a liquid environment than for itself. PDMS's surface energy is therefore lower when it is in contact with itself (Roca-Cusachs et al., 2005; Zhang et al., 2006).

Ground collapse is defined literally as the collapse of rods to the ground and subsequent adherence due to adhesion forces such as van der Waals forces. Rods are considered collapsed if they do not return to their original upright positions. Roca-Cusachs et al. developed a quantitative model in 2005 to predict the critical aspect ratio above which ground collapse occurs due to these adhesive forces. This critical aspect ratio is(Roca-Cusachs et al., 2005)

$$\left(\frac{L}{d}\right)_g = \frac{\pi^{5/3}}{2^{11/3}3^{1/2}}\left(1-\nu^2\right)^{-1/6}\left(\frac{Ed}{W}\right)^{2/3} \tag{3.33}$$

where ν is Poisson's ratio, E is the elastic modulus (E_{PDMS} = 2.5 MPa), and W is the work of adhesion of the material to itself (Roca-Cusachs et al., 2005). Poisson's ratio for a material is defined as the negative of the lateral strain over the axial strain, or the decrease in width divided by the increase in length. For PDMS, ν = 0.5. In addition to ground collapse, there is also lateral collapse, which is the adhesion of one rod to another due to their proximity. The critical aspect ratio for lateral collapse is defined as (Roca-Cusachs et al., 2005)

$$\left(\frac{L}{d}\right)_L = \left(\frac{3^3\pi^4}{2^{11}(1-\nu^2)}\right)^{1/12}\left(\frac{s}{d}\right)^{1/2}\left(\frac{Ed}{W}\right)^{1/3} \tag{3.34}$$

where s is the spacing between rods, which for our templates is on the order of 7 μm. To calculate the conditions for ground and lateral collapse for biomimetic cilia, approximate values for the work of adhesion of PDMS in air, water, and ethanol were taken from Roca-Cusachs et al.: W_A = 44 mN/m, W_W = 86 mN/m, and W_E = 11 mN/m (Roca-Cusachs et al., 2005). For rods with a diameter of 0.55 μm, the critical aspect ratios for ground and lateral collapse are presented in Table 3.1 for air, water, and ethanol.

Table 3.1: Critical rod aspect ratios for ground and lateral collapse

	$(L/d)_g$	$(L/d)_L$
Air	3.19	11.8
Water	2.04	9.40
Ethanol	8.03	18.7

The values in Table 3.1 indicate that aspect ratios on the order of 10 or larger are unlikely to survive ground or lateral collapse. To have an array of rods which truly mimic biological cilia, I typically fabricate rods which are 10 μm and 0.55 μm in diameter, an

aspect ratio of 18. Thus, it is particularly important to develop materials and a fabrication process which are more robust as rods with this aspect ratio are not considered stable by these models for ground and lateral collapse. Figure 3.11 shows several different examples of collapsed rods with aspect ratios ranging from 18 to 31.

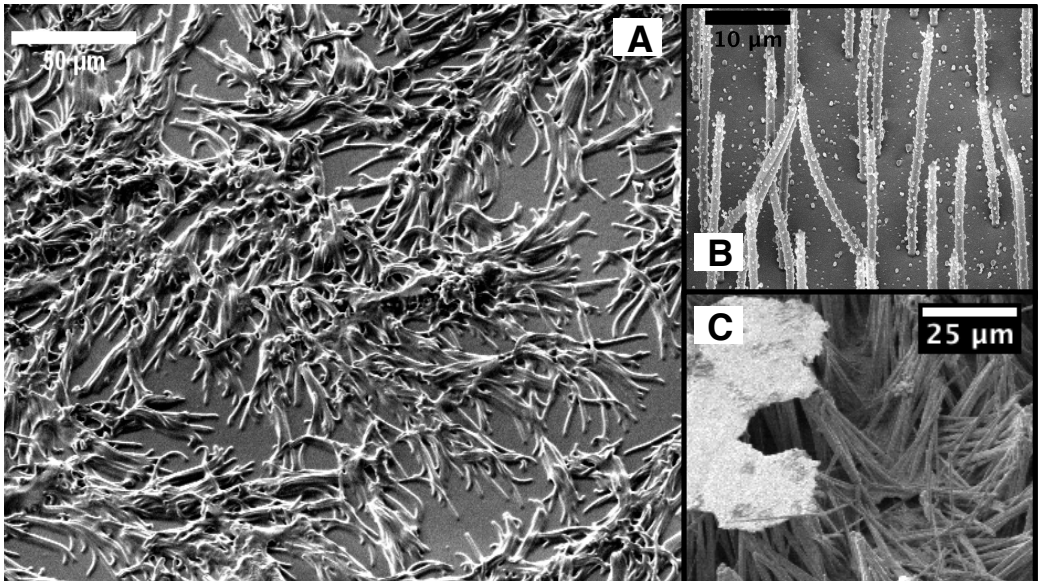

Figure 3.11: SEM images of rods with aspect ratios ranging from 18-31 exhibiting both ground and lateral collapse. (A) FFPDMS-NH_2. (B) FFPDMS. (C) core-shell rods.

Chapter 4

Materials and Fabrication

Designing an actuator by maximizing its bend angle and torque through consideration of flexibility and magnetic permeability is valuable for determining the materials and length scales used in the fabrication process. Different materials may require fabrication at varying length scales due to differences in responsiveness. Higher elastic moduli may result in a more rigid actuator at lower aspect ratios; thus, fabrication at higher aspect ratios may be required for a particular application. For flexibility in the fabrication process, we use polycarbonate track-etched filter membranes as a template for our biomimetic cilia. With these filter membranes, we can easily alter the pore diameter to adjust the aspect ratio, creating more or less rigid biomimetic cilia for a given material.

In the first section of this chapter, I discuss the template fabrication process including how pore diameter is altered. This template method is utilized in the remaining sections where I discuss two types of materials from which we fabricate biomimetic cilia: magnetic nanoparticle composite materials and core-shell materials. The magnetic composite materials utilize either maghemite or magnetite nanoparticles, both of which are superparamagnetic. The core-shell materials are fabricated with a nickel shell and are ferromagnetic in nature. The synthesis of these materials and the fabrication of biomimetic cilia using

these materials are described in detail throughout this chapter.

4.1 Template Fabrication

Polycarbonate track-etched (PCTE) filter membranes are a smart choice for use as a template due to their commercial availability and the variety of sizes in which they can be manufactured (Figure 4.1). The physical characteristics of the template – thickness, pore diameter, and pore density – translate into the biomimetic cilium's height, cilium diameter, and cilia spacing, respectively. These membranes can be purchased with standard thicknesses ranging from 10 μm to 100 μm. (Other thicknesses are available on special request.)

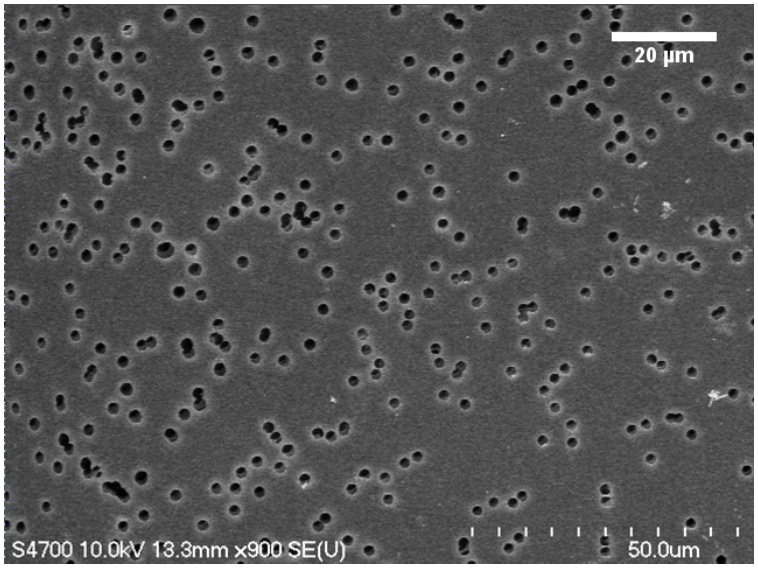

Figure 4.1: SEM image of PCTE membrane 25 μm thick with an average pore diameter of 1.9 μm.

PCTE membranes are fabricated by bombarding polycarbonate sheets with an ion beam. Ions pass through the polycarbonate, leaving damage tracks in the ions' wakes. The beam

which irradiates the polycarbonate is a directional beam such that each damage track is perpendicular to the plane of the polycarbonate. Depending on the manufacturer, the irradiation source may or may not be directional; thus, some damage tracks may have a diagonal orientation or pass through one another. These damage tracks may be widened into cylindrical pores by incubating the PCTE membranes in a 4M sodium hydroxide (NaOH) solution. Longer incubation times at higher temperatures produce larger pore diameters. Figure 4.2 depicts the relationship between a 10 μm thick membrane's pore diameter and the incubation time in 4M NaOH at 80°C. After incubation in NaOH, PCTE membranes are copiously rinsed in deionized water and dried with a stream of nitrogen.

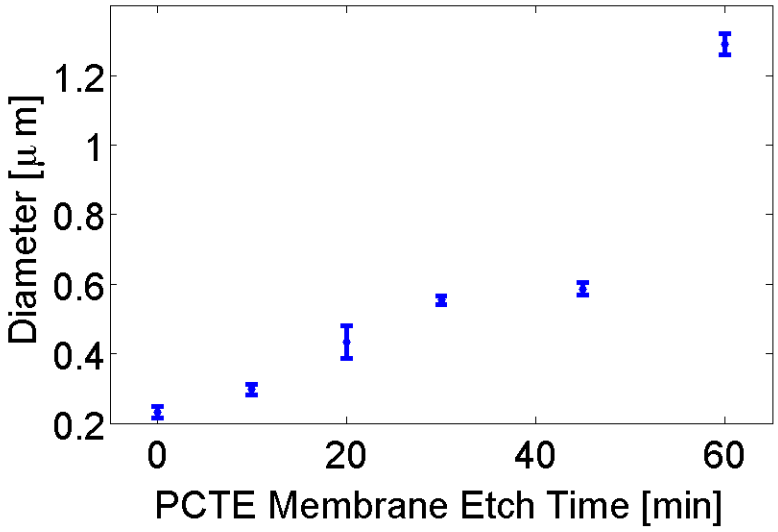

Figure 4.2: PCTE membrane (10 μm thick) pore diameter as a function of incubation time in 4M NaOH. Incubation was performed at 80°C.

Additionally, PCTE membranes are a smart choice for template fabrication as the density of pores and polymer coating can be specified for a variety of applications. Available pore densities range from $1x10^5$ pores/cm^2 to $6x10^8$ pores/cm^2. This large range in pore

density is especially useful in fabricating structures with large aspect ratios, as higher densities can lead to lateral collapse for high aspect ratio structures (Section 3.5). Polymer coatings may also be useful depending on the membrane's application. Poly(vinylpyrrolidone) (PVP) is a coating applied to PCTE membranes to increase hydrophilicity, thereby increasing the membrane's ability to wet and its effectiveness as a filter or fillable template.

For the fabrication of biomimetic cilia, we purchased PCTE membranes (www.it4ip.be) with thicknesses of 25 μm and 10 μm, a pore diameter of 200 nm, and a density of 2×10^6 pores/cm^2. With this pore density, the typical spacing between adjacent cilia is on the order of 10 μm. I utilized 25 μm membranes to fabricate biomimetic cilia with a ferrofluid-polymer composite material (as described in Section 4.2), and 10 μm membranes to fabricate biomimetic cilia with a core-shell structure (as described in Section 4.3).

4.2 Magnetic Composite Materials

Inherent in the fabrication of biomimetic cilia are both the need for a driving mechanism which propels the cilium in a given direction at a specified beat frequency and the ability of the cilium to respond to this driving mechanism. Magnetics offers a promising solution to driving arrays of biomimetic cilia and microactuators in general. No wires or internal, on-chip power sources are required, and magnetic fields are unlikely to affect any chemical reactions occurring in a system. Additionally, large actuator displacements may be achieved and a complex actuator response may be easily orchestrated by manipulating magnet geometries or placement. Magnetic material, however, is intrinsically stiff, typically with an elastic modulus in the GPa range. For microactuators such as biomimetic

cilia to be both magnetic and flexible, we must employ a soft polymer as a matrix for the magnetic material. This type of material is referred to as a magnetic-polymer composite.

Magnetic-polymer composite materials are often used to fabricate highly responsive actuators with flexibility and large magnetic permeabilities; the responsiveness of a structure is the competition between these two properties. After the first synthesis of magnetic nanoparticles in 1852 by Lefort (Lefort, 1852), researchers have been incorporating nanoparticles into polymer matrices to explore their properties. Soft hydrogels such as polyacrylamide (Caykara et al., 2009; Galicia et al., 2003; Mayer et al., 2000) and polyvinyl alcohol (Barsi et al., 1996; Collin et al., 2003; Lin et al., 2003; Mitsumata et al., 1999; Resendiz-Hernandez et al., 2008) are often used, as are hydrophobic silicone polymers (Evans et al., 2007a; Fahrni et al., 2009b; Pirmoradi et al., 2010). In 2007, Ben Evans et al. developed a novel composite material with iron oxide nanoparticles entrapped in the polymer poly(dimethylsiloxane) (PDMS). PDMS is a smart polymer choice because its low elastic modulus ($E \approx 2.5$ MPa) lends it a flexibility that is useful for actuator applications. This composite material is essentially a mixture of maghemite ferrofluid and PDMS, called FFPDMS (Evans et al., 2007a) and is described in Section 4.2.1. In 2008, we designed a new composite material utilizing magnetite nanoparticles chemically complexed to a silicone polymer, as described in Evans, Fiser, et al. (2012) (Evans et al., 2012). This physical attachment of polymer to nanoparticle rather than an entrapment of the nanoparticle within the matrix, allows for a higher loading of magnetic nanoparticles within the final material as there is less potential for aggregates to form or particles to leach. Loading an actuator with a higher amount of magnetic material increases actuator response as long as there is

not also a significant increase in elastic modulus due to the added nanoparticles. I describe this complexed material in Section 4.2.2.

Both maghemite and magnetite have been utilized previously in polymer complexes (Vadala et al., 2004; Francois et al., 2007; Kryszewski and Jeszka, 1998; Wilson et al., 2002), though magnetite more so. Because maghemite and magnetite have high saturation magnetizations, a low sensitivity to oxidation, and the ability to be easily fabricated in-house, they are excellent nanoparticle choices for our composite materials. Figure 4.3 displays the magnetizations of both maghemite and magnetite, measurements taken on a Superconducting Quantum Interference Device (SQUID) magnetometer (Quantum Design Magnetic Property Measurement System) and performed over the range $\pm 5 \text{x} 10^5$ G at a temperature of 300°K. SQUID magnetometers are highly sensitive instruments used to measure a material's response to an applied magnetic field. They are cooled by liquid helium and have detection limits as low as $2 \text{x} 10^{-8}$ emu, or $2 \text{x} 10^{-11}$ Am^2.

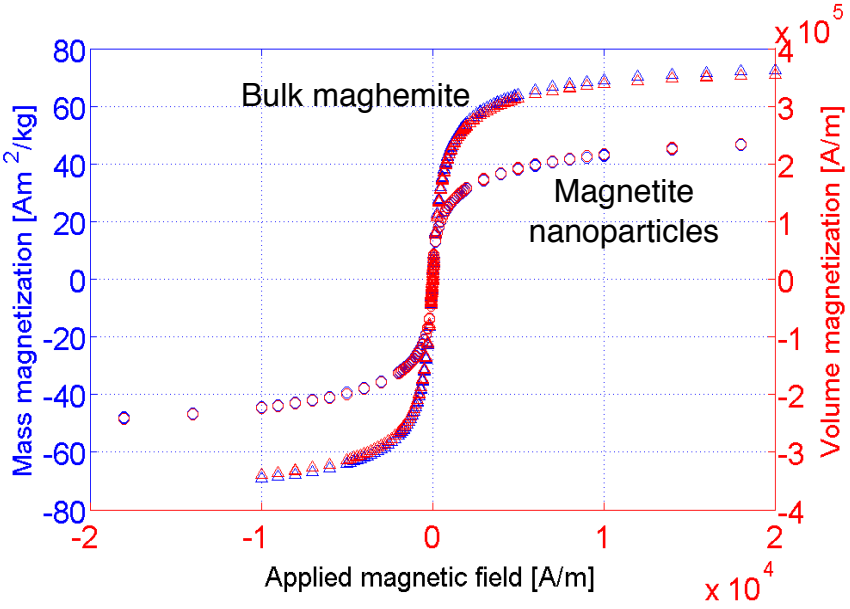

Figure 4.3: Magnetization curves for bulk maghemite and magnetite nanoparticles. The left axis and blue color is mass magnetization, and the right axis and red color is volume magnetization. The saturation magnetization for bulk maghemite is higher than for magnetite nanoparticles, though bulk magnetite has a saturation magnetization of 92-100 Am^2/kg (Cornell and Schwertmann, 2003). The maghemite curve was adapted from Ben Evans' thesis (Evans, 2008).

Nanoparticles less than 10 nm in diameter are considered superparamagnetic, and thus we see no evidence of remanence in the magnetization curves in Figure 4.3. Previously reported saturation magnetization values for bulk maghemite range from 60-80 Am^2/kg. For bulk magnetite, the saturation magnetization ranges from 92-100 Am^2/kg (Cornell and Schwertmann, 2003). However, for magnetite nanoparticles, values are typically 30-50 Am^2/kg (Vadala et al., 2004; Francois et al., 2007; Kryszewski and Jeszka, 1998; Wilson et al., 2002). The saturation magnetizations in Figure 4.3 do fall within this range.

4.2.1 Maghemite-polymer composite material

For the fabrication of our maghemite ferrofluid-polymer composite, or FFPDMS, a ferrofluid of magnetite nanoparticles must first be synthesized according to Massart's (Massart, 1981; Massart et al., 1995) and van Ewijk's (van Ewijk et al., 1999) work, which requires their precipitation from ferric chloride ($FeCl_3$) and ferrous chloride ($FeCl_2$) salts in a 2:1 molar concentration. We dissolve 1.2 g ferric chloride and 0.74 g ferrous chloride tetrahydrate separately in 20 mL of deionized water, and the two components are then mixed in a beaker using a stir bar. Concentrated ammonium hydroxide (20 mL, 29% wt. in water) is added, and the nanoparticles precipitate immediately from solution.

This magnetite ferrofluid is suspended in water and boiled with iron nitrate for oxidation purposes and conversion to maghemite nanoparticles. These solutions contain up to 5% maghemite by weight, but before being incorporated into the organic polymer PDMS, the maghemite nanoparticles must be moved from an aqueous solution to an organic solution. To accomplish this, oleic acid is added to the aqueous solution, and the nanoparticles migrate to the organic oleic acid phase. This organic suspension of maghemite nanoparticles can then be easily combined with PDMS pre-polymer (no crosslinking agent) to form a ferrofluid-PDMS (FFPDMS) composite material. FFPDMS is stable at room temperature for months; it will remain a fluid until PDMS crosslinking agent is added. More details on the fabrication of this material can be found in Benjamin Evans' thesis (Evans, 2008).

When fabricating biomimetic cilia with FFPDMS, we follow the method described by Evans et al. (2007). A PCTE membrane with thickness 25 μm, diameter 800 nm, and pore density 2×10^6 pores/cm^2 is filled with liquid FFPMDS such that the pores are fully occu-

pied by the material (Figure 4.4A). We then immerse this now filled template in uncured PDMS which has been mixed with a crosslinking agent at a ratio of 10 parts pre-polymer to 1 part curing agent (Figure 4.4B). The curing agent will leach into the FFPDMS inside the pores to crosslink that material as well (Evans et al., 2007a).

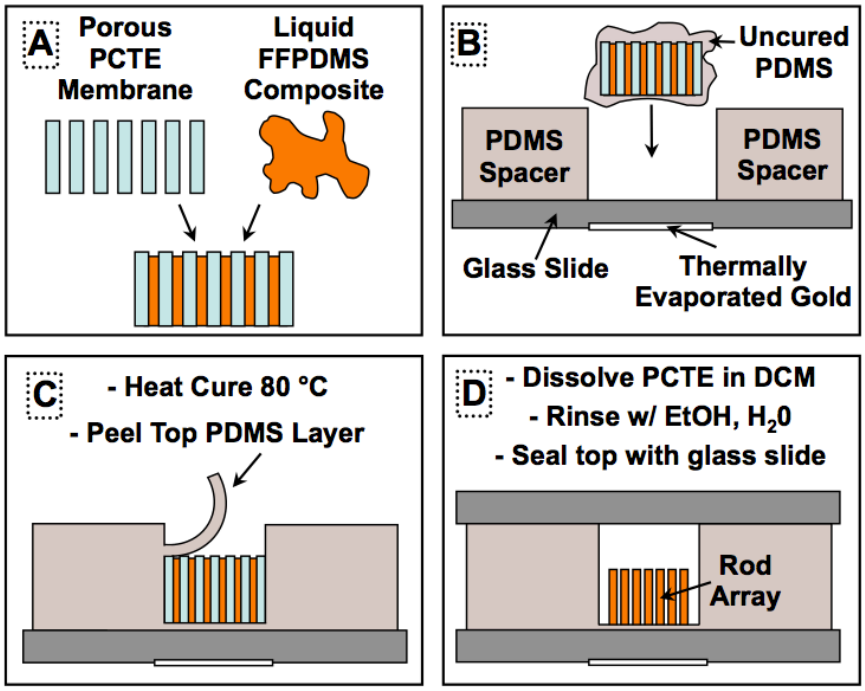

Figure 4.4: Reprinted with permission from Evans et al. (2007). Copyright 2007 American Chemical Society. Cross-sectional view of FFPDMS fabrication procedure. (A) FFPDMS is templated into the porous PCTE membrane. (B) The now filled PCTE membrane is immersed in PDMS mixed 10:1 w/w polymer:crosslinking agent and set into a previously fabricated well structure which will later be used as a fluid reservoir. (C) FFPDMS and PDMS are crosslinked at 80°C for at least one hour. After curing, the top layer of PDMS is removed to expose the PCTE membrane. (D) The membrane is dissolved in dichloromethane at 65°C for two minutes and rinsed in ethanol. The appropriate fluid may be added and the well structure is sealed with a top glass coverslip (Evans et al., 2007a).

The entire sample is placed on a No. 1.5 glass coverslip in the center of a permanent 200-300 μm tall PDMS well structure. The well structure acts as a fluid reservoir and are fabricated in advance by securing crosslinked PDMS doughnut-shaped structures to cov-

erslips through plasma bonding. The FFPDMS-filled template inside the PDMS well is put into a vacuum desiccator to evacuate any air bubbles and then into an 80°C oven for at least one hour to crosslink the PDMS and FFPDMS (Figure 4.4C). After curing, the upper PDMS layer must be removed to expose the PCTE template and array of FFPDMS rods. To free the rods from the PCTE template, we immerse the entire sample in a bath of dichloromethane (DCM) at 60°C. This organic solvent dissolves the PCTE membrane (Figure 4.4D), and we then rinse with ethanol to remove the DCM. The ethanol contains 0.1% Triton-X, which acts as a surfactant to reduce the surface tension of the ethanol and to reduce the interfacial tension between FFPDMS rods and the fluid around them. The ethanol can be exchanged for any fluid and the top of the well can be sealed with a glass coverslip and Norland optical adhesive (Fisher) to eliminate evaporation (Evans et al., 2007a).

Figure 4.5 contains SEM images of FFPDMS cilia where rod arrays have been critical point dried (CPD'd), a process which instantaneously converts liquid carbon dioxide to carbon dioxide gas. A rod sample which has been CPD'd will never feel the effects of a meniscus from evaporating or drying fluid and thus will remain standing upright in air.

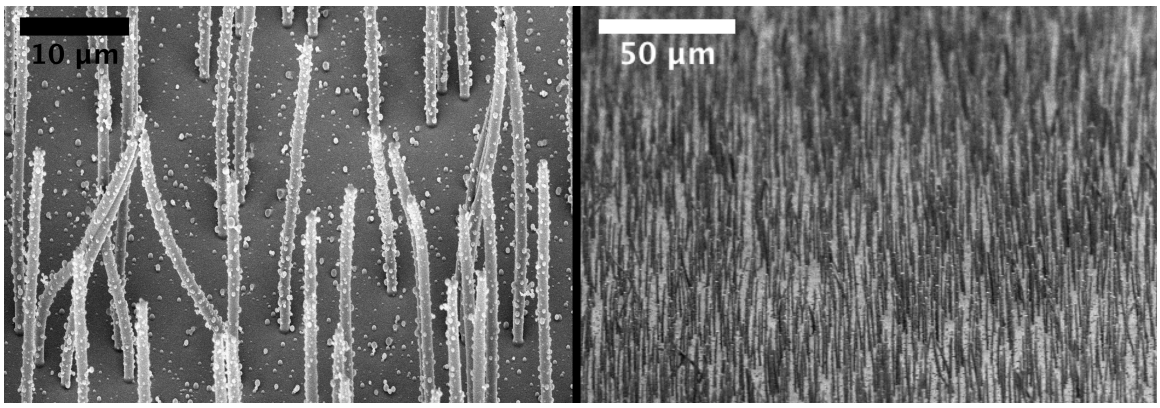

Figure 4.5: SEM images of FFPDMS biomimetic cilia taken by Adam Shields on a 45° tilted sample stage. These arrays have been critically point dried to prevent collapse.

4.2.2 Magnetite-polymer complexed material

The magnetite nanoparticles used to produce the magnetite-polymer complexed material are synthesized following the same initial steps used to synthesize the maghemite nanoparticles in Section 4.2.1. After the precipitation of the magnetite nanoparticles, the polymer to which the magnetite will complex is immediately added. We chose the copolymer aminopropylmethylsiloxane (APMS) with dimethylsiloxane (DMS), with 6-7% APMS mole percent (Gelest, Inc.), as the APMS segment contains amine groups which may be adsorbed onto the magnetite nanoparticle surface. We refer to this copolymer as PDMS-NH_2.

After synthesis the magnetite nanoparticles are suspended in an aqueous solution with a pH~10. We add 2 mL PDMS-NH_2 and stir the mixture for 24 hours, after which it will have separated into a light clear aqueous phase and a dark organic phase. During the 24 hours of stirring, the magnetite nanoparticles are transferred from the aqueous phase to the organic phase by binding to the PDMS-NH_2. Because the pH is greater than the isoelectric point of magnetite, which is pH~6.8 (Tewari and McLean, 1972), but less than the pKa of the amines on the PDMS-NH_2, the positively charged magnetite particles will bind to the negatively charged amine groups. The final product is a complex of a magnetite nanoparticle surrounded by a siloxane copolymer, or FFPDMS-NH_2 (Evans et al., 2012). A diagram depicting the synthesis process is shown in Figure 4.6.

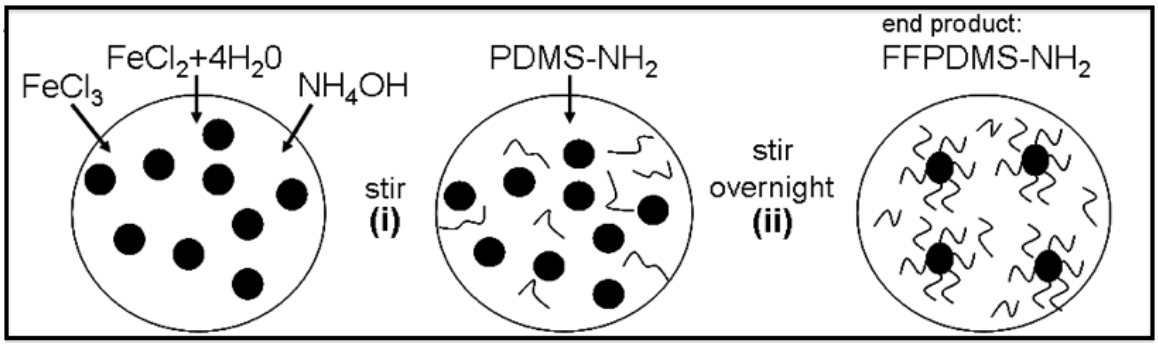

Figure 4.6: Synthesis of FFPDMS-NH_2 complexed material. Details in the text.

After the magnetite nanoparticles have complexed with the PDMS-NH_2, any free magnetite or PDMS-NH_2 is removed by decanting the aqueous phase and rinsing with methanol. The complexed material is then sedimented with a permanent magnet and rinsed five times in methanol, five times in water, and five more times in methanol, sedimenting and decanting after each rinse. We add 15 mL of chloroform and ultrasonicate the solution with a sonic dismembrator (Fisher Scientific Sonic Dismembrater 550) for at least 20 minutes at 30% power with 0.1s on/0.1s off pulses. This sonication step is necessary for the FFPDMS-NH_2 to fully suspend in the chloroform. We sediment the solution overnight and decant one final time to remove any unbound material. In order to also remove the majority of the chloroform, we use a rotovapor until less than 1 mL remains.

To crosslink this material into a magnetic elastomer, we employ a free radical curing process with 10% wt. dicumyl peroxide. This material, now with the crosslinking agent, is placed in a 180°C oven for at least two hours. An initial heating step for two hours at 80°C will prevent the formation of bubbles during crosslinking. When we crosslink FFPDMS-NH_2 alone, it is extremely brittle and unsuitable for use as an actuator. To yield a more flexible elastomer, we dilute the FFPDMS-NH_2 before crosslinking by adding varying

amounts of PDMS-NH_2. The FFPDMS-NH_2 must first be diluted in chloroform, and the PDMS-NH_2 is then added by wt. %. The entire mixture is ultrasonicated, and the added chloroform is then removed by rotovapor. We can fabricate elastomers with up to 17% magnetite by volume; at this concentration of magnetite, the modulus of the elastomer is still less than 3 MPa. (The elastic modulus of pure, crosslinked PDMS is 2.5 MPa.) Table 4.1 shows the physical properties of various dilutions of FFPDMS-NH_2. Saturation magnetization values were taken at an applied field of 50,000 G.

Table 4.1: Properties of various dilutions of FFPDMS-NH_2 in PDMS-NH_2

FFPDMS-NH_2 (%wt. nom.)	%wt. magnetite	%vol. magnetite	Density (kg/m^3)	Saturation Magnetization (kA/m)	Zero-field Elastic Modulus (MPa)
20%	8.7	1.9	1031	4.84	0.54±0.03
30%	13.7	3.2	1156	8.48	0.92±0.06
40%	22.9	5.7	1190	14.14	1.16±0.10
50%	29.9	8.1	1318	20.45	1.52±0.05
60%	36.5	10.5	1501	28.25	1.9±0.3
70%	39	11.6	1545	30.17	2.05±0.14
80%	44.5	14.2	1712	36.79	2.7±0.3
90%	49.6	16.8	1760	45.06	2.9±0.4

FFPDMS-NH_2 is an ideal material for nano- and microscale actuators due to its homogeneity at the nanoscale and lack of nanoparticle aggregation. Figure 4.7 is a transmission electron micrograph showing 70% crosslinked FFPDMS-NH_2.

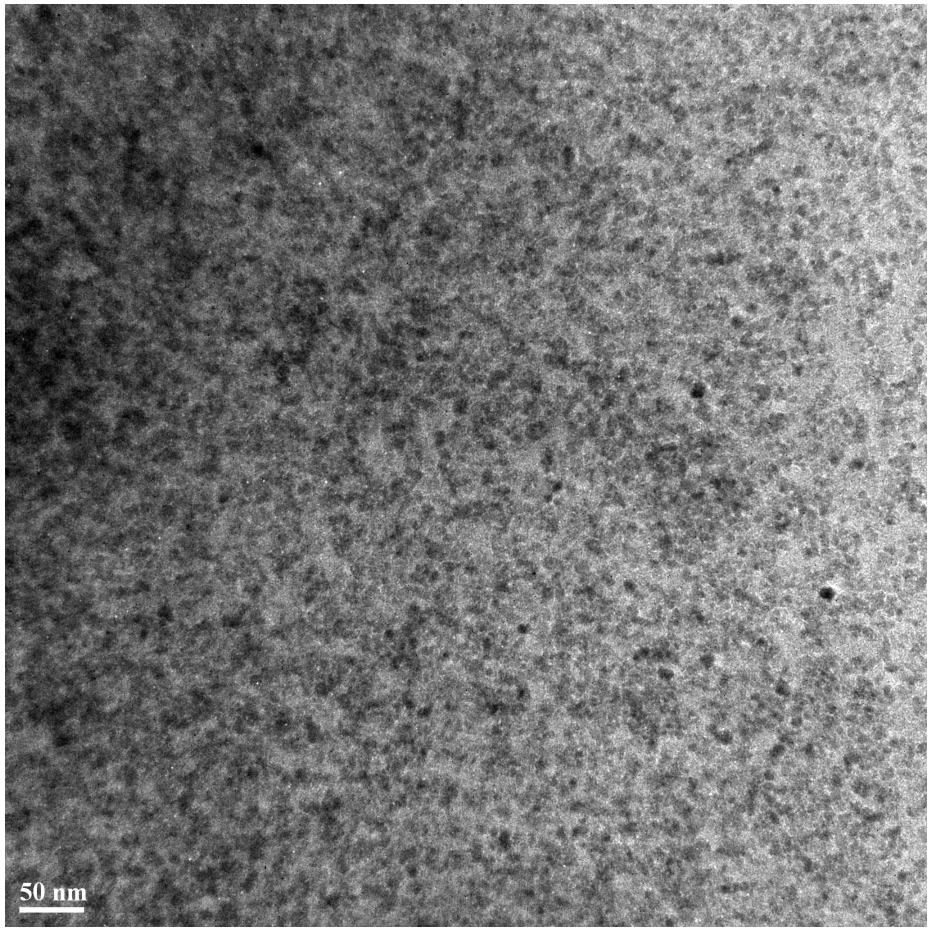

Figure 4.7: TEM image detailing the small scale homogeneity of crosslinked 70% FFPDMS-NH_2.

The fabrication of biomimetic cilia arrays utilizing this FFPDMS-NH_2 material is nearly identical to the procedure for FFPDMS biomimetic cilia (Figure 4.4). We fill the PCTE membrane pores with FFPDMS-NH_2 (which has been previously diluted into PDMS-NH_2 by the desired amount). This FFPDMS-NH_2-filled template is then immersed in PDMS-NH_2, which serves to attach the template to a glass coverslip inside a previously affixed PDMS well structure. Prior to submerging the template in PDMS-NH_2, the crosslinking agent dicumyl peroxide (10% by wt.) is added to PDMS-NH_2. Here again, the curing agent will leach into the FFPDMS-NH_2 within the template, crosslinking that material as

well. The entire sample is put into a 80°C oven for two hours, followed by a 180°C oven for two more hours. To remove the template after crosslinking has occurred, we submerge the sample in a 60°C bath of DCM for two minutes and rinse with ethanol. Figure 4.8 is an SEM image of an array of FFPDMS-NH_2 biomimetic cilia that has been critical point dried.

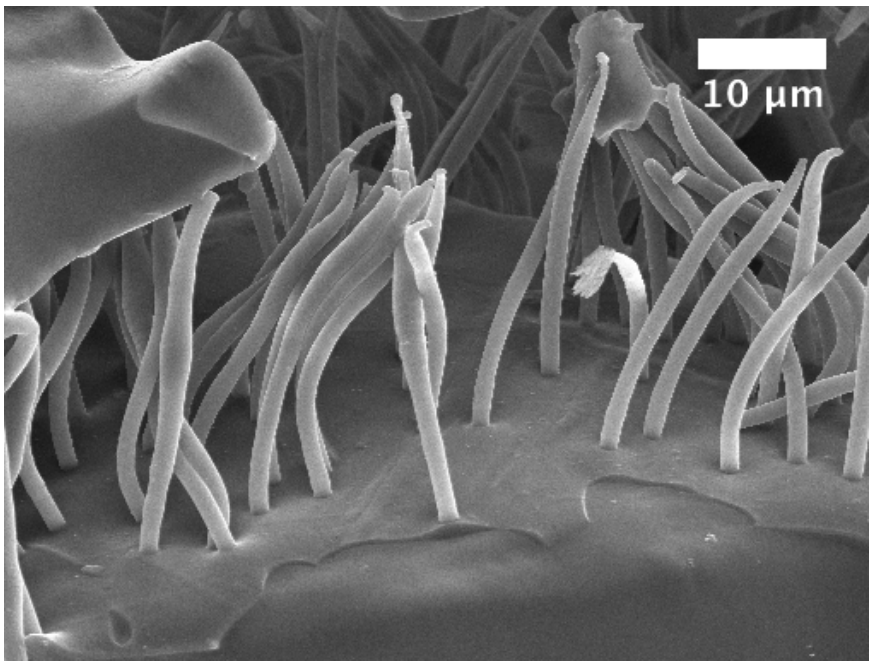

Figure 4.8: SEM image of a critically point dried FFPDMS-NH_2 cilia array taken on a 45° tilted sample stage. The entire upper layer of PDMS-NH_2 was not fully removed from the sample before PCTE membrane dissolution.

4.3 Core-shell Materials

Magnetic composites and complexes are extremely useful materials for fabricating magnetically actuated microstructures capable of moderate responsiveness. However, for many of these materials, to increase actuator response to an applied magnetic field, one must increase the amount of magnetic material, or magnetic loading. Unfortunately, this in-

crease creates a stiffer material and the elastic modulus decreases, leading to a less responsive actuator, limiting the actuator's applications. Many microactuators are overdamped, and thus when driven above some threshold frequency, they suffer from a limited deflection which the application of a larger magnetic field cannot overcome, as the limited magnetic loading leads to a limited application of torque. Additionally, when increasing magnetic loading, magnetic composites are sensitive to issues of magnetic particle aggregation. Aggregation can cause material inhomogeneities, limit the maximum magnetic force that may be applied, and restrict the actuator size.

With a core-shell structure, we can largely uncouple the actuator's elastic and magnetic components to circumvent these issues with loading and flexibility, thereby creating a structure with the ability to achieve large bend angles and maintain sufficient amplitude at higher driving frequencies and in the presence of strong damping. As the length of the shell in a core-shell structure may or may not span the length of the core, the core must be a flexible material to create a highly responsive actuator. I utilize PDMS for the core material, and the shell is electrodeposited nickel (Ni), the length and thickness of which may be controlled by the electrodeposition process. With this structure, magnetic permeability is dependent on the size of the Ni shell, and flexibility hinges on the polymer chosen to be the core (Fiser et al., 2012).

There has been much work with core-shell structures, though nothing has been done to utilize them as magnetically responsive microactuators. The majority of the work has focused on nanorods with metal cores surrounded by either metal or metal-oxide shells, such as SnSe−C, Bi−Bi_2O_3, Ni−Cu, Au−Ni (Pol et al., 2008; Li et al., 2006; Liu et al.,

2008; Kim et al., 2008; Evans et al., 2007b). When polymers are incorporated as the core or shell, they are typically rigid or semi-rigid conducting polymers such as polyaniline (Cao et al., 2001; Lahav et al., 2006) and polypyrrole (Peng et al., 2007; Liu et al., 2010). Applications for these various core-shell actuators include magnetic antennae (Cao et al., 2001), as sensors in electronic devices (Li et al., 2006), and in solar cells (Lahav et al., 2006; Pol et al., 2008). In addition, though they are not core-shell structures, polypyrrole-metal nanotubes have been fabricated for use as an electromagnetic actuator which simulates hand-arm movements (Liu et al., 2010).

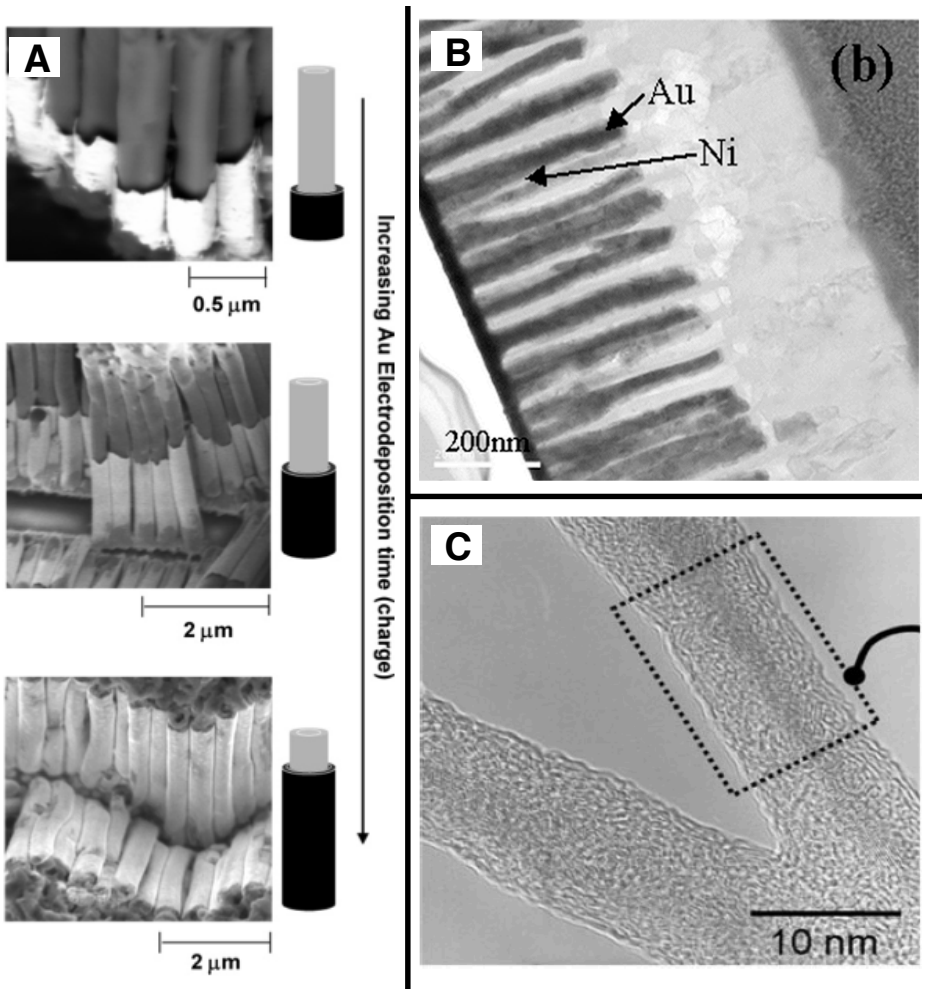

Figure 4.9: Core-shell actuators currently in use. (A) Reprinted from Lahav et al. (2006). Formation of polyaniline-Au core-shell structures as a function of Au deposition time (Lahav et al., 2006). (B) Reprinted from Evans et al. (2007)b. TEM image of Au-Ni core-shell rods embedded in an AAO template (Evans et al., 2007b). (C) Reprinted from Peng et al. (2007). TEM images of copper hydroxide-polypyrrole core-shell structures (Peng et al., 2007).

Within the field of core-shell structures, I have replaced semi-rigid polymers such as polyaniline or polystyrene with silicone and utilized a ferromagnetic metal, thereby developing a process for an entirely new, highly responsive actuator capable of being fabricated and actuated at the micron scale (Fiser et al., 2012). For the fabrication of these new actuators, I utilize PCTE templates 10 μm thick with 550 nm pore diameters. This pore size is

achieved after 30 minutes of incubation in 4M NaOH at 80°C.

4.3.1 Fabrication of core-shell structures

The fabrication of the core-shell structure first requires the creation of the tubular Ni shell within the pores of the PCTE template, followed by a filling step where the shell is filled with polymer. The tubular shell structure is created through the process of electrodeposition, which consists of reducing a solution of positively charged metal ions onto a negatively charged electrode surface. For Ni,

$$Ni^{+2} + 2e^{-} \rightleftharpoons Ni. \tag{4.1}$$

The electrodeposition system consists of three electrodes: a Cu working electrode, a Ag/AgCl reference electrode, and a Pt auxiliary electrode. The PCTE template is placed against the Cu working electrode, and this electrode acts as a negatively charged anode. The Ag/AgCl reference electrode is free floating in the solution of Ni ions and responsible for feedback between the computer and the electrodeposition system. The auxiliary electrode serves as the positively charged cathode in the system. This electrode is typically Pt, but may be replaced by another metal depending on the ions deposited. Figure 4.10 is a schematic illustrating the electrodeposition set-up and the role of each electrode.

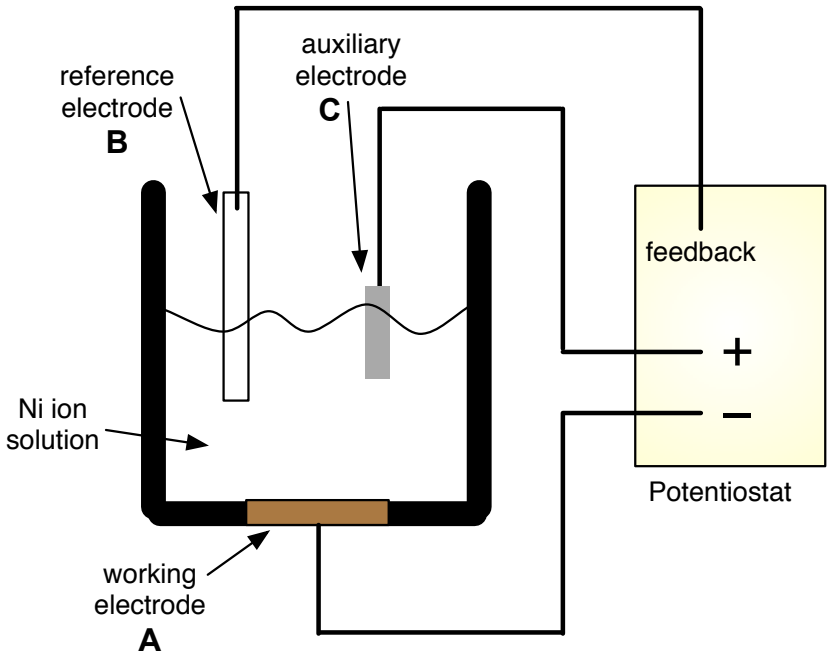

Figure 4.10: The electrodeposition system with its three electrodes. The working electrode (labeled as *A*) acts as the negatively charged anode. Ni ions reduce onto the working electrode. The reference electrode (labeled as *B*) provides feedback to the controlling computer and monitors the deposition. The auxiliary electrode (labeled as *C*) acts as a positively charged cathode.

As the Ni ions reduce onto the working electrode, they are reducing into the PCTE template, as the template is placed against the working electrode. However, good electrical contact must be made between the two, and merely pressing the PCTE template against the working electrode does not achieve this contact. Instead, we deposit a 200 nm layer of metal onto one side of the PCTE template. The thickness of 200 nm has been optimally chosen such that the layer does not significantly occlude the pores, as shown in Figure 4.11. This lack of occlusion is central to the creation of tubes rather than rods.

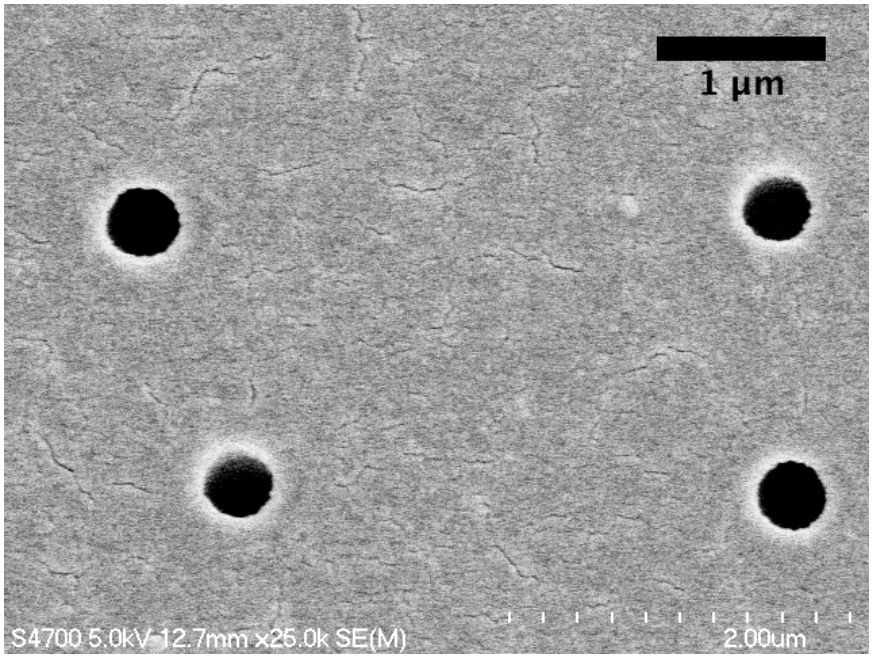

Figure 4.11: SEM image of 200 nm Cu layer sputtered onto one side of the PCTE membrane. Originally, the pore diameter was 550 nm; with the Cu layer, the pore diameter is approximately 400 nm.

This layer of metal is deposited by conventional physical vapor deposition sputtering techniques either in a desktop sputter coater (Ted Pella Cressington 108) or in a cleanroom sputtering system (Kurt Lesker PVD 75); the technique used depends on the desired metal. I have explored many different metals for use as a working electrode contact: Al, Au, Au/Pd, Cu, Ti. Each of these has a different conductivity and different method for removal after the electrodeposition process is complete and biomimetic cilia samples have been made. For a description of each metal's characteristics, see Table 4.2.

Table 4.2: Characteristics of sputtered metals

Metal	Conductivity ($\times 10^5$)	Etchant	Etch Time
Al	3.77/Ωcm	1M NaOH	30 sec
Au	4.52/Ωcm	$KI{\cdot}I_2-$phosphate complex	45 sec - 4 min
Pd	0.950/Ωcm	N_2HSO_4	1 min
Cu	5.96/Ωcm	KOH	> 1 hr
Ti	0.234/Ωcm	Deep reactive ion etcher	30-45 min

Figure 4.13 describes the core-shell cilia fabrication process step by step. The initial sputtering step is illustrated in Figure 4.13A. After being sputtered, I place the metal-sputtered side against the Cu working electrode and electrodeposit Ni from a Ni solution consisting of 60 g/L $NiSO_4{\cdot}6\,H_2O$, 30 g/L H_3BO_3, and adjusted to pH 2.9 using H_2SO_4 (Kumar and Chakarvarti, 2004). The deposition occurs at a controlled voltage of -1 V. If a voltage less than 1 V is utilized, the deposited metal may not be fully Ni, but instead a combination of Ni and NiO_2.

I typically deposit 30-50 mC of charge into a 5 mm circular area of PCTE membrane (Figure 4.13B); this is approximately 2.04 mC/mm^2 and produces Ni tubes 3-7μm in length and 100 nm in thickness. After Ni tube deposition, the sample is removed from the electrodeposition chamber, rinsed with deionized water, dried with N_2, and set on a 60°C hot plate for ten minutes until all fluid has evaporated. At this point we have Ni tubes of a given length, L_{Ni}, inside a PCTE template. Figure 4.12 is an SEM image of a larger Ni tube, fabricated to be 2 μm in diameter.

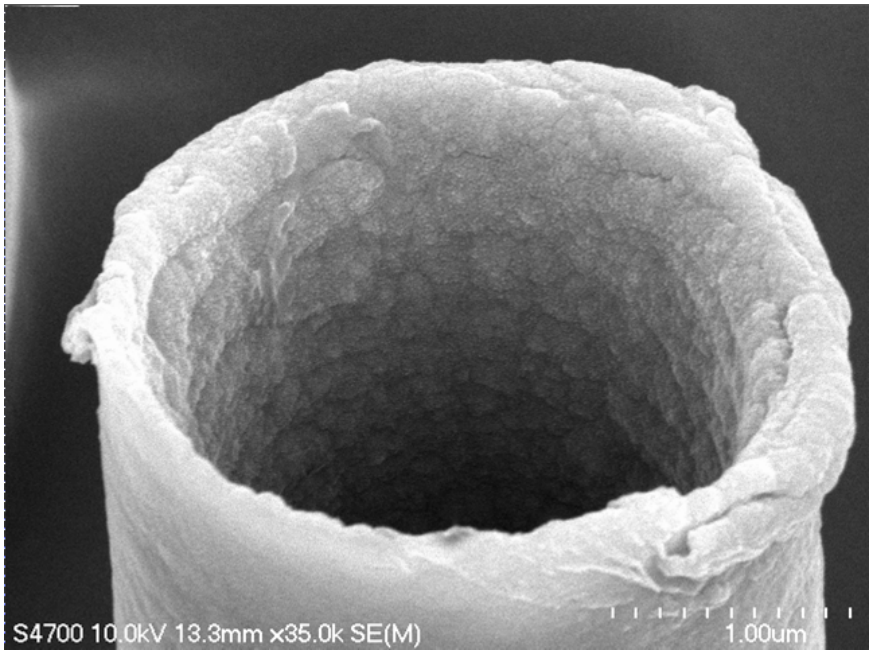

Figure 4.12: SEM image of a 3 μm diameter Ni tube.

I cut the 5 mm circular template into smaller 1 mm x 1 mm squares; each square is a biomimetic cilia array sample, and a sample contains on the order of 20,000 cilia. As illustrated in Figure 4.13C, every sample is immersed in PDMS, which is mixed at a 10:1 w/w polymer to curing agent ratio. The PDMS enters the pores and fills the Ni tubes, becoming the core in the core-shell structure.

Similar to the FFPDMS and FFPDMS-NH_2 fabrication processes, samples are placed inside a 200-300 μm tall PDMS well structure which was previously crosslinked into a solid and plasma-bonded to a glass coverslip. For core-shell samples, I ensure the metal-sputtered side of the membrane is facing upward to ensure the Ni tube will enclose the upper portion of the core-shell microrod. To evacuate any air bubbles, the sample is degassed for approximately ten minutes, and the PDMS is cured in an oven at 80°C overnight (Figure 4.13D).

After curing, the upper layer of PDMS and the metal-sputtered layer must be removed. Using a microscope and tweezers, I carefully remove the PDMS, and depending on the type of metal sputtered onto the sample, this layer is removed according to Table 4.2. After removing the upper layers, the dissolution process continues as it did for the FFPDMS and FFPDMS-NH_2. The entire template-well structure is immersed in DCM for two minutes (Figure 4.13E) and rinsed with ethanol containing 0.1% Triton-X without exposing the rods to air.

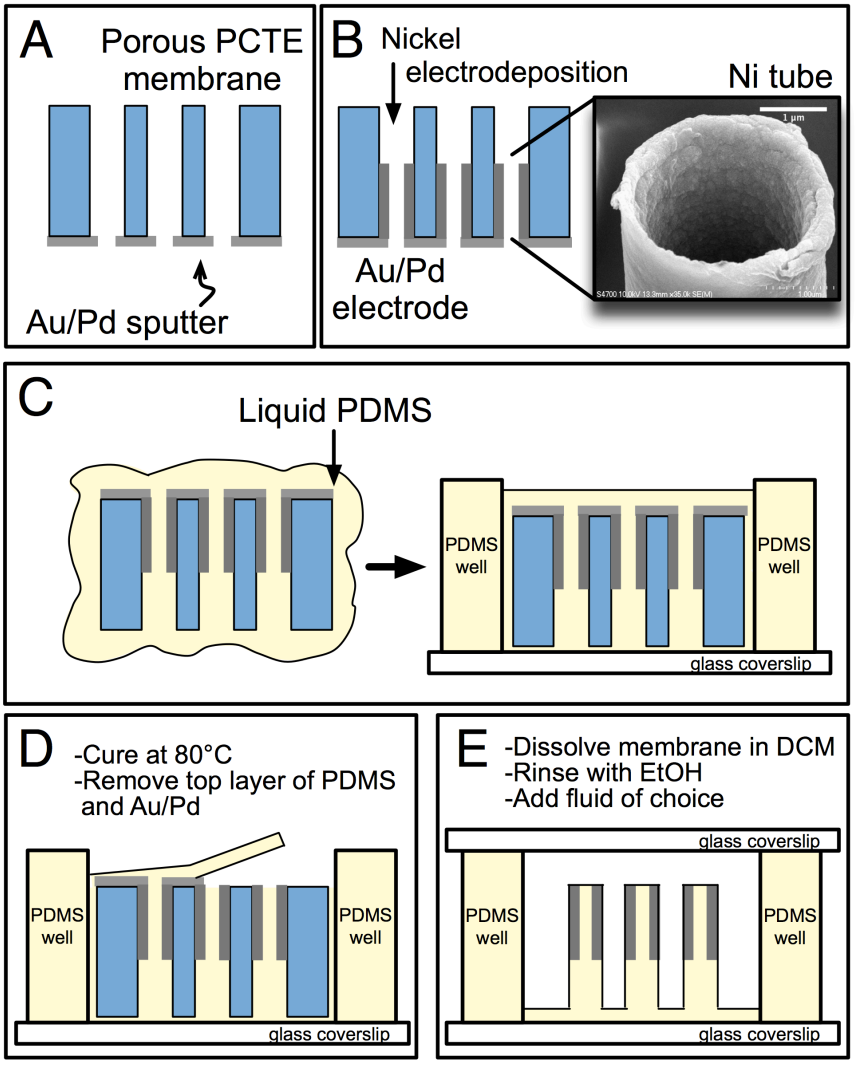

Figure 4.13: Cross-sectional view of core-shell cilia fabrication procedure. (A-B) Au/Pd is sputtered onto the PCTE membrane and serves as the working electrode for Ni electrodeposition. (C) PCTE membrane is immersed in uncured PDMS and set inside a PDMS well structure. (D) The sample is thermally cured, and the upper layer of PDMS and Au/Pd is removed to expose the PCTE membrane. (E) The PCTE membrane is dissolved with DCM, and cilia are rinsed with ethanol. The appropriate fluid is added, and the sample is sealed (Fiser et al., 2012).

Figure 4.14 consists of SEM images of critical point dried rod arrays. When fabricating core-shell cilia, we have two ways to control the length of the Ni shell, L_{Ni}: (i) alter the pore diameter of the PCTE template and deposit a specified amount of Ni, or (ii) alter the amount of Ni charge deposited into a given pore size. The two images in Figure 4.14 are

pore-size controlled.

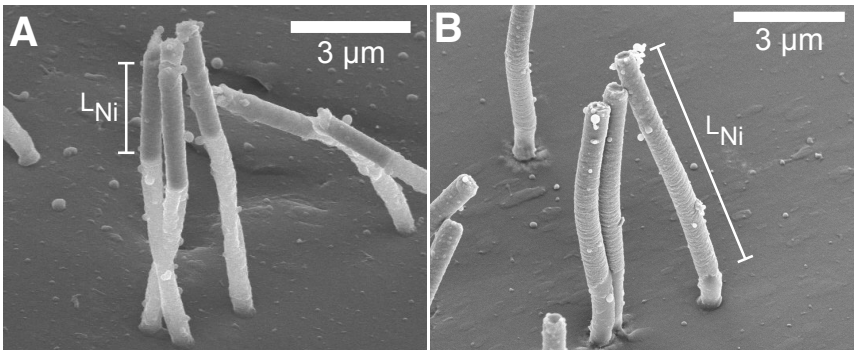

Figure 4.14: SEM images of core-shell cilia with various sizes of L_{Ni} taken on a 45°C tilted stage. The amount of Ni electrodeposited is identical, but the pore sizes are (A) 660 nm and (B) 590 nm.

I have utilized methods other than scanning electron microscopy for the characterization of these novel core-shell structures. Energy Dispersive X-ray spectroscopy (EDS), which is typically affixed to a scanning electron microscope, is a technique for the elemental analysis of a sample or field of view. From this, I may learn about the chemical composition of the material electrodeposited into the PCTE membrane which acts as the shell in the core-shell rod. Another technique which will provide a measure of the magnetic responsiveness of these structures is called SQUID magnetometry. This technique was used to measure the magnetizations of maghemite and magnetite nanoparticles as a function of applied magnetic field and previously described in Section 4.2.

4.3.2 Energy Dispersive X-ray analysis

To verify the presence of a Ni shell and PDMS core, I used Energy Dispersive X-ray spectroscopy (EDX or EDS), a technique that employs a high energy electron beam which penetrates a sample up to 2 μm deep to determine its composition. The electron beam

interacts with electrons in the inner shell of an atom, exciting and ultimately ejecting them from the shell. When new electrons from a higher energy shell move in to fill the vacancy, the characteristic differences in these higher energies and the lower energies of the inner shell are released as X-rays. The energies measured by EDS are energies characteristic to specific atoms from which they were emitted. Thus, this method will verify the elemental structure of core-shell rods.

The geometry of a sample determines the type of scan performed. Using Inca's EDS software, the user may specify a particular field of view, the shape of the area of a scan, the sampling resolution, and the scan time. I performed a line scan (Figure 4.15) to determine the elemental composition along the length of a rod. From left to right along the rod, a sharp signal change exists at the core-shell boundary. The Ni signal increases dramatically, and a corresponding decrease in silicon signal is observed as PDMS has a silicon-oxygen backbone. Several measurements such as these were performed on numerous rod array samples with differing Ni tube lengths.

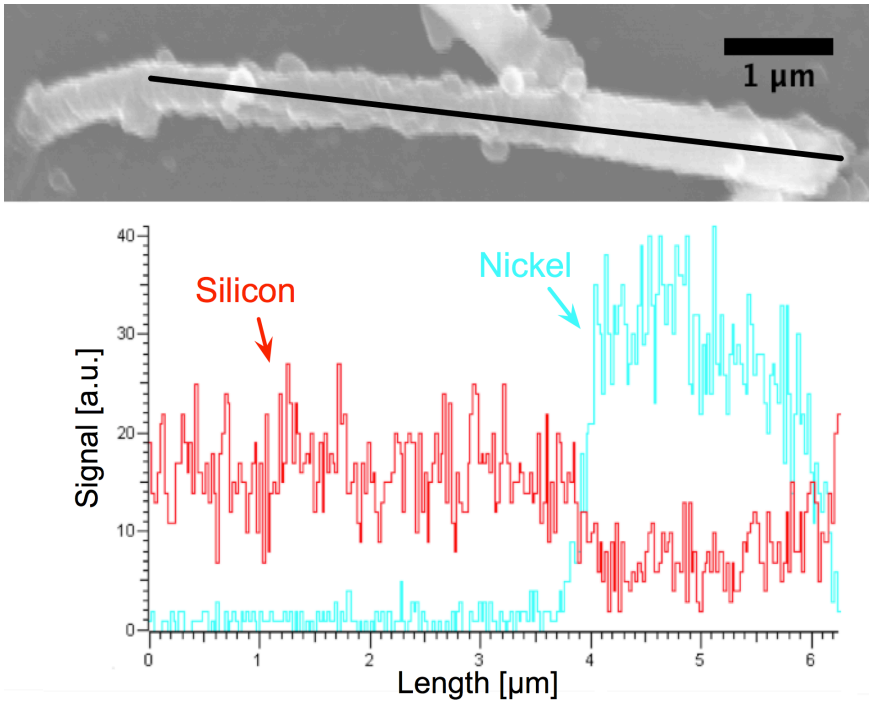

Figure 4.15: An Energy Dispersive X-ray Spectroscopy line scan of a 10 μm long and 660 nm diameter core-shell cilium with a Ni deposition of 2.04 mC/mm^2, resulting in a tube length of approximately 3.5 μm and thickness of 100 nm. At 4 μm into the scan, note the increase in Ni signal and decrease in the Si signal. This change in material can also be seen in the SEM image; the Ni appears as a bright portion at the right end of the rod (Fiser et al., 2012).

4.3.3 Applied field dependence

To characterize the magnetic properties of core-shell biomimetic cilia, I fabricated samples as described in Figure 4.13, but in this case, the rods remained inside the PCTE membrane. The final release step shown in Figure 4.13E was not performed. The arrays (encased in the PCTE membrane) were inserted into a straw holder such that the microrods' long axes were parallel or perpendicular to the applied magnetic field. All magnetization curves were run at 300°K. Initial runs over a large range of applied field determined that the nickel saturated at ±1400 Oe, and so future runs were performed over the range ±3000 Oe.

In addition, the magnetization of the background was obtained, and all data presented has been background subtracted.

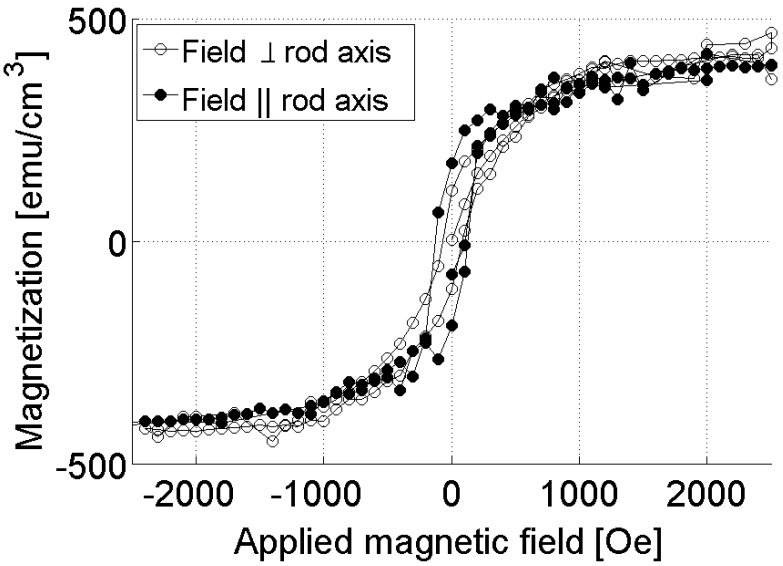

Figure 4.16: The magnetic field was applied both perpendicular (○) and parallel (●) to the rod axis, and the signal is normalized by the volume of Ni deposited into the PCTE membrane (Fiser et al., 2012).

The microrods' saturation was the same whether the field was applied parallel or perpendicular to the rods long axes, and the saturation magnetization was 397±13 emu/cm^3, a value that approaches saturation magnetizations in literature (Ferre et al., 1997; Kisker et al., 1995; Cordente et al., 2001). The ferromagnetic nature of core-shell cilia was confirmed by the presence of hysteresis in the curves. In addition, I checked for the presence of shape anisotropy which appears as a general shape change in the hysteresis curves when the magnetic field is applied in different orientations. As shown in Figure 4.16, data indicate there may be a subtle anisotropy. When the rods' long axes are aligned parallel to the applied field, the sample appears to approach saturation more quickly than when the rods' long axes are aligned perpendicular to the applied field. This phenomenon is expected as

more energy is required to rotate the moment of individual domains away from the long (easy) axis of the rod. Shape anisotropy has been shown in previous magnetization studies of Ni nanorods with packing densities less than 35%. Larger porosities (>35%) have exhibited a reduced anisotropy due to the dipolar coupling between rods, as shown in Figure 4.17 (Encinas-Oropesa et al., 2001). The porosity of rods in Figure 4.17A is 4%, and the porosity of rods in Figure 4.17B is 35-38%. I utilize PCTE membranes with a porosity of 0.31%.

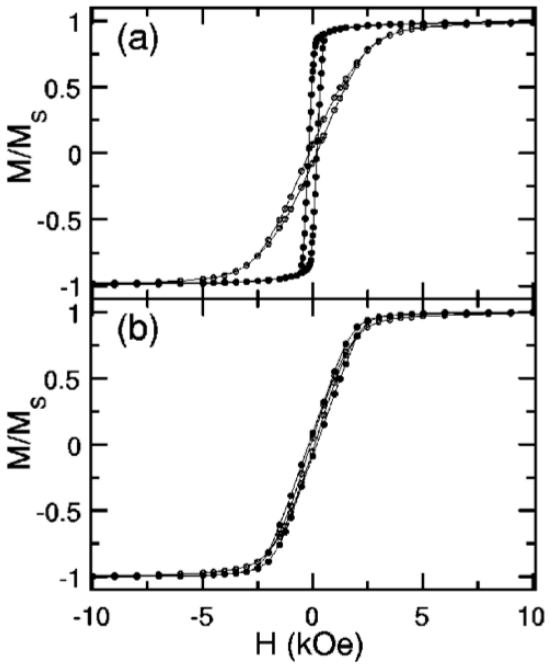

Figure 4.17: Reprinted from Encinas-Oropesa et al. (2009). The magnetic field was applied both perpendicular (open circles) and parallel (filled circles) to the rod axis, and the signal is normalized by the saturation magnetization. The Ni nanowires in (a) have a porosity of 4% and diameter of 56 nm, and in (b), the porosity is 35-38% and the diameter is 250 nm (Encinas-Oropesa et al., 2001).

Chapter 5

Magnetic Actuation

Magnetic forces, such as those generated by permanent magnets or electromagnets, offer an appealing solution to driving arrays of biomimetic cilia. The effect of a magnetic field may be long range, and for permanent magnets, no wires or internal, on-chip power sources are required. Additionally, large actuator displacements may be achieved, and a complex actuator response may be easily orchestrated by manipulating magnet geometries or placement. Permanent magnets are therefore a simple and commercially available method for the application of a magnetic field.

Magnetic fields are able to actuate biomimetic cilia through two different mechanisms: torque and force. The nickel tubes surrounding core-shell biomimetic cilia are ferromagnetic as can be seen in Figure 4.3.3, and are thus capable of retaining a magnetization after the magnetic field has been removed, though the hysteresis is slight. Typically at the microscale objects are superparamagnetic, such as FFPDMS cilia, and dipoles within the material do not remain aligned when a magnetic field is removed.

The torque which is applied to a dipole is (Jackson, 1998)

$$\vec{N} = \vec{m} \times \vec{B} \tag{5.1}$$

where B is the applied field and m is the magnetic dipole moment. If a dipole is aligned with the magnetic field, the torque on the dipole will give zero, and when the field and dipole are perpendicular, the torque will be a maximum; thus, the torque acts to align a dipole with the applied field. The force which is applied by the magnetic field to the dipole is (Jackson, 1998)

$$\vec{F} = \nabla(\vec{m} \cdot \vec{B}), \tag{5.2}$$

which is dependent on the direction of the greatest increase of $\vec{m} \cdot \vec{B}$. Thus, the magnetic field rotates a dipole and the field gradient pulls a dipole closer. In biomimetic cilia, dipoles within the nickel shell interact with one other and the torque and force are both minimized with a head-to-tail alignment along the long (or easy) axis of the cilium. If the long axis of the cilium is not parallel to the applied magnetic field, dipoles within the rod will attempt to align themselves with the field while maintaining their alignment with the cilium's long axis, causing a torque on the cilium. This torque minimizes the angle between the direction of the applied field and the dipoles. As discussed in Section 3.3.1, the effect of the magnetic gradient, and thus magnetic force, on the actuator is negligible.

I magnetically actuate biomimetic cilia arrays using rare-earth neodymium-iron-boride permanent magnets (K&J Magnetics) situated from 2-15 mm above the sample. The rectangular magnet is oriented such that the north and south ends are parallel to the sample plane. This effectively orients the magnet field in a direction perpendicular to the relaxed orientation of cilia, maximizing the applied torque on the rod. The distance between the magnet and sample controls the strength of the applied magnetic field, as shown in Figure

5.1, where the magnetic field was measured as a function of distance using a gaussmeter (F.W. Bell Teslameter, model 5080G). Each curve in Figure 5.1 represents measurements made with respect to a different location of the magnet.

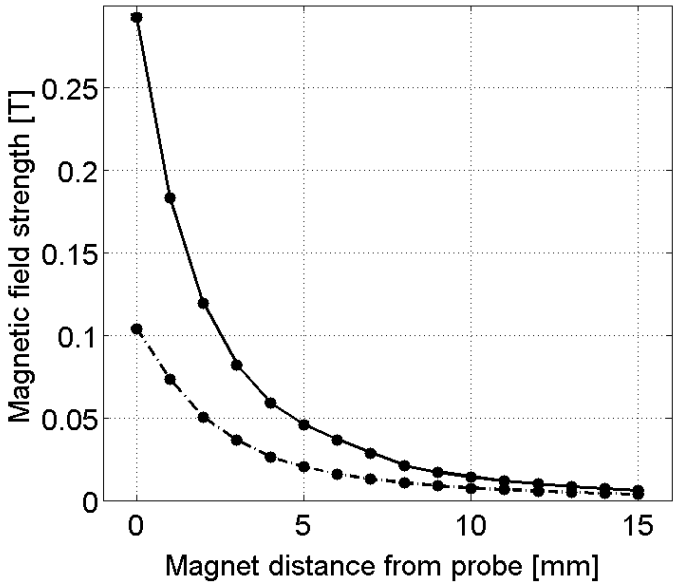

Figure 5.1: The permanent magnet used in all experiments had dimensions 1.0 in x 0.5 in x 0.25 in. The magnetic field was measured as a function of distance from the center of the 1 in x 0.5 in face of the magnet (solid line) and from the center of the 1.0 in x 0.25 in face of the magnet (dashed-dotted line). In experiments, the magnet is oriented with the 1.0 in x 0.25 in face of the magnet parallel to the sample plane.

In this chapter, I will first compare the responsiveness of composite FFPDMS rods and core-shell rods to an applied magnetic field in various fluids, and follow this by characterizing the abilities of core-shell rods in general. At the low end of the range of magnetic field strength achievable with commercially obtained neodymium magnets (1 in x 0.5 in x 0.25 in), ~5 mT, core-shell cilia achieve bend angles of approximately 20°. Increasing the field to a moderate 30−100 mT field strength causes the nickel portion of the cilium to bend a full 90° such that the tip of the cilium contacts the substrate and sticks momentarily. Bend

angles achieved by FFPDMS cilia, even at the higher applied fields approaching 200 mT, are no larger than 40°. In addition to the responsiveness from a given applied field, I will discuss how we utilize various magnetic setups and oscillating fields to engender actuator beat shapes similar to those of biological cilia.

5.1 Responsiveness of composite and core-shell actuators

Designing an actuator to be highly responsive requires the optimization of magnetic loading for a given geometry. This optimization was discussed in the context of Ben Evans' energy minimization model as utilizing the volume fraction of magnetic material at which an actuator achieves a maximum static deflection. This definition of 'optimal' implies that maximum actuation is the ultimate goal of an actuator. The goal of an actuator should depend on its application. Thus, a possible goal may also be to design an actuator with larger torque, such that it has the ability to deflect in a more viscous environment.

The design of FFPDMS, FFPDMS-NH_2, and core-shell actuators is strongly dependent on the application for which they will be utilized. The sacrifice of some deflection to achieve a higher torque in a higher viscosity environment may or may not be necessary. FFPDMS biomimetic cilia are highly damped in fluids with larger viscosities. This damping worsens as drive frequency increases. In PBS, a buffer with a zero-shear viscosity η_0 = 1.05 cP, FFPDMS cilia arrays actuate at appreciable amplitudes, approximately ~5-6μm (with bend angles on the order of 30°), but when actuated in 0.25% agarose, a viscoelastic fluid with η_0 ~630 cP, the bend angle and amplitude become nearly undetectable. Figure 5.2 shows minimum intensity projections of thirty second videos where two differ-

ent arrays of FFPDMS cilia are driven at 32 Hz in both buffer and 0.25% agarose. Each dark oval shape is the motion of a cilium tip over the course of thirty seconds.

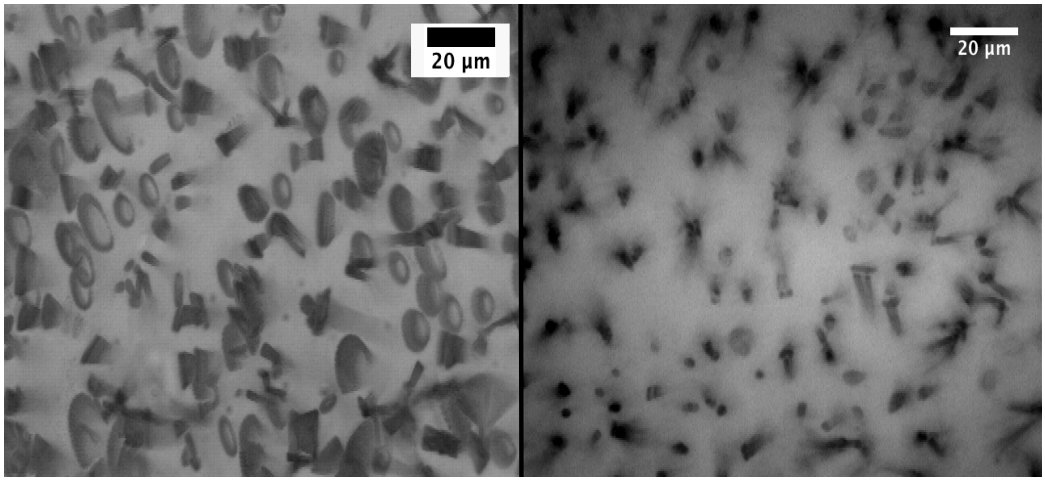

Figure 5.2: Minimum intensity projection of two different FFPDMS cilia arrays (25 μm long, 800 nm diameter) driven at 32 Hz in PBS (at left) and 0.25% agarose (at right) with a maximum applied field of ~130 mT. The viscosity of 0.25% agarose (~600 cP greater than PBS) restrained nearly all cilia motion. The amplitude decreases from ~5.5 μm to an average of 0.8 μm, decreasing to 9% its original value.

In higher viscosity environments, core-shell cilia are preferable as they are capable of maintaining larger amplitudes and applying higher forces to the fluid. Figure 5.3 shows minimum intensity projections of core-shell cilia actuated at 16.3 Hz. The left image is in PBS buffer (η_0 = 1.05 cP) at an applied field of 11 mT, and the right image is in 0.25% agarose(η_0 = 630 cP) at an applied field of 125 mT. The low magnetic field needed to obtain large amplitude in buffer indicates the large responsiveness of these arrays. The rod amplitude is diminished in a fluid 660 times more viscous, but still easily detectable and has been marked on the figure. Amplitude decreases from approximately 5 μm in PBS to 1.5 μm in 0.25% agarose. Note that these core-shell cilia are less than half the size of FFPDMS cilia, and the applied field in buffer necessary to achieve large core-shell

amplitudes is 9% of the field required to achieve large FFPDMS amplitudes.

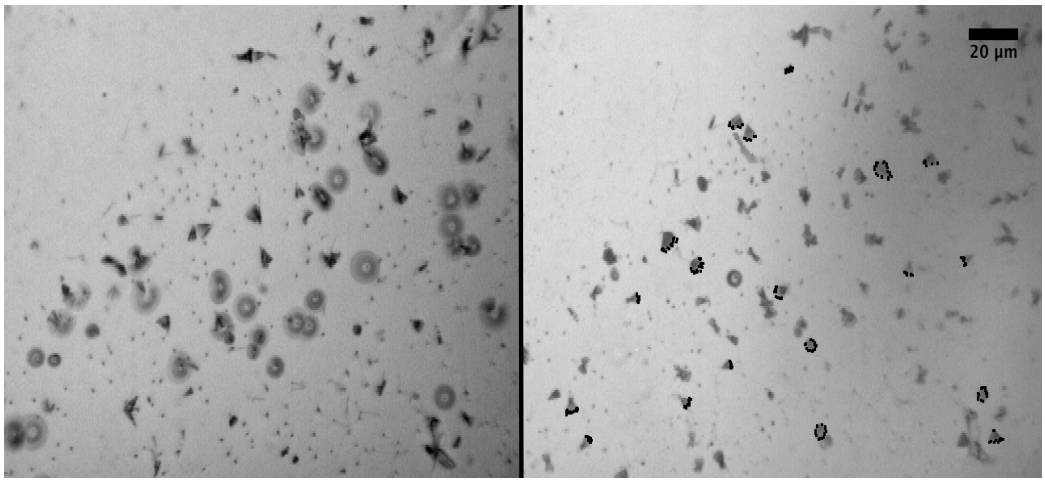

Figure 5.3: The same core-shell cilia array (10 μm long, 550 nm diameter) driven at 16.3 Hz in PBS (at left) and 0.25% agarose (at right). The applied magnetic field at left is 11 mT, and the applied field at right is 125 mT. From PBS to 0.25% agarose, the amplitude decreases from 5 μm to 1.5 μm, a decreasing to 28% its original value. Recall that core-shell cilia are less than half the size of FFPDMS cilia, and the amplitude for FFPDMS cilia decreased to 9% its original value.

I have also looked at core-shell arrays in a purely viscous environment, as the elasticity of agarose may greatly contribute to the dampened amplitude. Minimum intensity projections of core-shell cilia beating at 8 Hz in both buffer and 2.5 M sucrose ($\eta_0 \sim 100$ cP) are shown in Figure 5.4. For the same array, the bend angle remains nearly unaffected by the fluid's viscosity, 55°±5° to 46°±3°, respectively.

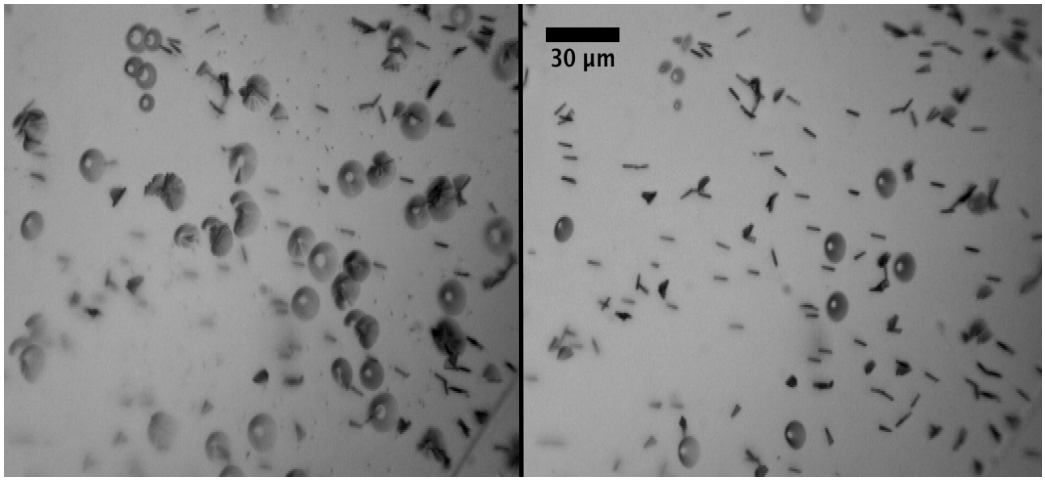

Figure 5.4: Minimum intensity projection of the same core-shell cilia array (10 μm long, 550 nm diameter) driven at 8 Hz in PBS (at left) and 2.5 M sucrose (at right). The act of exchanging sucrose for PBS (or vice versa) causes some rods to collapse. Rod amplitude decreases little when the array is transferred to a fluid nearly 100 times more viscous.

In addition to exhibiting a high static responsiveness, core-shell cilia maintain their responsiveness with an increase in frequency. Figure 5.5 shows amplitude measured as function of frequency for both FFPDMS cilia and core-shell cilia. Note the offsets on the y-axis. The applied magnetic field for core-shell cilia was 11 mT, and the applied magnetic field for FFPDMS cilia was ~100 mT. With 11% of the magnetic field, core-shell achieve a larger amplitude. For core-shell cilia, increasing the frequency from 0.65 to 16 Hz reduces the amplitude by only ~7%. For FFPDMS cilia, increasing the frequency from 2.9 to 10.3 Hz reduces the amplitude by ~10%. Linear fits indicate a decrease in amplitude from 0.65 to 32 Hz of only 13% for core-shell cilia, and 24% for FFPDMS cilia. Some change in amplitude as a function of frequency is desirable when measuring viscoelastic parameters; however, if the amplitude decrease is too large, the actuator may become ineffectual, as was described in Figure 5.2 for FFPDMS cilia.

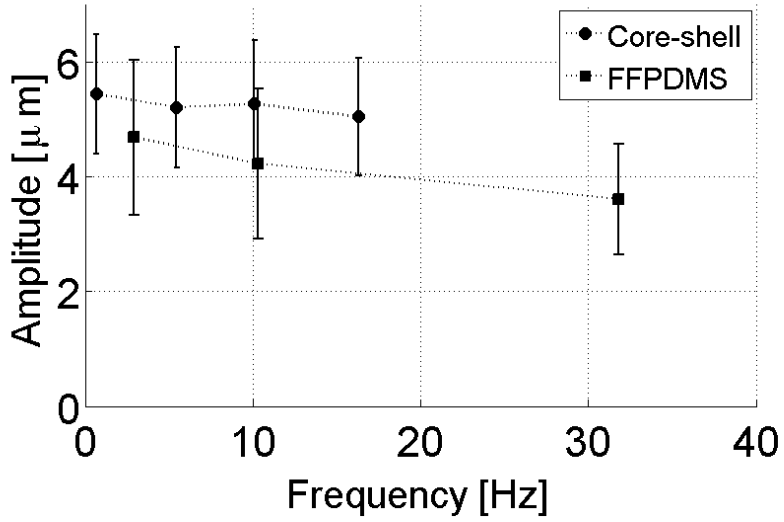

Figure 5.5: Rod amplitude as a function of frequency in PBS. Error bars represent standard deviation. The change in amplitude from 0.65 Hz to 16.3 Hz is ~7% for core-shell actuators. For FFPDMS actuators, the change from 2.9 Hz to 10.3 Hz is ~10%, and from 2.9 Hz to 32 Hz, the amplitude drops ~23%. The dashed lines connecting each point is only for visual purposes, though a least squares fit was performed for core-shell cilia and may be found in Section 7.1. Note that different fields were applied for the two cilia arrays: ~100 mT for FFPDMS cilia and ~11 mT for core-shell cilia.

5.1.1 The power of the core-shell structure

Because of the high responsiveness of core-shell biomimetic cilia, applying a low magnetic field of 30 mT induces a bend angle of the nickel portion of the rod greater than 90°. This large bend angle is shown in Figure 5.6 when, at the maximum extension of the rod's tip from its equilibrium position, the tip contacts the substrate and remains for several frames of video. The left image in Figure 5.6 is a minimum intensity projection of two seconds of a single rod's path. Each dark stroke is a single video frame of the rod's motion. All rods within the camera's field of view performed similarly, contacting the substrate at the same instant. The image at right in Figure 5.6 is the rod's average angular velocity as a function of time for a single rotation. The asterisks in both the image and the plot denote

the portion of the beat where bending of the Ni tube is greater than 90° at the Ni-PDMS interface. The Ni portion contacts the substrate and is restrained for one-tenth of a second. Following this restraint, there is a large spike in angular velocity as the rod tip 'pops' off the substrate fairly quickly. Another interesting portion of the beat is indicated by arrows in the minimum intensity projection. Because the array is imaged in a reflectance brightfield mode, the Ni tube reflects light back to the camera when it is horizontal.

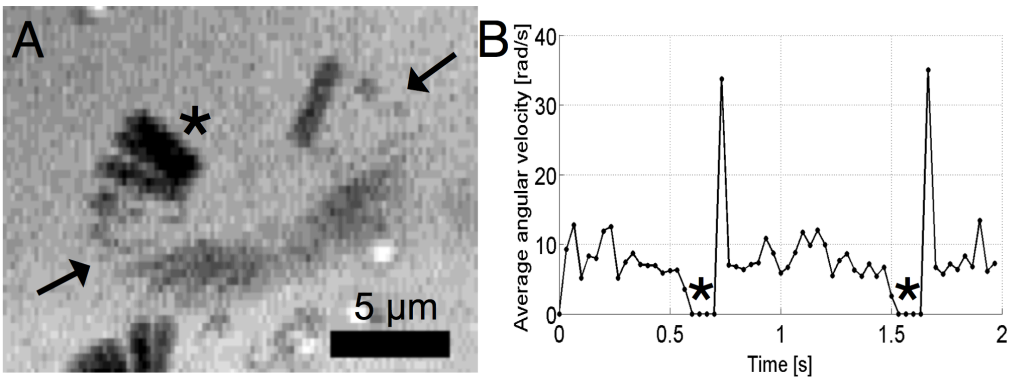

Figure 5.6: With a 30 mT magnetic field, we can actuate the rods such that their Ni tubes contact the substrate. The left image is a time lapse image of two seconds of a single rod's rotational beat. Arrows denote a brighter region where light reflects off the horizontally-oriented Ni tube. The plot at right is average angular velocity as a function of time for the same rod. Asterisks in both indicate where the Ni tube bends more than 90° to contact the substrate.

5.2 Mimicking the biological cilia beat shape

Motile biological cilia are known to beat in two different physical patterns, a planar beat and a tilted conical beat. An example of cilia which exhibit the linear beat pattern are lung epithelial cilia. They beat with a forward effective stroke where the cilium fully extends itself upward away from the cell surface and a backward recovery stroke where the cilium bends low and close to the cell surface. During the effective stroke, mucus is propelled up

the lung and toward the throat, and during the recovery stroke, the cilium is close to the no-slip boundary condition of the cell surface, thereby inhibiting flow deeper into the lung. The tilted conical beat pattern is executed by vertebrate embryonic nodal cilia. The tips of nodal cilia move in a circular pattern which is not centered around the cilium base, but around a tilted axis, such that during part of one beat rotation, the tip of a nodal cilium is closer to the no-slip boundary condition at the cell surface. The net motion of the fluid is in the cilium tip's direction when it is farthest from the cell surface. Figure 5.7 is a diagram of both the lung epithelial cilia beat shape and the vertebrate embryonic nodal cilia beat shape.

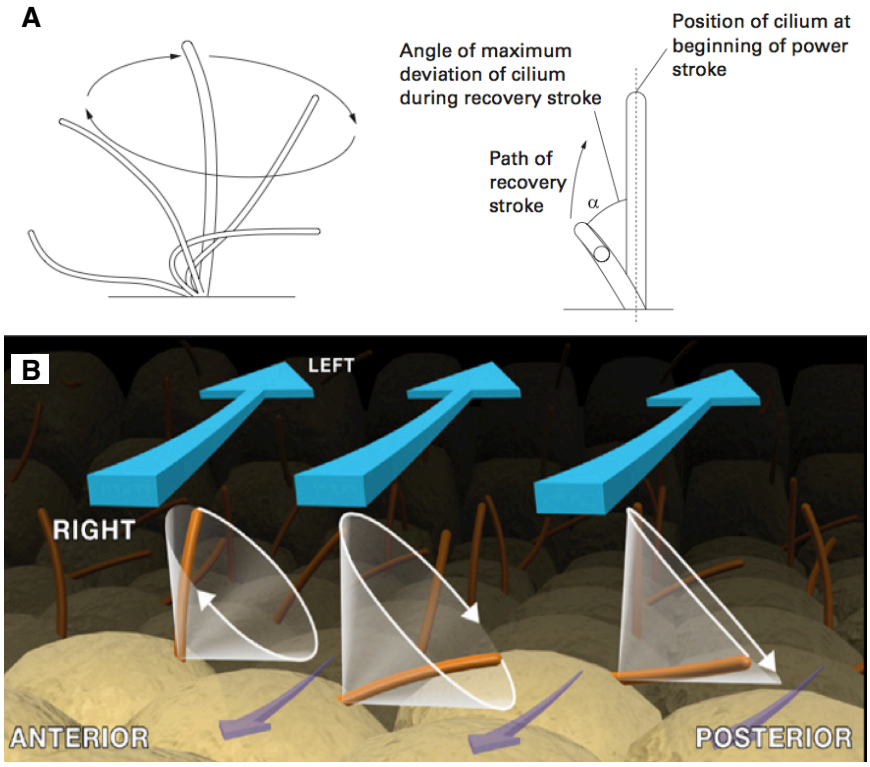

Figure 5.7: (A) Reprinted from Chilvers et al. (2000). Diagram of the linear beat shape performed by lung epithelial cilia (Chilvers and O'Callaghan, 2000). (B) Reprinted from Hirokawa et al. (2006). Diagram of the tilted conical beat shape exhibited by vertebrate embryonic nodal cilia. Blue arrows indicate the direction of nodal flow; purple arrows indicate viscous drag (Hirokawa et al., 2006).

5.2.1 The linear beat

To drive a linear beat, I utilize a variable frequency motor and multiple permanent magnets (K&J Magnetics) with dimensions 1.0 in x 0.5 in x 0.25 in. These permanent magnets are affixed to a disc-like structure which is then attached to a variable speed motor's shaft (Figure 5.8A). Four magnets sit on the edge of the disc equidistant from one another, and the disc is positioned such that its edge passes over the biomimetic cilia sample, producing the beat shape illustrated in Figure 5.8B. Currently, I have only utilized the planar beat shape for the technological application of core-shell cilia as detectors of the onset of blood coagulation, which I discuss in Chapter 7.

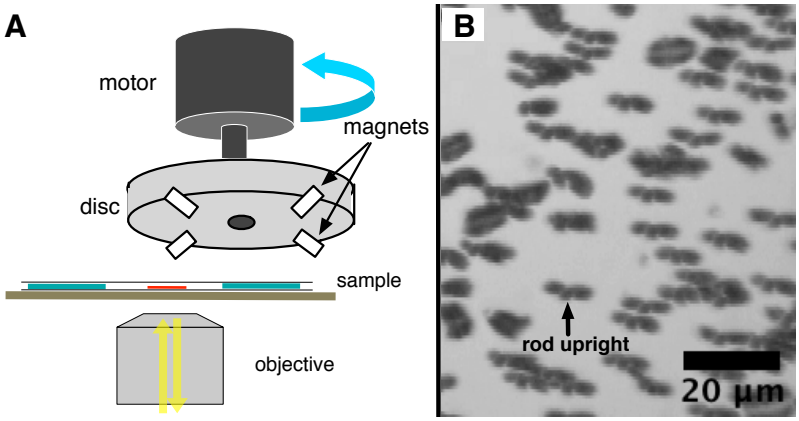

Figure 5.8: (A) Magnet set-up utilized to drive a linear beat. Permanent magnets are affixed to the edge of the disc with any spacing between them. The entire disc is affixed to a rotating motor, causing each magnet to pass over a cilia array. (B) Minimum intensity projection of the linear beat of core-shell cilia driven by the disc-magnet set-up in (A). The center spot of each dark object is the cilium's upright position; the two dark spots on either side represent the cilium's excursions as it follows the magnetic field. A description of the torque applied to a cilium as the magnet passes the sample is detailed in the text and in Figure 5.9.

To understand the effect of the passing magnets on the cilia array, I consider a single cilium. When no magnet is present over the cilium, the cilium remains upright. As a

magnet nears, the magnetic field induces the alignment of dipoles within the nickel portion of the rod, assuming the rod has no prior magnetization. These dipoles seek to maintain the alignment of the rod's long axis with the magnetic field lines as the magnet passes over the cilium, applying a torque to the rod. Initially, as the magnet nears, and the magnetic field is at an angle between 0° and 90° with respect to the vertical; the rod bends to align with the field. When the magnet is oriented such that the field is 90° with respect to the vertical (parallel to the sample plane), the rod is approaching its largest deflection. As the magnet passes, and the angle between the field and the vertical becomes greater than 90°, the rod again seeks to align itself with the field. Since both the substrate and material comprising the rod prevent it from bending greater than 90° and since core-shell rods are ferromagnetic, within at most 33 ms for a 2 Hz beat, the rod orients itself at an angle left of the vertical, aligning itself antiparallel to the direction of the magnetic field. Figure 5.9 illustrates this actuation. Ben Evans energy minimization model can be utilized to predict energy minima which correspond to the angle of the applied magnetic field; details can be found in his thesis where this phenomena is called the 'snap-beat' and described for superparamagnetic cilia (Evans, 2008).

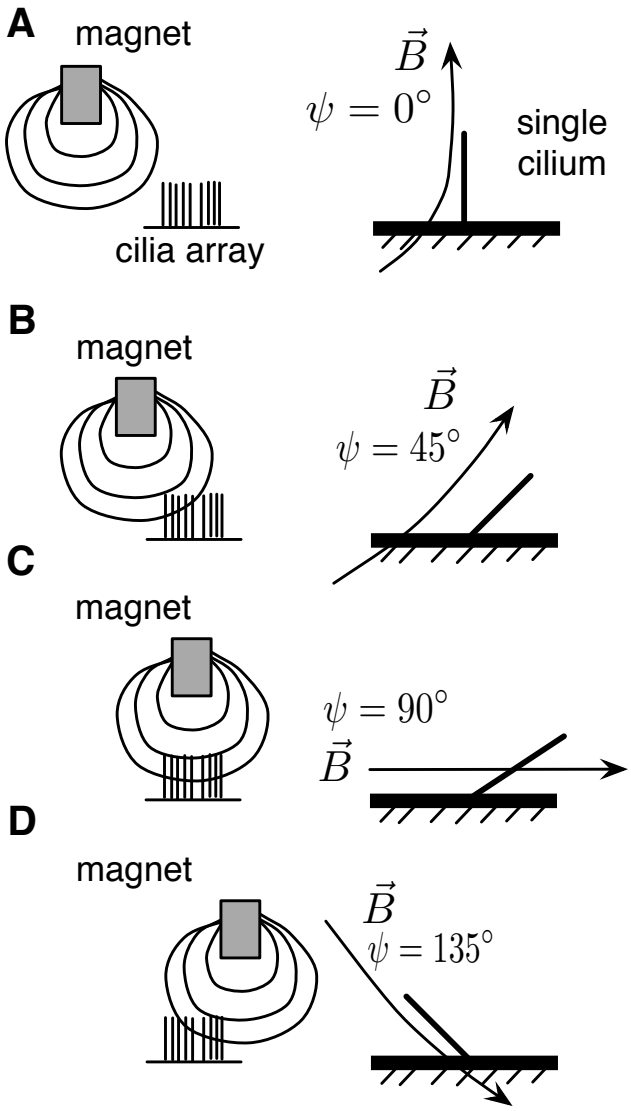

Figure 5.9: (A) When the magnet approaches the cilium, the magnetic field is at an angle of 0° with the vertical, and the cilium feels no torque, remaining upright. (B) As the magnet nears, the magnetic field is at an angle between 0° and 90°. The rod feels a torque aligning it with the field. (C) When the magnetic field is at 90°, parallel to the sample plane, the rod attempts to maintain its alignment. (D) As the magnet continues past the cilium, the field approaches an angle greater than 90°. At this point, material parameters may prevent the rod from following the field's increasing angle with respect to the vertical. Experimentally, the rod is seen to physically 'snap' from the right side of the vertical to the left side of the vertical, in an attempt to become anti-aligned with the magnetic field. This 'snap' happens within at most 33 ms for a 2 Hz beat.

In the minimum intensity projection in Figure 5.8B, the beat frequency of cilia is 2 Hz,

meaning two of the four magnets securing to the rotating disc pass over the array every second. The disc itself is approximately 16.5 cm in diameter. For the same applied voltage and number of permanent magnets, a larger diameter disc would result in a lower beat frequency. The entire passage of a single magnet, the period of a rod's beat, is approximately one-third of a second.

5.2.2 The tilted conical beat

To perform the tilted conical beat, a permanent magnet is affixed to the shaft of a rotating variable speed motor. The magnet is attached such that its poles are oriented parallel to the sample plane, as shown in Figure 5.10A. This orientation causes the magnetic field at or near the sample to also be parallel to the sample plane. As the motor and magnet rotate from 0° to 360°, the magnetic field rotates from 0° to 360°, and a cilium which follows the magnetic field will follow this circular rotation. As illustrated in Figure 5.9C, when the magnetic field is nearly 90° with respect to the vertical, the cilium's bend anglewill be as large as possible, restrained by its material parameters. This bend angle is analogous to the tilt angle plus half cone angle depicted in Figure 5.10B. Since the permanent magnet is fixed in space, the angle between the magnetic field and the vertical axis does not change. The permanent magnet does, however, rotate in space, and in spherical coordinates the angle swept out is ϕ, where $0 \leq \phi < 2\pi$. As the permanent magnet and thus the magnetic field rotates, the cilium follows.

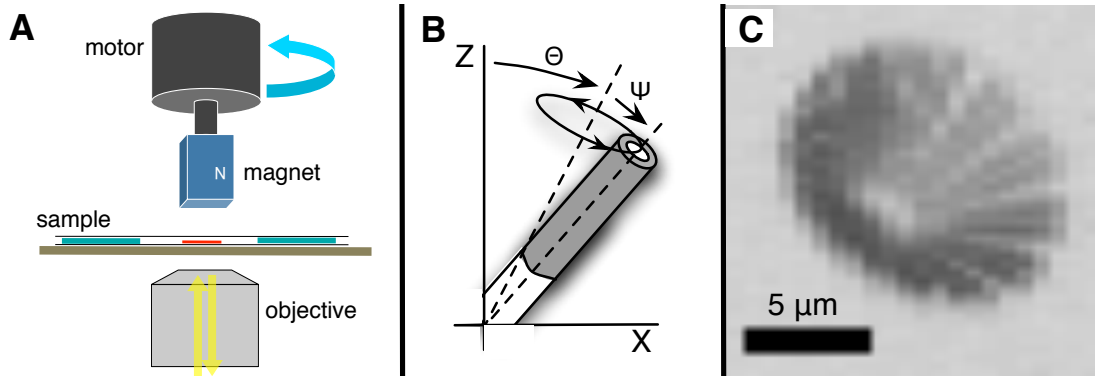

Figure 5.10: (A) Magnet position with respect to the sample is characterized by the magnet's height above the sample, and the magnet's x-offset from the sample center. For reference, the microscope stage and objective are included in the diagram. (B) The x-offset controls the direction of the magnetic field experienced by the cilia array and thus the tilt angle θ of a cilium as further detailed in Figure 5.11. The distance from the magnet to the sample controls the strength of the magnetic field and thus the half cone angle ψ. (C) Minimum intensity projection of a top down view of single rod performing the tilted conical beat.

The distance from the permanent magnet to the cilia sample affects the strength of the applied magnetic field. A shorter distance between magnet and sample will increase the field strength, thereby increasing the amplitude and half cone angle ψ (as illustrated in Figure 5.10B) of the cilium. In addition, offsetting the center of the permanent magnet laterally with respect to the cilia array affects the axis around which cilia rotate. Figure 5.10C is a top down view of a time lapse minimum intensity projection of a single core-shell rod performing this tilted conical beat shape. Each dark line denotes a position of the rod, the darkness of which is caused by the Ni tube. When the x-offset is zero, the magnet is directly above the cilia array such that the rotational axis of the magnet is aligned with the cilium's axis. As shown in Figure 5.11A, a cilium responds to this magnet orientation with an upright, conical beat shape. The tilt angle $\theta = 0°$.

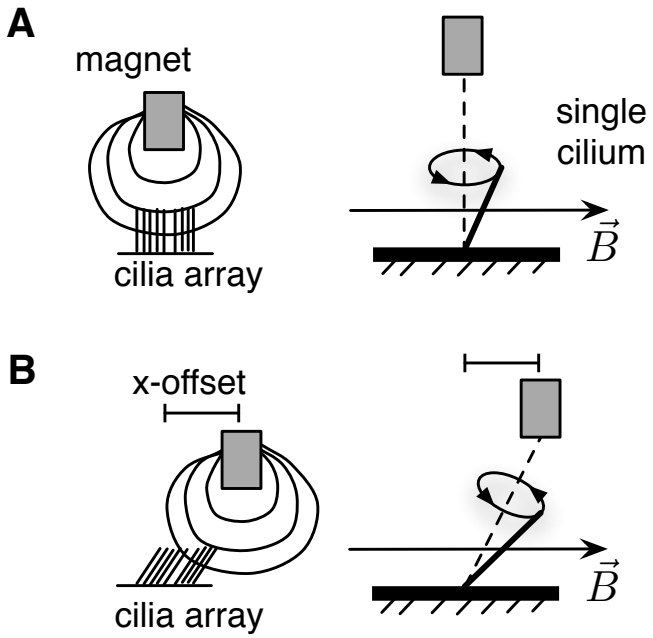

Figure 5.11: (A) When the axis of the permanent magnet is aligned with the cilium's rotational axis, $\theta = 0°$. The cilium will rotate as the magnetic field rotates, and its half cone angle ψ will be determined by the magnetic field strength. (B) When the axis of the permanent magnet is offset by some x, the cilium's rotational axis attempts to align itself with the magnet's axis producing a nonzero θ. The cilium will then rotate around its tilted axis as the magnetic field rotates.

With the introduction of an x-offset between the magnet center and cilia array, a cilium's rotational axis will point toward the magnet's center rather than vertically, tilted at an angle θ. As a laterally offset magnet rotates, a cilium will beat around its newly tilted axis, and the half cone angle ψ is measured with respect to θ, as shown in Figure 5.11B. A larger x-offset induces a larger tilt angle. The asymmetry in beat shape produced by the offset of the magnet is integral to achieving fluid flow at the microscale, as theoretically detailed by Smith et al. (2008). Fluid flow at the microscale will be discussed in Chapter 6.

A cilium's tilt angle, bend angle, and beat amplitude are measured using brightfield videos. To determine the tilt angle θ and half cone angle ψ as shown in Figure 5.10B, the

straight line displacement from the rod's base to its tip's nearest and farthest extent (d_1 and d_2) in the direction of the tilt are measured over one beat cycle, as shown in Figure 5.12.

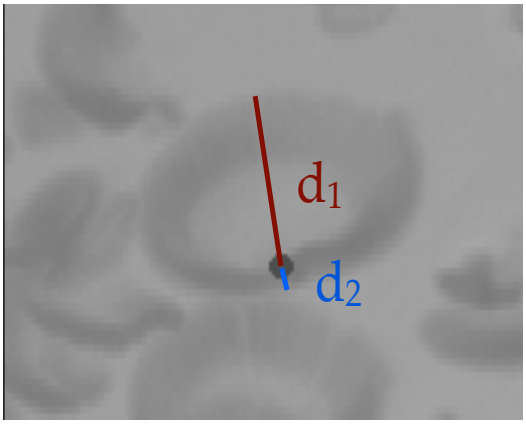

Figure 5.12: Minimum intensity projection of the cilium's path over the course of several beats. The tilt angle θ is calculated by first measuring the nearest and farthest extent of the cilium tip with respect to its base and then utilizing Equation 5.3. The bend angle is found using d_1 and the rod's known height.

The tilt angle θ is then

$$\theta = 1/2\left(sin^{-1}(d_1/L) + sin^{-1}(d_2/L)\right), \tag{5.3}$$

and the half cone angle ψ is

$$\psi = \theta - \left(sin^{-1}(d_1/L)\right). \tag{5.4}$$

The bend angle is determined by measuring the farthest straight line displacement of the rod's tip from its base, or $\theta + \psi$ which is equivalent to d_1 in Figure 5.12, and using the rod's known height of $L = 10$ μm. In order to measure the amplitude of the cilium, the path traced out by the cilium tip is fit to an ellipse, and the amplitude is one-half the length of

the ellipse's major axis. The amplitude is measured in this way to control for varying tilt angles across biomimetic cilia specimens.

This tilted conical beat shape is the shape utilized for all experiments discussed in Chapter 6. I have not yet been successful in replicating the asymmetrical planar beat employed by biological airway cilia. However, with the tilted conical beat, I am able to compare my flow results in aqueous fluids directly to the biological cilia-driven flow in vertebrate embryonic nodes, the ultimate illustration of the utility of a system such as mine.

5.3 Tracking the fluid motion

To image the flow produced by biomimetic cilia beating with a tilted conical beat shape, fluids are seeded with one micron red latex fluorescent microspheres (FluoSpheres). (Throughout this thesis I will interchangeably use microspheres, tracers, and tracer particles to indicate the particles I utilize to track flow in biomimetic cilia arrays.) Depending on the fluid, the microspheres may or may not be PEGylated, a process which binds low molecular weight polyethylene glycol (PEG) to a microsphere's surface to reduce (or neutralize) its surface charge. If using polymer solutions such as mucus or guar, coating microspheres' surfaces with PEG reduces the potential that beads will become attached to the polymer matrix and cease their thermal and/or driven motion. In an aqueous solution such as buffer PEGylation does not affect the motion of microspheres. Additionally, in some polymer solutions such as agarose, diffusion measurements taken by David Hill, a research associate with the Cystic Fibrosis Center at UNC-Chapel Hill, also indicate that PEGylation has little effect on microsphere motion.

To investigate the flow above and below the array of biomimetic cilia, the focal plane of the objective is changed in increments of tens of microns, and both brightfield and fluorescent videos are taken using a Pulnix camera, model TM-6710CL (JAI, Inc.), and an EDT-PCI DV (Engineering Design Team) frame grabber card. With fluorescence, videos may be captured close to and within the cilia layer without interference from moving cilia. In each video, the fluorescent microspheres are tracked using CISMM's Video Spot Tracker (cismm.org/downloads), and velocities are extracted using in-house Matlab scripts.

Chapter 6

Fluid Transport in Aqueous and Viscoelastic Fluids

The thrust of this thesis thus far has concentrated on the design and realization of fabricated microstructures in the same physical parameter space as biological cilia. Because biological cilia are responsible for propelling both aqueous and viscoelastic fluids, creating an identically sized biomimetic system has been an important endeavor. In hydrodynamics, viscous and viscoelastic fluids are characterized by a group of dimensionless numbers which represent the dominant forces and timescales in a fluid. In order to use an experimental apparatus, such as biomimetic cilia, at a larger scale and accurately represent fluidic phenomena, all dimensionless numbers characterizing the experiment must be equivalent (Metzner et al., 1966). For purely viscous fluids, this is a relatively simple undertaking as the Reynolds number is the significant dimensionless number that must be scaled. Any purely viscous fluid may be utilized in a macro-scale experiment, producing similar results to a micro-scale experiment, if the Reynolds number is equivalent. For viscoelastic fluids, the Reynolds number, Deborah number, and Weissenberg number must all be scaled with the physical dimensions of the experiment. This scaling is nearly impossible unless the

exact same fluid is used every time; it is difficult to make any generalization concerning all three dimensionless numbers for viscoelastic fluids (Metzner et al., 1966). For these reasons, core-shell biomimetic cilia are an ideal system for the study of fluid propulsion at the micro-scale, being the only system currently capable of viscoelastic fluid propulsion at the scale of biological cilia.

In addition to dimensionless numbers, the field of fluid dynamics has developed a number of constitutive relations to understand how, for a particular fluid, stress and shear (or strain) rate are related. Purely viscous fluids, also called Newtonian fluids, which exhibit a linear relationship between stress and shear rate with a proportionality constant that is the fluid's viscosity, are understood analytically for a number of problems with simple geometries. The introduction of a little complexity, however, may require the use of computational methods. As such, very little is understood about viscoelastic fluids, or non-Newtonian fluids, which are fluids that exhibit a time dependent response to an applied stress or strain.

In this chapter, I will first give a brief review of the relevant hydrodynamics including an overview of the three significant dimensionless numbers used to describe both viscous and viscoelastic fluids, the governing equation in fluid dynamics, the Navier-Stokes equation, and canonical solutions for both viscous and linear viscoelastic fluids, including Stokes' 1st and 2nd problems. Following this will be an analysis and extensive discussion of the characteristics of fluid flow driven by biomimetic cilia in both aqueous (Section 6.2) and viscoelastic (Section 6.3) fluids. Biological cilia are responsible for driving flow in multiple kinds of fluids including both buffer-like (aqueous) and mucus-like (viscoelastic) fluids. Thus, it is important to utilize our biomimetic platform to understand driven flow in both

environments.

Our theoretical understanding of viscous and viscoelastic fluids far surpasses our experimental understanding, especially as it pertains to biological systems. By using simple theoretical models for viscous and viscoelastic fluids and treating my biomimetic cilia tips as a single moving boundary (also known as coarse-graining), I am able to gain insight into the fluid dynamics of the system and apply this insight to both embryonic nodal cilia and lung epithelial cilia.

In the purely viscous, or aqueous, fluid, both FFPDMS and core-shell cilia are capable of driving transport with the tilted conical beat shape. The hydrodynamic model which supports the experimental data considers the motion of all cilia as a single translating plane and is a superposition of two canonical solutions to the low Reynolds number Navier-Stokes equation. This model was first identified in our publication in 2010 (Shields et al., 2010) and has been expounded upon in significant detail by Adam Shields in his dissertation (Shields, 2010).

In viscoelastic fluids, FFPDMS cilia are incapable of maintaining a sufficiently large amplitude to attain flow, and thus all presented results were collected with core-shell bioimimetic cilia. The data for flow in a viscoelastic fluid at low Reynolds number is markedly different than purely viscous flow, and to better understand these differences, I first apply the purely viscous models to the viscoelastic data. These models are quickly shown to be insufficient at explaining the fluid dynamics and a model which better incorporates the elastic contributions of a viscoelastic fluid is discussed.

6.1 Review of microscale hydrodynamics

6.1.1 Dimensionless Numbers

The field of hydrodynamics utilizes numerous dimensionless numbers which are useful in characterizing the dominant phenomena in an environment. Three dimensionless numbers used to describe both the environment in which cilia live and the characteristics of the fluid surrounding cilia are the Reynolds number, the Deborah number, and the Weissenberg number (Metzner et al., 1966).

These dimensionless numbers are often called scaling relations; a system may be scaled as large or small as necessary and still exhibit the same fluidic phenomena if the dimensionless numbers which correspond to length and time scales within the experiment are equivalent. For purely viscous fluids, the dominant dimensionless number is the Reynolds number, *Re*, which relates inertial forces to viscous forces. Thus to explore aqueous fluid dynamics, with a constant *Re*, we can apply fluid dynamics solutions at the microscale to the macroscale and vice versa (Macosko, 1994).

When time becomes a variable, as it does with viscoelastic fluids, multiple dimensionless numbers must be utilized to characterize the system including the Reynolds number. The Deborah number *De* is the primary dimensionless number, and it relates the time scale of the fluid to the time scale of the experiment. In addition to *Re* and *De*, the Weissenberg number *We*, which characterizes the elastic contribution to the nature of the fluid, is also of considerable importance for viscoelastic fluids (Metzner et al., 1966; Liu et al., 1998). I discuss each of these dimensionless numbers briefly below.

Reynolds Number

Biological cilia and other microorganisms live in an environment completely different from ours. If a force is applied to a microorganism, and suddenly the force is removed, the microorganism's motion also stops nearly instantaneously. When inertia is irrelevant and the viscosity of the surrounding environment becomes significant, the ratio of inertial to viscous forces, called the Reynolds number, becomes very small. The Reynolds number, Re, is defined as (Purcell, 1977)

$$Re = \frac{inertial forces}{viscous forces}. \tag{6.1}$$

At low Reynolds number, every motion is reversible and time invariant. The speed at which an action is performed does not affect the outcome of the action. This is best illustrated by the famous scallop theorem put forth by Purcell (Purcell, 1977). To move in its environment, a scallop opens its shell slowly and closes its shell quickly to expel water and push itself in a forward direction. In a low Reynolds number environment where speed of motion (time rate of change of direction) has no effect, the scallop is effectively performing a reciprocal motion, opening and closing its shell in the same configuration. When the configuration is symmetrical, the scallop does not achieve net displacement and is trapped in place. For microorganisms like the scallop or microstructures like cilia that rely on their bodies' motions to displace themselves, the motion must be asymmetric in space to achieve net transport (Purcell, 1977).

Explicitly, the Reynolds number is written as

$$Re = \frac{vl\rho}{\eta}. \tag{6.2}$$

where v and l are the characteristic velocity and length scales of the system (which may vary from system to system), ρ is the fluid's density, and η is the fluid's dynamic viscosity. The density ρ and viscosity η can be combined into the kinematic viscosity ν, and Re becomes

$$Re = \frac{vl}{\nu}. \tag{6.3}$$

To understand the difference between the world of the cilium and the world in which we live, we can compare the Reynolds number for cilia to the Reynolds number for our everyday environment. To illustrate, let l be height, 2 m, and if we walk across the room at $\sim v = 2$ m/s in air ($\rho = 1.18$ kg/m^3 and $\eta = 1.78 \times 10^{-2}$ cP), the Reynolds number is approximately 270,000. This Reynolds number is considered high, in a turbulent regime of flow characterized by eddies and vortices. Turbulent flow typically begins at a Reynolds number greater than 1000. For aqueous solutions, on average, $\rho = 1000$ kg/m^3 and $\eta = 1$ cP, which is equivalently $Re = vl/10^{-6}\ m^2/s$. To live in a low Reynolds number environment, in a laminar flow regime, $vl \leq 10^{-3}\ m^2/s$. For both biological and biomimetic cilia, the relevant length and velocity (at a beat frequency of 10 Hz) scales are listed in Table 6.1, and the Re are on the order of 10^{-3}, solidly within the laminar flow regime.

Table 6.1: Characteristic scales of biological and biomimetic cilia

	Length (μm)	Diameter (nm)	Tip velocity (μm/s)	Re
Biological cilia	7	250	~200 (Hill et al., 2010)	~1.4x10^{-3}
Biomimetic cilia	10 or 25	550-800	~220	~2.2x10^{-3}

An illustration of turbulent and laminar flow can be seen flowing from a kitchen sink faucet. When the water pours from the faucet at a low flow speed (velocity), the fluid appears to move smoothly and steadily; this flow is laminar. Greatly increase the velocity of the fluid by allowing more water to exit the faucet, and the motion of the water undergoes a distinct change. No longer is the flow steady and smooth, but instead, the water tends to flow in every direction. The paths of fluid parcels cross over one another, intermingle, and are impossible to predict; this is turbulent flow.

In laminar flow, fluid parcels moving side by side will never cross paths or mix with one another. The only mixing which occurs in laminar flow is through diffusion. Nearly all microfluidics channels are at low Reynolds number for aqueous solutions. Mixing two fluids in a microfluidic or lab on a chip device more quickly than occurs through diffusion is impractical without some additional construct which forces the interaction of fluid parcels with one another. Because of this, many mixing devices, including several artificial cilia discussed in Section 3.1, have been developed to fulfill this technological need. In Section 6.2.3, I will address how our biomimetic cilia system may be one avenue of addressing the need for mixers in microfluidics.

Deborah Number

For viscoelastic fluids, one important characteristic is the timescale over which they flow. The response to an applied strain for purely viscous fluids is independent of time − upon the achievement of a constant strain, the Newtonian fluid relaxes nearly instantly. Applying a constant strain rate to a viscoelastic fluid evokes a gradual relaxation of stress to zero over a prolonged time (Macosko, 1994). The relaxation time is essentially the time it takes the material to adjust to any changes in the applied stress or strain. Because of the time dependent nature of the relaxation phenomena for a viscoelastic fluid, carefully selecting a time over which to observe the viscoelastic fluid is critical. The Deborah number, De, is the ratio of a material's relaxation time λ to the experiment's observation time t (Macosko, 1994):

$$De = \frac{\lambda}{t}. \tag{6.4}$$

For $De << 1$, the relaxation time is small compared to the observation time, and the material behaves like a liquid. Purely viscous liquids have Deborah numbers much less than one as their relaxation times are very short. For $De >> 1$, the material behaves like a solid, as the material never fully relaxes within the observation time. A material with a Deborah number which is of the order 1 is viscoelastic, exhibiting both viscous, liquid-like characteristics and elastic, solid-like characteristics (Macosko, 1994).

In order for biological cilia to be efficient in propelling fluid, the Deborah number for the fluid must be $De \leq 1$. If $De > 1$, the fluid will behave like a solid, and as De increases,

cilia will become responsible for the propulsion of a solid-like material. If we consider the observation time, or flow time, for cilia to be the beat frequency the solid-like fluid is incapable of responding on a comparable time-scale, and the combined cilia-fluid system may not be efficient. This concept was investigated in 2010 with a computational model of a free undulating sheet swimming in a viscoelastic fluid. Teran et al. found that the swimmer moved more quickly and efficiently when its beat frequency was on the same order as the fluid's relaxation time. When compared to a finite-length swimming sheet in a purely viscous fluid where $De << 1$, the swimmer with $De \sim 1$ moved a distance 25% farther in the same length of time (Teran et al., 2010).

Weissenberg Number

A viscoelastic fluid comprises both viscous and elastic contributions from the polymers within the fluid. Similar to the Deborah number, the Weissenberg number We indicates whether the material is slightly or largely viscoelastic, as it is the ratio of elastic to viscous forces. We is defined as (Metzner et al., 1966)

$$We = \frac{\lambda v}{l} \tag{6.5}$$

where λ is the zero-shear-rate relaxation time, v is the velocity of the fluid, and l is the characteristic length scale of the system. A fluid with a longer relaxation time will be more elastic, as purely viscous Newtonian fluids relax nearly instantly under a constant applied stress. Thus, a larger We will correspond to a more elastic fluid. In a typical experiment considering flow past a cylinder, l represents the diameter of the cylinder (Liu et al., 1998).

For a biological or biomimetic core-shell cilium, this is approximately 250−550 μm, further increasing the contribution of the elastic component of the fluid.

6.1.2 Navier-Stokes equation

In continuum fluid mechanics, the governing equations are the conservation of mass equation (also known as the continuity equation) and the conservation of momentum equation (essentially $\vec{F} = m\vec{a}$ for fluid elements). The conservation of mass equation states that the rate of change in density within a volume element must equal the rate of mass transported into the same volume element across a surface. This relationship is also known as the continuity equation because it implies a constant flow velocity field. Quantitatively, the conservation of mass equation states

$$\frac{\partial \rho}{\partial t} = -\nabla \cdot (\rho \vec{u}). \tag{6.6}$$

where ρ is the fluid density, t is time, and u is the velocity of the fluid element. Unless the flow velocity is approaching the speed of sound, the fluid is typically considered incompressible and has a constant density. With this assumption, Equation 6.6 becomes

$$\nabla \cdot \vec{u} = 0, \tag{6.7}$$

also known as the incompressibility constraint.

The equation for conservation of momentum is written as Newton's second law for fluids. Surface forces exerted on a fluid are equal and opposite the rate of momentum

transported by the flow across the surface, or (Goodwin and Hughes, 2008)

$$\frac{\partial(\rho\vec{u})}{\partial t} + \nabla \cdot (\rho\vec{u}\vec{u}) = \nabla \cdot \Pi + \rho\vec{f}. \tag{6.8}$$

This equation is actually three equations as it represents momentum in all three directions, and these three equations combined with the continuity equation represent the Navier-Stokes equations. In Equation 6.8, the surface forces can be divided into two categories: forces exerted onto the entire surface externally (such as gravity) and forces exerted inside the surface by the fluid parcels (such as viscous stresses). The first term on the left side of Equation 6.8 represents the rate of momentum increase; the second term to the left of the equal sign is the rate of momentum transported across a surface by flow. On the right side of the equation, the first term encompasses all surface forces exerted by the fluid, and the latter term is all external forces exerted on the body of the fluid as a whole.

In Equation 6.8, Π is called the total Cauchy stress tensor (used for small deformations) and can be written as the sum of its diagonal and off diagonal elements,

$$\Pi = -p\delta + \tau \tag{6.9}$$

where p is the pressure, δ is the Kronecker delta, and τ is the viscous stress tensor. Taking the divergence of Equation 6.9 gives

$$\nabla \cdot \Pi = -\nabla p + \nabla \cdot \tau \tag{6.10}$$

which can be substituted into the Navier-Stokes equation (Equation 6.8) to describe the

flow of any type of fluid, (Macosko, 1994)

$$\frac{\partial(\rho\vec{u})}{\partial t} + \nabla \cdot (\rho\vec{u}\vec{u}) = -\nabla p + \nabla \cdot \tau + \rho\vec{f}. \tag{6.11}$$

The equations thus far have remained general and are applicable to any fluid if the incompressibility constraint is not enforced. To determine the flow for a particular fluid, we need the fluid's stress-strain relationship, often represented by the viscous stress tensor τ, also called a constitutive relation. The constitutive relation will vary depending on the material. As an example, Table 6.2 lists a number of constitutive relations for both purely viscous and viscoelastic fluids (Macosko, 1994). The double underline indicates a tensor.

Table 6.2: Viscous stress tensors (Macosko, 1994)

Model name	**Function**
Generalized Newtonian	$\underline{\underline{\tau}} = -\eta(\dot{\gamma})\underline{\underline{\dot{\gamma}}}$
Generalized linear viscoelastic (Lodge model)	$\underline{\underline{\tau}} = -\int_{-\infty}^{t} G(t-t')\underline{\underline{\dot{\gamma}}}(t')dt'$
Maxwell	$\underline{\underline{\tau}} + \lambda\frac{\partial\underline{\underline{\tau}}}{\partial t} = -\eta_0\underline{\underline{\dot{\gamma}}}$
Upper convected Maxwell	$\underline{\underline{\tau}} + \lambda\overset{\triangledown}{\underline{\underline{\tau}}} = -\eta_0\underline{\underline{\dot{\gamma}}}$
Lower convected Maxwell	$\underline{\underline{\tau}} + \lambda\overset{\triangle}{\underline{\underline{\tau}}} = -\eta_0\underline{\underline{\dot{\gamma}}}$
Oldroyd B fluid	$\underline{\underline{\tau}} + \lambda_1\overset{\triangledown}{\underline{\underline{\tau}}} = -\eta_0(\underline{\underline{\dot{\gamma}}} + \lambda_2\overset{\triangledown}{\underline{\underline{\dot{\gamma}}}})$

In Table 6.2, η is the fluid viscosity, η_0 is the steady state fluid viscosity, λ is the material's relaxation time, $\dot{\gamma}$ is the shear rate, and the upper and lower convected derivatives are defined as (Macosko, 1994)

$$\overset{\triangledown}{\underline{\underline{\tau}}} = \frac{\partial \underline{\underline{\tau}}}{\partial t} + \underline{u} \cdot \nabla \underline{\underline{\tau}} - (\nabla \underline{u})^T \cdot \underline{\underline{\tau}} - \underline{\underline{\tau}} \cdot \nabla \underline{u} \tag{6.12}$$

$$\overset{\triangle}{\underline{\underline{\tau}}} = \frac{\partial \underline{\underline{\tau}}}{\partial t} + \underline{u} \cdot \nabla \underline{\underline{\tau}} + \nabla \underline{u} \cdot \underline{\underline{\tau}} + \underline{\underline{\tau}} \cdot (\nabla \underline{u})^T. \tag{6.13}$$

I am interested in both viscous and viscoelastic fluids. Thus, the following two sections will discuss the pertinent viscous stress tensors for both types of fluids.

6.1.3 Navier-Stokes equation and purely viscous stresses

In applying the Navier-Stokes equation to purely viscous Newtonian fluids at low Reynolds number, several assumptions can be made. The first assumption is the incompressibility constraint; we have an incompressible fluid, $\nabla \cdot \vec{u} = 0$, and thus the second term in Equation 6.11 is equal to zero. The second assumption is an absence of external body forces acting on the fluid. (I am ignoring forces such as gravity.) Thus, in Equation 6.11, $\vec{f} = 0$. The third assumption is that of low Reynolds number, and the fourth is the presence of a steady flow. This fourth assumption implies that the velocity does not change as a function of time, $\partial(\vec{u})/\partial t = 0$, and the first term in Equation 6.11 is equal to zero. After all of these assumptions, the Navier-Stokes equation becomes

$$\nabla p = \nabla \cdot \tau. \tag{6.14}$$

We can now include the stress tensor τ for a purely viscous fluid. Purely viscous fluids obey Newton's Law of Viscosity, which puts forth a linear relationship between stress and strain rate with a proportionality constant equal to the fluid's viscosity. Mathematically,

(Macosko, 1994)

$$\tau = \eta\dot{\gamma} = \eta[\nabla u + (\nabla u)^T] \tag{6.15}$$

where η is the dynamic fluid viscosity and u is the fluid velocity, and because of the incompressibility constraint,

$$\nabla p = \eta\nabla^2 u. \tag{6.16}$$

The solution for the fluid velocity u in this equation is now dependent on the applied boundary conditions.

Poiseuille and Couette Flow

Two independent analytical solutions to this low Reynolds number Navier-Stokes equation for Newtonian fluids, called Poiseuille and Couette flow, are of immediate interest as they will be utilized to describe cilia-driven velocity u as a function of height z above the cilia array. In both Poiseuille and Couette flow, fluid is situated between two no-slip parallel plates that extend infinitely in the x and y directions. Poiseuille flow is driven by a nonzero pressure gradient which results in a parabolic velocity profile (Figure 6.1), while in Couette flow, a constant velocity translation of one of the infinite plates drives a linear velocity profile.

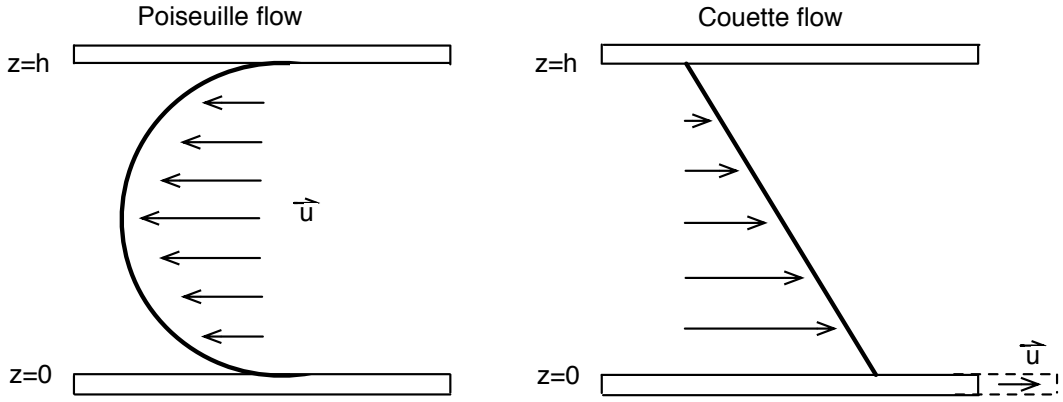

Figure 6.1: Schematics of both Poiseuille (at left) and Couette (at right) flow profiles. Poiseuille flow is a parabolic velocity profile with a nonzero pressure gradient between two stationary infinite plates. Couette flow is a linear velocity profile driven by a uniformly translating bottom plate with a stationary top plate as a second boundary.

Taking the linear superposition of these two independent solutions to Navier-Stokes produces a third solution which we call Poiseuille-Couette (PC) flow. More generally, this represents a limiting case of driven cavity flow where the cavity length and width are much larger than its height and a single boundary translates at constant velocity, driving vortical flow throughout the cavity (Bye, 1966; Albensoeder et al., 2001). The equation describing PC flow is given as

$$u(z) = \frac{u_0}{h}(h - z) + \frac{\nabla p}{2\eta} z(z - h) \tag{6.17}$$

where u_0 is the translating velocity of the bottom plate (located at $z = 0$) relative to the stationary top plate (located at $z = h$) (Shields et al., 2010) .

6.1.4 Stokes' 1st and 2nd problems

For both viscous and linear viscoelastic fluids, Stokes' first and second problems are benchmark problems in fluid mechanics and have many applications. They are both exact solutions to the Navier-Stokes equation but have different boundary conditions. In both problems, there is a semi-infinite space above a flat infinite plane. In Stokes' 1st problem, the system is initially at rest, and at time $t = 0$, the plane suddenly begins translating at a velocity $u = U$. In Stokes' 2nd problem, the infinite plane sinusoidally oscillates in time with a velocity $u = U_0 sin(\omega t)$ where ω is the frequency of the oscillation. For both problems, no pressure gradient exists, and as the motion of the infinite plate is only in the x direction, the fluid velocity is also only in the x direction and only a function of y. The Navier-Stokes equation (Equation 6.11) in the x direction reduces to the following for both Stokes' 1st and 2nd problems with a purely viscous fluid,

$$\frac{\partial u}{\partial t} = \nu \frac{\partial^2 u}{\partial y^2} \tag{6.18}$$

where u is the fluid velocity in the x direction, and ν is the kinematic viscosity η/ρ. For Stokes' 1st problem, the boundary conditions are

$$u(0,t) = \begin{cases} 0 & t \leq 0, \\ U & t > 0 \end{cases} \tag{6.19}$$

and the condition that the fluid velocity remain finite as we move far away from the plane (as $y \to \infty$). The initial condition we apply is $u(0,0) = 0$, indicating the fluid is at rest at

time zero. As I am more interested in Stokes' 2nd problem with the sinusoidally oscillating plane, I will give the solution to Stokes' 1st problem:

$$u(y,t) = U\left(1 - \text{erf}\left(\frac{y}{2\sqrt{\nu t}}\right)\right) \tag{6.20}$$

where erf is the error function.

For Stokes' 2nd problem, the boundary condition of a finite velocity as $y \to \infty$ remains, and in addition,

$$u(0,t) = \begin{cases} 0 & t \leq 0. \\ U sin(\omega t) & t > 0 \end{cases} \tag{6.21}$$

The initial condition is still $u(0,0) = 0$. We can assume a solution of the form

$$u(y,t) = \Im\left[f(y)e^{i\omega t}\right] \tag{6.22}$$

where $\Im$ indicates the imaginary part of the solution and $f(y)$ is the amplitude of the oscillation as a function of the distance from the oscillating plane. Substituting this solution into Equation 6.18 gives

$$\Im\left[i\omega f(y)e^{i\omega t}\right] = \nu\Im\left[\frac{d^2 f(y)}{dy^2}e^{i\omega t}\right] \Longrightarrow \frac{d^2 f(y)}{dy^2} = \frac{i\omega}{\nu}f(y). \tag{6.23}$$

This second order homogeneous differential equation has a solution of the form

$$f(y) = c_1 e^{r_1 y} + c_2 e^{-r_2 y} \tag{6.24}$$

where c_1 and c_2 are constants determined using boundary and initial conditions, and r_1, and r_2 are roots of the characteristic equation. Immediately, we know f(y) must remain finite as $y \to \infty$, which does not happen for the first term. Thus $c_1 = 0$, and we are left with

$$f(y) = c_2 e^{-r_2 y} \tag{6.25}$$

where substitution into the original differential equation, Equation 6.23, gives

$$c_2 {r_2}^2 e^{-r_2 y} = \frac{i\omega}{\nu} c_2 e^{-r_2 y}. \tag{6.26}$$

From this, we can see that $r_2 = \sqrt{i\omega/\nu}$. The solution then becomes

$$f(y) = c_2 e^{-\sqrt{i\omega/\nu}\, y}, \tag{6.27}$$

and inserting this back into the original solution, Equation 6.22, gives

$$u(y,t) = \Im\left[c_2 e^{-\sqrt{i\omega/\nu}\, y} e^{i\omega t}\right]. \tag{6.28}$$

Before taking the imaginary part of this solution, I will substitute $\sqrt{i} = (1+i)/\sqrt{2}$ into the above equation. Making this substitution and taking the imaginary part using Euler's relation $e^{i\theta} = cos\theta + isin\theta$ gives

$$u(y,t) = c_2 e^{-\sqrt{\frac{\omega}{2\nu}}\, y} sin\left(\omega t - \sqrt{\frac{\omega}{2\nu}}\, y\right). \tag{6.29}$$

We can use the final set of boundary conditions on the velocity where $u(0,t) = Usin(\omega t)$, implying that $c_2 = U$. The solution to Stokes' 2nd problem for a viscous fluid then becomes

$$u(y,t) = Ue^{-\sqrt{\frac{\omega}{2\nu}}\,y} sin\left(\omega t - \sqrt{\frac{\omega}{2\nu}}\,y\right), \tag{6.30}$$

a solution which describes an oscillating velocity, maximally valued at the location of the oscillating boundary and decaying as a function of distance y from the boundary.

It is interesting to understand from Equation 6.30 the length scale associated with the penetration of the motion of the lower boundary into the fluid. This length scale is called the penetration depth and is defined as the height y above the oscillating plate where the velocity is equal to $1/e$ its original value. Since the value of sine in Equation 6.30 has a maximum value of one, we can write

$$\frac{1}{e}U = Ue^{-\sqrt{\frac{\omega}{2\nu}}\,\alpha} \tag{6.31}$$

where α is the penetration depth. After some algebra, we have

$$\alpha = \sqrt{\frac{2\nu}{\omega}}, \tag{6.32}$$

illustrating that as the viscosity of the fluid above the oscillating boundary increases, the penetration depth increases, and the effects of the boundary are felt farther into the fluid. This result is depicted in Figure 6.2 with a boundary located at $y = 0$ oscillating at $\omega = 1$ Hz. Each plot represents a different kinematic viscosity ($\nu = 1, 2, 4$). In an individual plot, a single line represents a moment in time where the center of the plane is moving with

a velocity equal to the x-intercept. As the plane oscillates, the color of the lines changes from red to green to blue. As the viscosity increases, the coupling between the boundary and the fluid increases as can be seen by the increased penetration depth and the lack of a sharp decrease in velocity with increased height. Conversely, though it is not illustrated in the figure, as the oscillating frequency of the boundary increases, the penetration depth decreases.

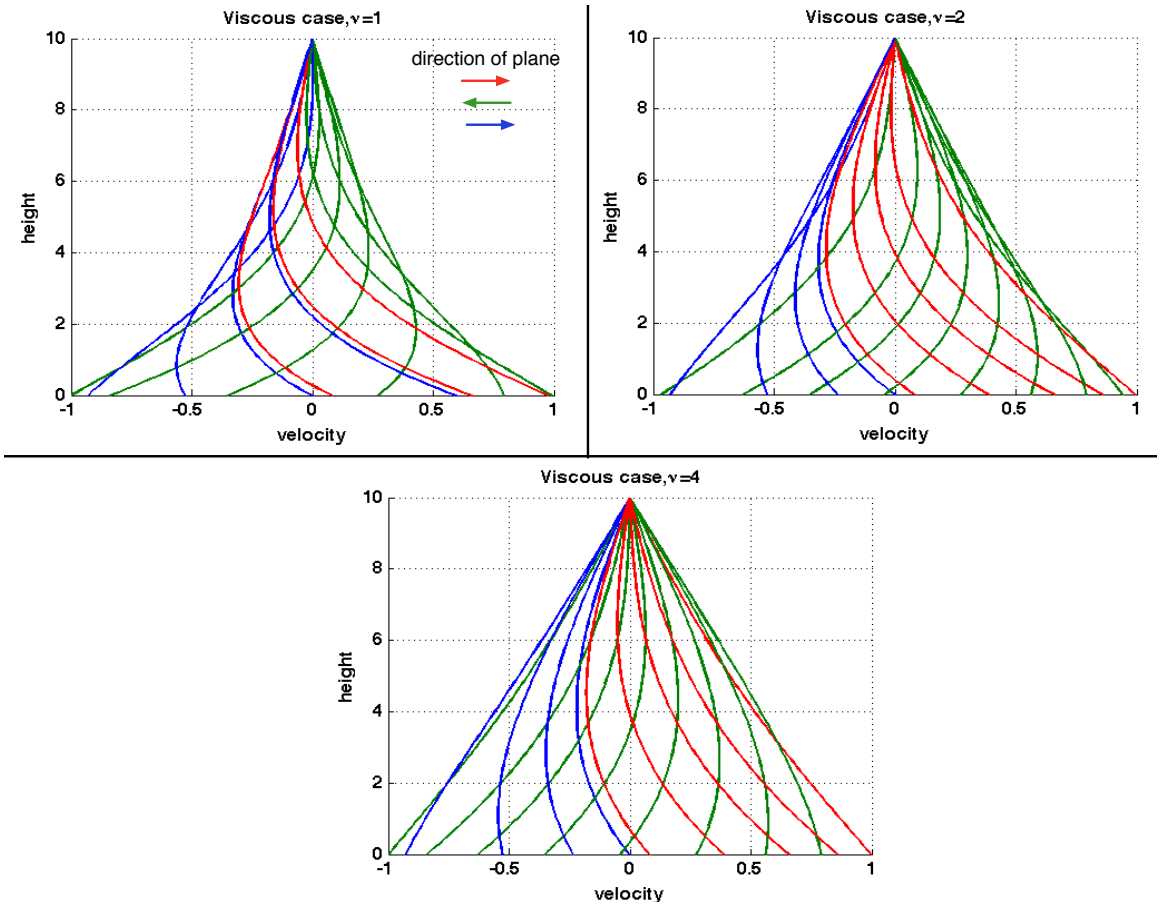

Figure 6.2: A simulation of Stokes' 2nd problem for a purely viscous fluid illustrates the effects of an increasing viscosity on the propagation of stress throughout the fluid. Each plot represents a different viscosity ($\nu = 1, 2, 4$), and within a plot, a line indicates an instant in time after a steady state has been reached. Red lines correspond to earlier times and blue lines correspond to later times. The frequency of the oscillating plane is $\omega = 1$ Hz. As the viscosity increases, the effect of the oscillating plane penetrates farther into the fluid.

6.1.5 Modified Stokes' 2nd problem

The previous solution was only for the purely viscous fluid which follows Newton's Law of Viscosity. If we consider a fluid which obeys a different constitutive law, the equation of motion will differ as will the resulting solution for the velocity of the fluid. In addition, changing the boundary conditions for any fluid type will alter the solution to the differential equation. Adding a stationary upper boundary at $y = h$ is called the Modified Stokes' 2nd problem, and for the viscous fluid, the presence of the upper boundary means we cannot ignore the positive exponential term in Equation 6.24. Thus, for a plate oscillating at $u(y,t) = U sin(\omega t)$, we have a hyperbolic sine function, and the fluid velocity becomes (Mitran et al., 2009)

$$u(y,t) = \Im\left[U e^{i\omega t} \frac{sinh[\frac{\delta_0}{A}(h-y)]}{sinh[\frac{\delta_0}{A}h]}\right] \tag{6.33}$$

where $\Im$ refers to taking the imaginary part, $A = U/\omega$, and $\delta_0 = (1+i)\sqrt{\omega/(2\nu)}$. Each plot in figure 6.3 shows the flow profile for a given kinematic viscosities ($\nu = 1, 2,$ or 4). Each line within a plot is a moment in time after a steady state flow has been reached. As with Figure 6.2, red lines indicate the plane's passage to the right, green lines indicate the plane's passage to the left, and blue lines indicate the plane's passage to the right again. The penetration depth is related to the inverse of $\Re(\delta_0)$. When comparing the flow profiles of Stokes' 2nd problem and Modified Stokes' 2nd problem, the effects of the oscillating plane in Stokes' 2nd problem penetrate farther into the fluid as in Modified Stokes' 2nd problem, the fluid velocity must be zero at the upper boundary. Notice again the decrease

in velocity as a function of height for the lower viscosity fluid as compared to the higher viscosity fluid. The effects of the oscillating boundary penetrate farther into the fluid as ν increases.

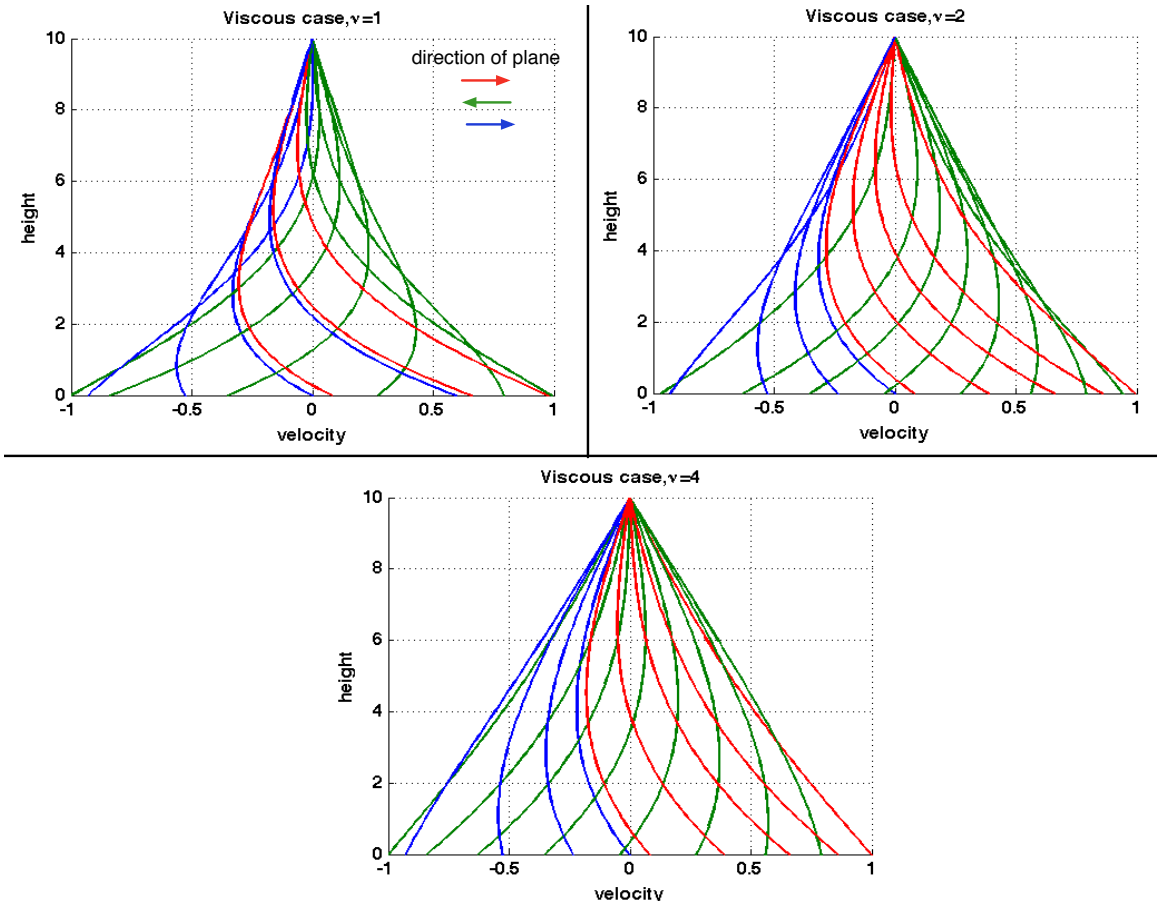

Figure 6.3: A simulation of Modified Stokes' 2nd problem for a purely viscous fluid illustrates the effects of an increasing viscosity on the propagation of stress throughout the fluid. The frequency is assumed to be $\omega = 1$ Hz. Each plot represents a different viscosity ($\nu = 1, 2, 4$), and within a plot, a line indicates a single time step after a steady state has been reached. Red lines correspond to earlier times and blue lines correspond to later times. The three plots demonstrate that as ν increases, the coupling between the fluid and the boundaries increases.

For viscoelastic fluids, the original differential equation for which I seek a solution will not include Newton's Law of viscosity, but will instead be a constitutive relation for the the viscous stress tensor τ which, depending on the fluid, may or may not lead to an analytical

solution of the Modified Stokes' 2nd problem. For two viscoelastic fluids, the linear viscoelastic Maxwell model and the nonlinear upper convected Maxwell and Giesekus models, modified Stokes' 2nd problem has been solved analytically. Both Maxwell models are listed in Table 6.2.

The Maxwell model was first proposed by Maxwell in 1867 in differential form for small changes in stress and strain (Macosko, 1994),

$$\underline{\underline{\tau}} + \lambda \frac{\partial \underline{\underline{\tau}}}{\partial t} = -\eta \underline{\underline{\dot{\gamma}}} \tag{6.34}$$

where η is the fluid viscosity, and λ is the material's relaxation time. This model actually falls out of the Generalized linear viscoelastic constitutive relation (in Table 6.2) if we assume only one single relaxation time within the fluid. Describing a fluid with a Generalized linear viscoelastic model implies a linear relationship between the change in stress ($d\tau$) and strain (γ) with a proportionality constant equal to the change in the relaxation modulus G, or $d\tau = dG\gamma$. These fluids do have memory as the generalized model integrates over all previous elapsed time. Graphically, Maxwell models are represented as a spring and dashpot combination, as shown in Figure 6.4, with the spring representing the elastic contribution and the dashpot representing the viscous contribution of the fluid. This concept that the application of slow stresses versus rapidly changing stresses affects a material's response ties into later discussion when I introduce the viscoelastic fluid agarose (Macosko, 1994).

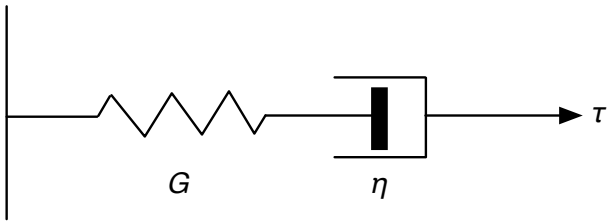

Figure 6.4: The spring and dashpot represent the linear Maxwell model with a single relaxation time. τ is the stress applied to the fluid.

It is much simpler to consider the Navier-Stokes equation in its non-dimensional form where the position variables in the equation have been divided by the appropriate characteristic length scale, the velocity has been divided by the characteristic velocity, and the time has been divided by the ratio of the length scale over the velocity scale. The non-dimensional Navier-Stokes equation is then

$$\frac{\partial u}{\partial t} + \nabla \cdot (\vec{u}\vec{u}) = \frac{1}{Re}\nabla \cdot (-p + \tau) \tag{6.35}$$

where Re is the Reynolds number. Assuming we still have no pressure gradient, a driving plane oscillation of $u(t) = Usin(\omega t)$ such that the fluid is only in the x direction, and the viscous stress represented by the Generalized linear constitutive relation (where I will include G specific to the Maxwell model), the non-dimensional Navier-Stokes equation becomes (Mitran et al., 2009)

$$\frac{\partial u}{\partial t} = \frac{1}{Re}\frac{\partial}{\partial y}\left[\int_{-\infty}^{t} G(t-t')\frac{\partial u(y,t')}{\partial y}dt'\right] \tag{6.36}$$

where η_0 is the zero-shear viscosity and for a Maxwell model, $G(t) = (\eta_p/\lambda)e^{-t/\lambda}$ with η_p non-dimensionalized by η_0 and λ non-dimensionalized by ω giving

$$\frac{\partial u}{\partial t} = \frac{\eta_p}{\lambda Re} \int_{-\infty}^{t} e^{-(t-t')/\lambda} \frac{\partial^2 u(y,t')}{\partial y^2} dt'. \tag{6.37}$$

This equation simplifies to a damped wave equation (Mitran et al., 2009),

$$\frac{\partial^2 u}{\partial t^2} + \frac{1}{\lambda}\frac{\partial u}{\partial t} = \frac{\eta_p}{\lambda Re}\frac{\partial^2 u}{\partial y^2}. \tag{6.38}$$

The solution to Equation 6.38 has a very similar appearance to the solution for a purely viscous fluid (Equation 6.33) and has been written down by Mitran et al. (2009) in its non-dimensionalized form:

$$u(y,t) = \Im\left[e^{it}\frac{sinh[\delta(H-y)]}{sinh(\delta H)}\right] \tag{6.39}$$

where $\delta = (1+i)\sqrt{Re/(2\eta^*)}$, in dimensional variables $Re = U^2/(\omega\nu)$, and t is measured in units of ω. The variable η^* is the complex viscosity of the fluid, and equal to $\eta' - i\eta''$ where η' is the viscosity and η'' is the elasticity of the fluid. Figure 6.5 illustrates Modified Stokes' 2nd problem for a viscoelastic fluid as a function of changing viscosity and elasticity. Three cases are shown in the figure: (i) $\eta' = 0.5\eta''$, (ii) $\eta' = \eta''$, (iii) $\eta' = 2\eta''$. For each case, a series of curves is displayed with each curve illustrating a moment in time after a steady state flow has been achieved.

Initially in the figure the elasticity of the fluid dominates the fluid's viscous response, and the coupling between the fluid and the boundaries is strong, as we see the effects of the oscillating plate continue to affect fluid elements near the upper boundary. In addition, it is interesting to note the increased velocity of the fluid is larger near the center of the

channel. This increase is likely due to the constructive interference of propagating and reflected shear waves (off the stationary upper boundary). This increased velocity is not present when the viscosity is on the same order or larger than the elasticity. In these cases ($\eta' \sim \eta''$ and $\eta' > \eta''$), the velocity profile begins to look more like a purely viscous fluid in that the effect of the oscillating boundary is damped by the viscosity of the fluid more quickly than in the first case where $\eta' = 0.5\eta''$.

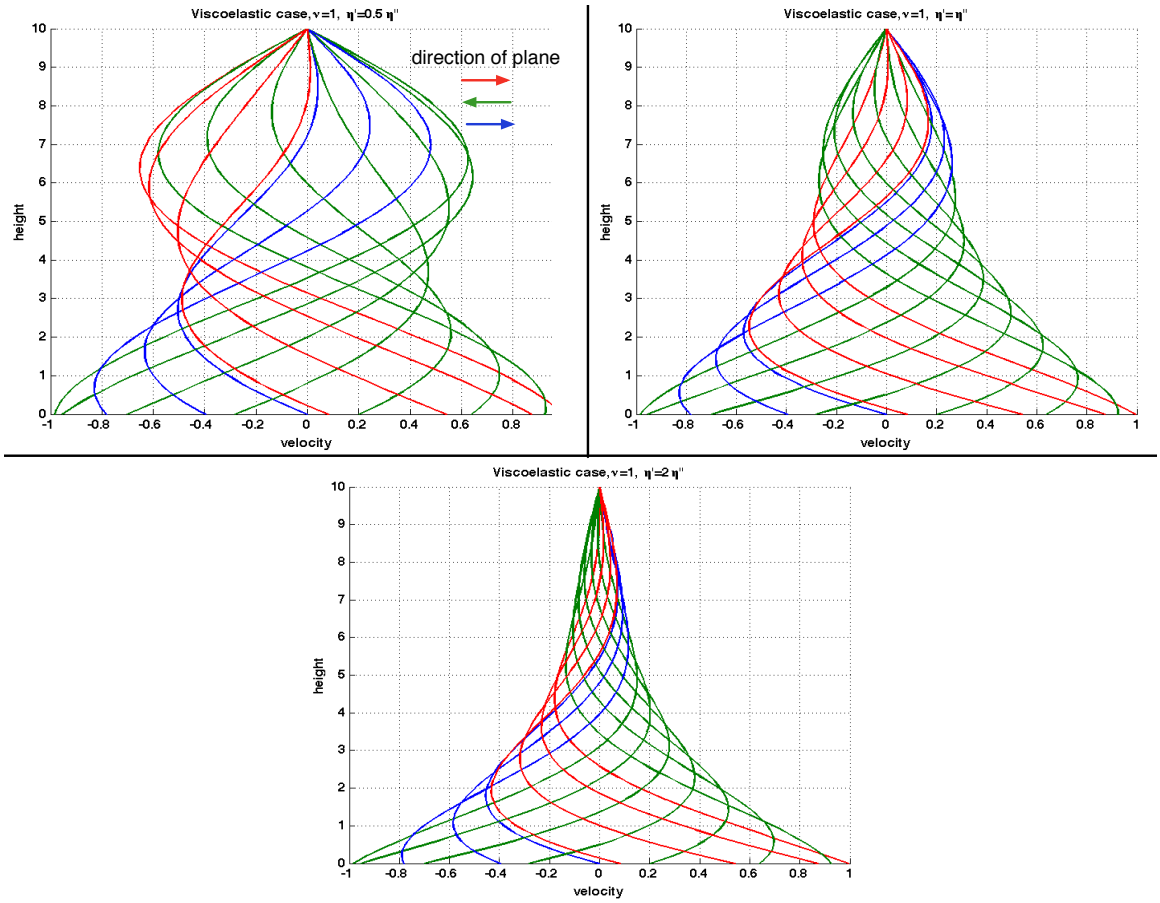

Figure 6.5: Flow velocity as a function of height in a viscoelastic fluid with kinematic viscosity $\nu = 1$ as obtained using the analytical solution to Modified Stokes' 2nd problem. Each plot illustrates a different relationship between the fluid's dynamic viscosity η' and its elasticity η''. Within a single plot, each curve represents a moment in time after steady state has been reached. Red lines indicate earlier times and blue lines correspond to later times. As viscosity η' increases with respect to the elasticity η'', the effect of the oscillating plane appears to die down more quickly; the velocity decays as height above the oscillating plane increases.

As I explore the flows produced by my biomimetic cilia in both viscous and viscoelastic fluids, these hydrodynamics solutions will be applied as a way to understand the underlying fluid dynamics in my systems, including the relationship among cilia beat frequency, flow velocity, and fluid viscosity and elasticity.

6.2 Fluid Transport in Aqueous Fluids

Both FFPDMS and core-shell cilia have produced driven transport in aqueous fluids utilizing the same tilted conical beat shape. To better understand how a single cilium contributes to the flow as a whole, I will present a hydrodynamic model which treats the motion of all cilia as a moving plane. This model is a superposition of two canonical solutions to the low Reynolds number Navier-Stokes equation and was first identified in our publication in 2010 (Shields et al., 2010) and later expounded upon in more detail by Adam Shields in his dissertation (Shields, 2010). The model is essentially that of a driven cavity (assuming a length and width much larger than height) and correlates well with both flow produced by our biomimetic cilia arrays and by biological vertebrate nodal embryonic cilia, allowing us to model both flows. An understanding of the low Reynolds number flow for purely viscous fluids also provides me with a first step in understanding more complex viscoelastic fluid flow; thus, the conclusions I present will be used in the following section (Section 6.3) to assist in the interpretation of viscoelastic cilia-driven flow.

In addition to looking at the flow driven by FFPDMS and core-shell cilia tips in this section, I will also discuss the flow below FFPDMS tips, which is drastically different from flow above cilia tips and characterized by large fluctuations in flow velocities from one spatial region to another. These large fluctuations in flow velocity and the lack of a uniform flow below cilia tips lends our biomimetic cilia to the application of mixing in microfluidics channels, which will be discussed in Section 6.2.3.

6.2.1 Flow velocity dependence on cilia beat frequency

Before discussing the flow profile (flow velocity as a function of height) in an aqueous fluid for a particular cilia beat frequency, it is important to understand how changing the beat frequency affects the flow velocity. The beat frequency is an easily controlled parameter in my artificial core-shell cilia system. By increasing the voltage supplied to the motor to which the permanent magnet is attached, the frequency of the motor may be increased, thereby increasing the cilia beat frequency. In addition, I control the flow direction by controlling the direction of the cilia beat; altering the rotational direction of the motor (clockwise to counterclockwise) changes the direction of the core-shell cilia beat.

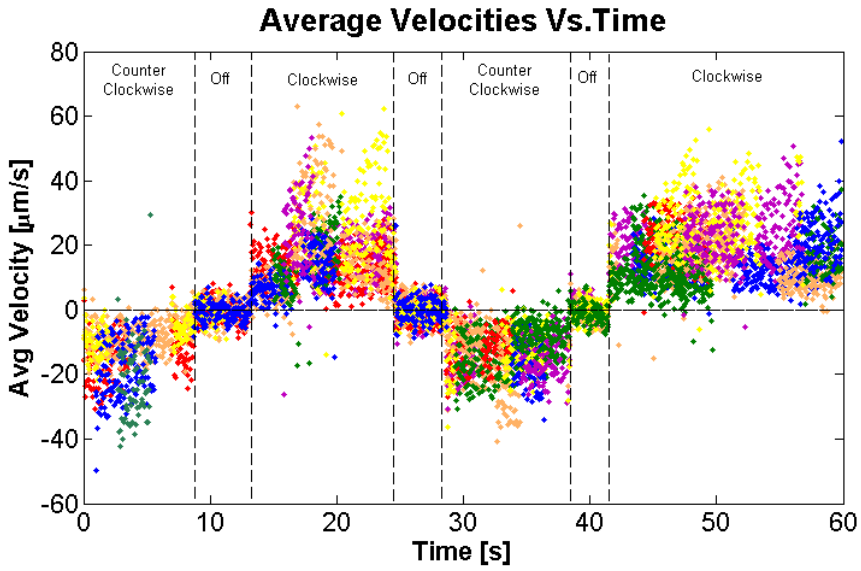

Figure 6.6: Flow direction as produced by core-shell biomimetic cilia can be altered by altering the direction of rotation of the driving motor and magnet. From time 0 to approximately 9.5 s, core-shell cilia are beating in the counterclockwise direction. From 9.5 s to 13 s, the magnet is stationary and cilia are no longer beating, and from 13 s to 24 s, core-shell cilia are beating in the clockwise direction, reflecting the change in the motor's rotational direction. Data was taken 10 μm above the cilia tips.

Figure 6.6 displays the velocity as a function of time where the direction of the driving force, created by the rotating motor plus magnet, is at first counterclockwise, removed from the array, rotated in the clockwise direction, removed from the array, and so on.

As the frequency of the driving force increases, so does the flow velocity driven by the core-shell cilia array in a purely viscous fluid. Figure 6.7 displays this linear relationship for core-shell biomimetic cilia. This positive linear velocity dependence on frequency is also seen with FFPDMS biomimetic cilia up to frequencies of at least 32 Hz. The effect of changing frequency on flow velocity in a viscoelastic fluid does not appear linear and will be discussed in Section 6.3.2. In addition, altering the tilt angle of the array affects flow velocity, though regardless of tilt angle, the relationship between frequency and flow velocity remains linear. A larger tilt angle increases the resulting flow velocity driven by the array. (Shields, 2010)

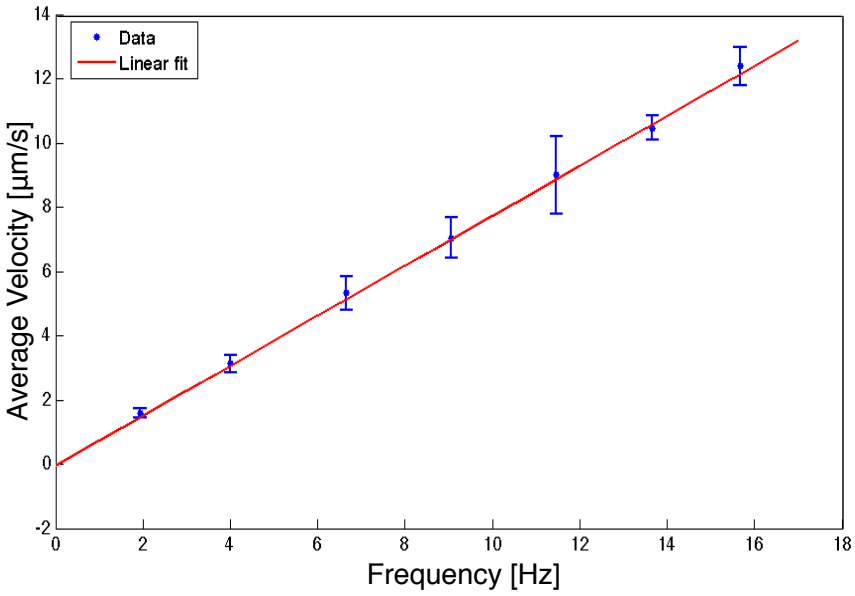

Figure 6.7: Flow velocity as a function of frequency 20 μm above the core-shell cilia tips in an aqueous phosphate buffered saline (PBS) solution. Flow velocity and frequency are linearly related, as indicated by the least squares linear fit.

In biology, we do have evidence that increased flow velocities are in some way related to increases in beat frequency. In 2005, Okada et al. published a study on the embryonic nodal cilia for three different species: mouse, medakafish, and rabbit. The study found that the cilia of each species beat at different frequencies, producing varying flow velocities in the purely viscous environment of the node. For the mouse, cilia beat at 10.7±2.8 Hz; for the medakafish, cilia beat at 42.7±2.6 Hz; and for the rabbit, cilia beat at 7.2±2.3 Hz. The leftward driven flow velocities for each species was correspondingly different, ranging from 1.3±0.4 μm/s for rabbits to 7.4±3.6 μm/s for medakafish (Okada et al., 2005). This relationship between frequency and velocity is not exactly linear, but note that the data represents three different species with various cilia sizes. The experiment to alter the beat frequency of cilia and understand resulting flow velocities in the node of a single embryo has not yet been realized.

6.2.2 Two regimes of flow

To evaluate the flow produced by biomimetic cilia in an aqueous Newtonian fluid, PBS seeded with 500 nm diameter fluorescent microspheres at a concentration of 1:300 was added to arrays mimicking the tilted conical beat of embryonic nodal cilia. This experiment has been performed with both 25 μm tall FFPDMS cilia (Shields et al., 2010) and 10 μm tall core-shell cilia (Fiser et al., 2012). However, two distinct regimes of flow have been studied only for the taller FFPDMS cilia arrays. Because of their height, these taller arrays show a distinct separation between the directed flow occurring above the cilia tips and the lack of directed flow below the cilia tips. Several fluorescent tracer particles below the

tips of shorter cilia arrays have been seen to exhibit large fluctuations in speed and rapid movements, jumping from the vortex created by one cilium to another, but for the most part, directional flow dominates, and most tracer particles travel at the same rate and in the same direction as the flow above the cilia tips.

These two regimes of flow present in 25 μm tall FFPDMS biomimetic cilia arrays are distinctive in nature, with a very sharp transition between them. As I mentioned previously, above the cilia tips, the flow is uniform and directed across the entire array, which is approximately 2 mm x 2 mm in size. This directed flow is fastest at the cilia tips and decreases as the distance above the cilia tips increases. At some point above the cilia tips, the flow begins to reverse itself and recirculate throughout the enclosed flow cell. Almost immediately below the cilia tips, the flow becomes nondirectional and appears rapid. Tracer particles jump from one cilia-induced vortex to another, sampling the flows around multiple cilia. The flow regime below cilia tips strongly resembles an enhanced diffusive process. Figure 6.8 illustrates the two regimes of flow. In the next two sections, I discuss the characterization of these regimes in further detail, the directed transport present in both FFPDMS and core-shell cilia arrays and enhanced diffusion in FFPDMS cilia arrays.

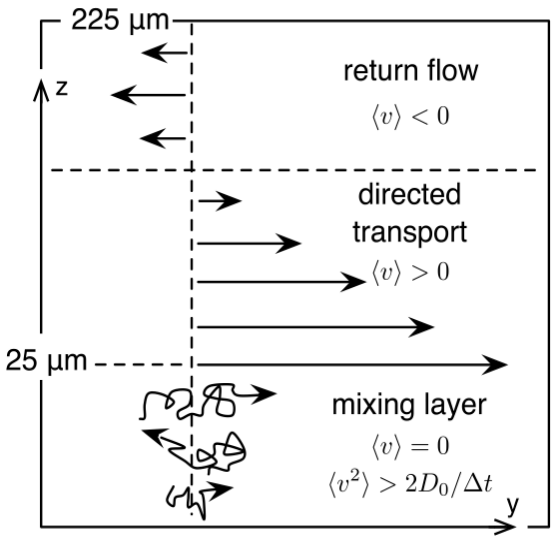

Figure 6.8: Reprinted from Shields et al. (2010). Biomimetic cilia driven flow in aqueous fluids exhibits different behavior above and below the cilia tips. Below the cilia tips, flow is rapid and nondirectional. Directly above the cilia tips, the flow is strongly directional and uniform across the entire array. As the height above the cilia array increases, the flow begins to reverse direction due to the enclosed nature of the fluidic cell in which the cilia sit (Shields et al., 2010).

Directed transport and the flow profile

Above the cilia tips, the flow is uniform, and strongly directional with tracer particles traveling the fastest directly at the cilia tips. The direction of the cilium beat when it is furthest from the floor determines the flow direction above the cilia tips. In order to develop a model of cilia-generated fluid flow, it is essential to understand how a single cilium contributes to the bulk fluid flow, also known as coarse-graining. Constructing a flow profile is key to understanding the motion of the bulk fluid. The flow profile, or velocity as a function of height, was generated by averaging the velocities of tracer particles in each individual focal plane within the fluidic cell (both above and below the cilia tips). Figure 6.9 shows the flow profiles for both FFPDMS and core-shell cilia arrays beating at

a frequency of 34 and 16 Hz, respectively. Both profiles are markedly similar in shape, though velocity and height values are different.

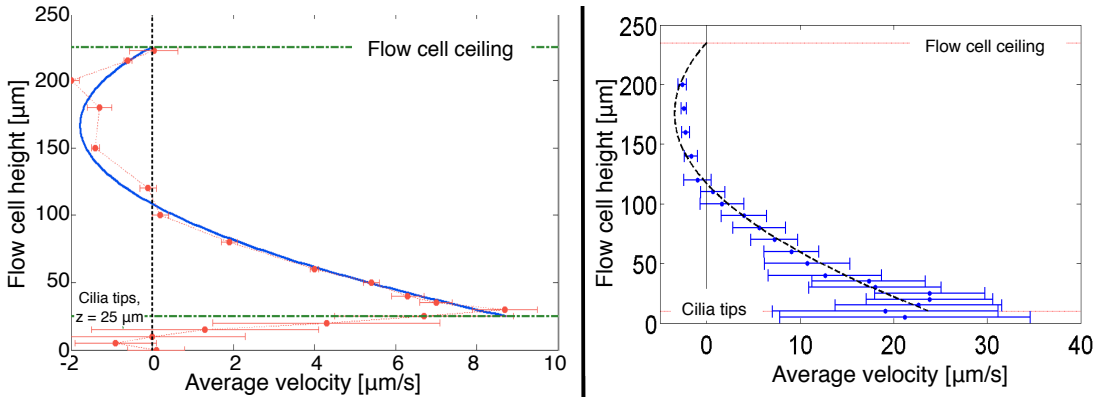

Figure 6.9: The flow profile at left is for FFPDMS biomimetic cilia, and the profile at right is for core-shell cilia. The flow velocity is largest at the cilia tips, with the core-shell cilia driving a larger velocity (~24 m/s) than FFPDMS cilia (~9 m/s) for beat frequencies 16 and 34 Hz, respectively. Around a height of $z = 100$ μm, the flow begins to recirculate in both cilia arrays. Below cilia tips, the distribution of velocities is much larger due to the nondirectional flow and large variations in velocity from tracer to tracer. As indicated by the solid (FFPDMS cilia) and dashed (core-shell cilia) lines in both flow profiles, the PC model accurately represents the flow above cilia tips. For FFPDMS cilia, $u_0 = 8.7$ μm/s and $\nabla p = 1.05$ Pa/m. For core-shell cilia, $u_0 = 24$ μm/s and $\nabla p = 2.0$ Pa/m

Looking at the flow velocities at and above the cilia tips ($z = 25 \rightarrow 225$ μm for FFPDMS cilia and $z = 10 \rightarrow 235$ μm for core-shell cilia), we can characterize the flow as a linear superposition of Poiseuille and Couette flow (PC flow), two classical solutions to the low Reynolds number, incompressible Navier-Stokes equation for Newtonian fluids (Equation 6.16. To apply PC flow to biomimetic cilia within a fluidic cell, I set $z' = z - 25$ μm for FFPDMS cilia and $z' = z - 10$ μm for core-shell cilia. For both FFPDMS and core-shell cilia, the cilia tips represent the lower plate at $z' = 0$ translating with a constant velocity u_0, and the stationary upper plate is located at $z' = 200$ μm and $z' = 225$ μm for the two cilia arrays, respectively. The solid blue line on the left plot in Figure 6.9 and the dashed

black line on the right plot are least squares fits of Equation 6.17 to the flow profiles. Fit parameters include the pressure gradient ∇p and the velocity of the translating plate u_0. From these fits, we conclude that our biomimetic cilia tips collectively generate a shear stress on the fluid, effectively acting as a moving plate. Additionally, the flow appears to have an effective pressure gradient driving recirculation within the fluidic cell. For a viscoelastic fluid with an elasticity comparable to viscosity, the flow velocity may not appear to decay as nicely as Figure 6.9 represents for a purely viscous fluid. The effects of a longer relaxation time and shear wave reflection off the upper boundary may create an nonlinear change in velocity as a function of height. All of these potential changes to the flow profile with the incorporation of a viscoelastic fluid will be discussed in Section 6.3.3.

In addition to describing our biomimetic cilia systems with PC flow, in Shields et al. (2010), we apply this PC flow fit to velocity data taken in a mouse embryonic node by Okada et al. (Okada et al., 2005), as shown in Figure 6.10. The cilia tips and node ceiling are indicated in the figure, information we gleaned from their work. From this fit and from Figure 6.9, we conclude that both our fabricated biomimetic cilia and biological nodal cilia behave as shear stress generating boundary for the fluid above the cilia tips.

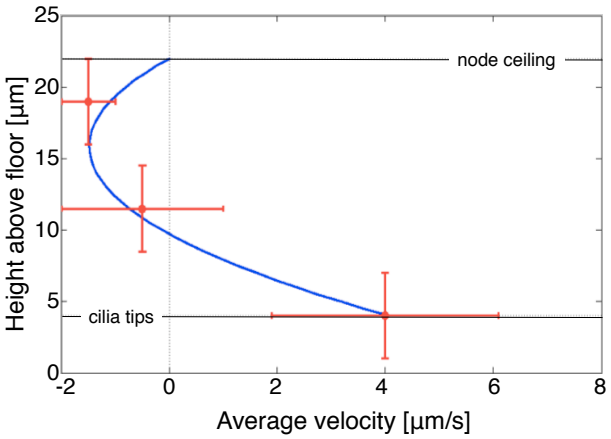

Figure 6.10: PC flow profile fit to mouse nodal flow velocity data obtained from Okada et al. (2005) at three different heights (Okada et al., 2005). Fit parameters are $u_0 = 4$ μm/s and $\nabla p = 79$ Pa/m.

Enhanced diffusion with FFPDMS cilia

Below the cilia tips, the flow appears rapid and nondirectional, and tracers exhibit large fluctuations in speed. Each cilium is associated with a local vortex, and tracers appear to jump from one vortex to the next, sampling the flows around multiple FFPDMS cilia. To understand more about this nonuniform flow below the tips, we need to understand how the velocities of tracer particles throughout the flow scale with time. The position r of a particle undergoing a constant velocity v, which is also called ballistic motion, scales linearly with time at the rate of the constant velocity, or $r = vt$. If the motion is not ballistic, the relationship between a particle's position at a time t will not be linear. To understand the relationship between position and time more generally, we use the mean square displacement (MSD), which defines a characteristic length scale over which a particle moves,

$$\langle r^2(\tau) \rangle = \alpha \tau^{\gamma} \tag{6.40}$$

where τ is a lag time, or time window, rather than an absolute time. For ballistic motion, Equation 6.40 reduces to $\alpha = v^2$ and $\gamma = 2$. For diffusive motion, motion which varies in time like a random walk, $\alpha = 2dD$ and $\gamma = 1$ where d is the Euclidean dimension ($d = 2$ for two dimensions) and D is the diffusion coefficient, or diffusivity. Processes which are not considered ballistic or diffusive are either superdiffusive ($1 < \gamma < 2$) or subdiffusive ($\gamma < 1$).

When determining the type of process exhibited by particles in a fluid, it is often simpler to look at the MSD in log-log space. Equation 6.40 becomes

$$log\left(\langle r^2(\tau)\rangle\right) = log(\alpha) + \gamma log(\tau) \tag{6.41}$$

such that when plotted, the slope of the curve is equal to γ and the y-intercept is equal to α, or for diffusive motion, $\gamma = 1$ and $\alpha = 2dD$.

Before looking at the motion of tracer particles below the cilia tips, the advective component of the flow was removed. This removal was done by analyzing the relative dispersion of pairs of tracers, with a separation of $\vec{R}(t) = \vec{x}_2(t) - \vec{x}_1(t)$ (Babiano et al., 1990; Artale et al., 1997; LaCasce and Bower, 2000). This relative dispersion method treats the separation of particles as a single particle; thus, four tracer particles in a fluid become six effective particles using relative dispersion. As with the transport of particles themselves, the transport of particle separations can be characterized by the MSD for two dimensions,

$$\langle R^2(\tau)\rangle = 4D^R_{eff}\tau^\gamma \tag{6.42}$$

where τ is again a lag time, D^R_{eff} is an effective relative diffusivity, and γ is the time dependence exponent. Performing a linear least squares fit to $\log(\langle R^2(\tau)\rangle)$ versus $\log(\tau)$ returned $\gamma = 1$ at all heights above the sample floor, indicating that the motion is effectively a diffusive process with an enhanced transport rate given by D^R_{eff}. The expected relative diffusivity for 500 nm diameter microspheres in PBS with no cilia motion is $D^R_0 = 1.8\ \mu m^2/s$. As shown in Figure 6.11, biomimetic cilia motion drives a maximum relative diffusivity of 42 $\mu m^2/s$, an enhancement in D^R_{eff} of 25 compared to D^R_0. For more detail on the characterization of an effective diffusion process, see the dissertation of Adam Shields (Shields, 2010).

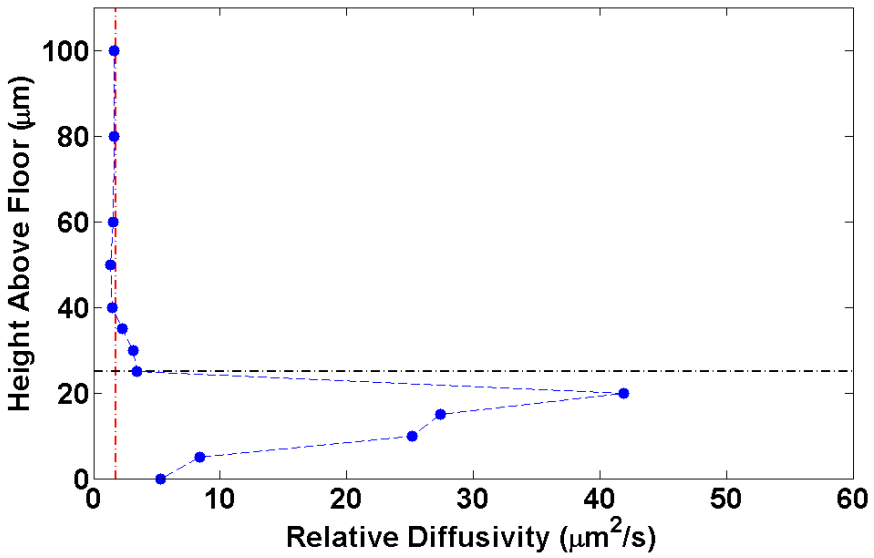

Figure 6.11: The cilia-driven motion of tracer particles below the cilia tips scales as a diffusive process with an enhanced transport rate of D^R_{eff}. The red line indicates the expected relative diffusivity of tracers in PBS without cilia present (Shields et al., 2010).

6.2.3 Implications for biology and technology

Our biomimetic cilia arrays are the first to truly mimic a biological system, and with it, we can inform our understanding of biological cilia. Biomimetic FFPDMS cilia-driven flow regimes were created by driving cilia in a tilted conical beat pattern, as described in Section 5.2.2, directly mimicking the tilted conical beat performed by vertebrate nodal embryonic cilia. Nodal embryonic cilia, in performing this beat, drive flow from the right to left sides of the embryonic node (Nonaka et al., 2002), and biomimetic cilia are capable of driving fluids in a similar fashion. I have shown that the flow profile established by nodal cilia above their tips correlates well with the flow profile established by biomimetic cilia above their tips (Section 6.2.2).

In addition to merely driving directional flow, there is a morphogen gradient generated within the nodal pit that plays a key role in determining left-right asymmetry in the vertebrate embryo (Nonaka et al., 2002). The morphogen gradient is more concentrated on the left side of the embryo, the same direction as the flow driven by nodal cilia. As I discussed in Chapter 2, within the node are nodal vesicular parcels (NVPs), one micron sized morphogen-loaded vesicles that carry their cargo toward the left side of the embryo and subsequently rupture, creating this morphogen gradient. The flow within the node must advect the NVPs efficiently to the left while transporting the released morphogens slowly enough to preserve the morphogen concentration gradient. Directed flow above the cilia tips appears to provide the initial establishment of a long-range chemical gradient; however, in order to form a gradient, NVPs must first reach the area where the directed flow regime dominates.

In 2005, Tanaka et al. proposed a mechanism for the release of NVPs into the advective flow layer such that microvilli at the cell surface dynamically extend NVPs into the flow (Tanaka et al., 2005). The directed flow results presented support this idea; some mechanism must be present to establish the initial morphogen gradient. Whether or not the gradient remains after initial transport into the advective layer depends on the competition between cilia-driven transport and the rate of intrinsic diffusive transport. The particle transport rate below the cilia tips is more rapid than the flow above, but it is nondirectional and effectively diffusive. Based on flow speed alone, it is unlikely that a chemical gradient would persist; however, cilia-driven mixing below the tips dominates intrinsic diffusivity for particle sizes larger than 10 nm. Thus, small molecules used to set up the chemical gradient within the node would not be affected by the enhanced mixing.

Besides being a tool for understanding biological cilia-driven flow, as a technological application, one use of microactuators such as ours has been as pumps or mixers in microfluidic systems. Microfluidics studies small volumes of fluids (typically microliter volumes) usually within sub-millimeter sized channels or systems of channels. Microfluidic systems deal almost exclusively with low Reynolds number laminar flows because of their small length scales, and in this environment, pumping without external syringe pumps and mixing are difficult. In laminar flow, the mixing of adjacent fluid particles is achieved only through diffusion, and thus is an inherently slow process. Many techniques exist in the literature which introduce physical constructs into the microfluidics channels, such as raised features on the sidewalls or floor, which interact with the fluid and cause fluid parcels to mix (Stroock et al., 2002). The time for a fluid to mix only through diffusion over a length

l in a fluid is

$$t_m = l^2 D. \tag{6.43}$$

Thus, a higher diffusivity D gives rise to a faster mixing time t_m, which for our biomimetic cilia may be 25 times faster. This enhanced diffusivity combined with the pumping action above the cilia tips make for a versatile device which can both mix and pump in two very spatially segregated regimes. In addition, one may alter the length of the biomimetic cilium, thereby changing the size of the mixing layer such that within a single microfluidics channel, one could span half the channel with a mixing regime and half the channel with a pumping regime, for selectively treating various fluids.

6.3 Fluid transport in viscoelastic fluids

All of our perceptions about motion and velocity are discarded in low Reynolds number environments where time is essentially irrelevant, and it is strictly the asymmetry of organism motion which determines whether an organism achieves net transport. In Section 6.2, I addressed this phenomenon in purely viscous fluids such as water and phosphate buffer. In this section, I will address the transport produced by biomimetic cilia in viscoelastic fluids. Adding an elastic component to the fluid further alters our understanding of phenomena at low Reynolds number, and this section will reach an understanding of these phenomena by first comparing them to the previously discussed viscous fluid case. The dependence of flow velocity on both cilia beat frequency and height in a viscoelastic fluid are important for

gaining a better understanding of biological cilia in the lung and the process of mucociliary clearance as a whole. There are many open questions concerning interactions between cilia and the mucus layer lining our lungs. The hurdle to answering these questions lies in part in the difficulty of obtaining *in vivo* samples of lung tissue. Much of our current understanding is derived from cell culture or animal models, both of which contribute greatly to our knowledge, but suffer from the drawback of being either a two-dimensional system or a system which is not entirely representative of the human airway. My biomimetic system is another model platform, one over which we have enormous control, that can also provide valuable contributions to our understanding of the interaction between cilia motion and the resulting viscoelastic fluid flow.

Before discussing results and implications, however, I take a moment to briefly review the nature of viscoelastic fluids and discuss the particular viscoelastic fluid, agarose, which is used in these flow experiments. Every fluid is, in the widest sense of the word, a viscoelastic fluid, consisting of both a viscous, or liquid, response, and an elastic, or solid response. Whether one characteristic or the other exhibits itself depends on the timescale t at which the material is probed (or over which the observation occurs) and the stress σ which is exerted on the material. As an example of a simple viscoelastic fluid, let us utilize the Maxwell model introduced in Section 6.1.5, which comprises a spring and dashpot in series representing the elastic and viscous contributions of a fluid's response, respectively. For the spring, the shear stress σ is proportional to the strain γ by the shear modulus G, and for the dashpot, the shear stress σ is proportional to the shear rate $\dot{\gamma}$ by the shear viscosity η. (Goodwin and Hughes, 2008) Suppose we quickly apply a small strain to a Maxwell

model fluid; the spring will respond immediately and the stress will remain constant over the entire application of strain. This stress will slowly dissipate, however, due to the dashpot piston's slow motion through its fluid. The stress decay as a function of time for the Maxwell fluid will be an exponential decay, $\sigma = \sigma_0 e^{-t/t_m}$ where t_m is a time constant associated with the fluid called the decay time. Dividing the stress equation by strain supplies us with a relaxation function, relating the modulus and decay time (Goodwin and Hughes, 2008):

$$\begin{aligned} G(t) &= \frac{\sigma}{\gamma} \\ &= \frac{\sigma_0}{\gamma} e^{-t/t_m}. \end{aligned} \tag{6.44}$$

When the observation time t is small compared to the decay time of the fluid, we can see that the exponential approaches one, and in the limit that $t \to 1$, $G(t) = G$, indicating that a Maxwell model fluid exhibits an elastic response at short time scales. As time passes, the stress is dissipated by the dashpot, which is indicative of a viscous response at long time scales. Short and long time scales correspond to high and low frequencies, respectively; thus the elastic response will display itself with high frequency interactions. Understanding the relationship between time and applied stress on material properties is integral to understanding the viscoelastic nature of a material.

6.3.1 The viscoelastic fluid agarose

As one of the motivations for my dissertation is to investigate the biological implications of our biomimetic system, I elected to understand biomimetic cilia-driven flow in the viscoelastic fluid agarose. Agarose is a polysaccharide derived from agar, which can be found in the cell walls of certain species of red algae. In the literature and in my own experiments, agarose has been shown to exhibit gross viscoelastic properties similar to those of bronchial epithelial mucus. In 1974, King et al., looked at the transport properties of multiple potential mucus mimics on cleaned frog palates. Transport was measured with 0.8 mm steel spheres. Agarose gels from 0.35-0.75% were tested and found to be transportable by the frog's depleted palate at approximately half the transport rate of native mucus (King et al., 1974).

In addition to King et al.'s measurements, I have measured the apparent viscosity as a function of shear rate for two concentrations of agarose, 0.1 and 0.25%, and compared these values to similar measurements obtained by Jeremy Cribb for two Human Bronchial Epithelial (HBE) mucus concentrations, 2.5 and 5.3% (Cribb, 2010). The two concentrations of HBE mucus were chosen because 2.5% corresponds to a 'normal' mucus sample, and 5.3% is considered similar to sputum obtained from a patient suffering with chronic obstructive pulmonary disease (COPD). Measurements were taken on a stress-controlled cone and plate rheometer (AR-G2, TA instruments) with a cone 40 mm in diameter at an angle of 1°. For agarose, a stress of 0.1 Pa was maintained and the frequency was varied between 10^{-2} and 10^{4} rad/s. The Cox-Merz rule, which equates the shear rate dependence of the steady state viscosity η and the frequency dependence of the linear viscoelastic vis-

cosity η^*, or essentially $\eta(\dot{\gamma}) = |\eta^*(\omega)|$, was applied to obtain viscosity as a function of shear rate (Macosko, 1994). In Figure 6.12, agarose data is included on the same plot as HBE mucus measurements for side-by-side comparison.

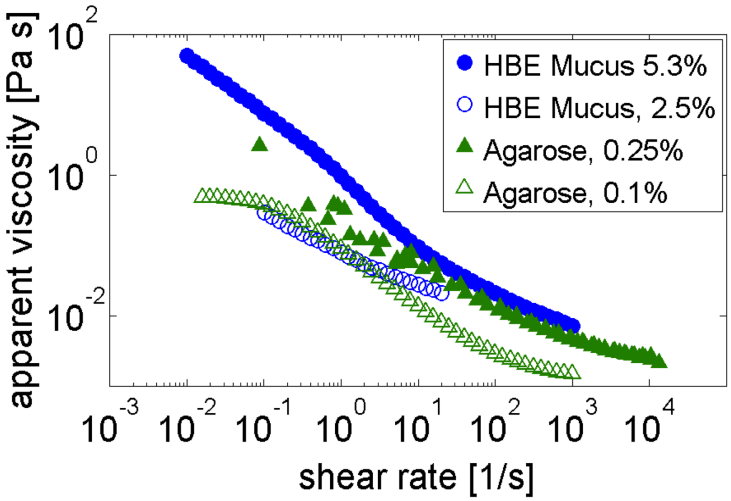

Figure 6.12: HBE mucus at concentrations of 2.5% and 5.2% (Cribb, 2010) and agarose at 0.1% and 0.25% exhibit similar gross viscoelastic properties.

Based on these comparisons, I use a concentration of 0.1% agarose to represent a healthy mucus and 0.25% agarose to represent a COPD-like mucus. Before adding these solutions to an array, I measured the viscous and elastic components of the fluid using the cone and plate rheometer. The application of a sinusoidally oscillating stress will produce a sinusoidal strain phase in the material shifted by the amount δ. This strain phase can further be divided into two waves with the same frequency; one wave is in phase with the strain, and the other is 90° out of phase with the strain. The in-phase wave is designated as the storage modulus, G', and the out-of-phase wave is designated as the loss modulus, G''. The storage modulus is a measure of the elastic component of a fluid, and the loss modulus is a measure of the energy dissipation of the fluid, representing the viscous component. We

relate the storage and loss moduli to the fluid's viscosity η' and elasticity η'' as $G' = \omega\eta''$, and $G'' = \omega\eta'$. A viscoelastic liquid has $G'' > G'$, and a viscoelastic solid has $G' > G''$. The loss tangent, or ratio of G'' to G', is frequently used to classify a viscoelastic material's behavior as liquid-like or solid-like. This loss tangent is written as (Macosko, 1994)

$$tan\ \delta = \frac{G''}{G'}. \tag{6.45}$$

Both of these moduli can be measured as a function of frequency and applied stress. Ideally, the measurement would be collected at a frequency and applied stress representative of the biomimetic cilia experiment, 16 Hz and at least 5 Pa (assuming a minimum cilia tip velocity of 50 μm/s). However, I am unable to explore the material's response at a frequency of 16 Hz as the material does not offer enough torque resistance to the motion of the cone, and the signal becomes extremely noisy and unreliable. This noisiness and signal unreliability occurs at frequencies as low as 10 Hz; thus, a frequency of 1 Hz was utilized to characterize agarose on the cone and plate rheometer. An applied stress of 0.01 Pa was also utilized as stresses larger than ~0.01 Pa explore the nonlinear regime of the material, a regime in which few assumptions can be made and little is understood about trends in the material response. Within the linear regime, G' and G'' are independent of the chosen stress amplitude and frequency. Figure 6.13 is a stress sweep at two different frequencies to illustrate the dependence of storage and loss moduli on frequency and stress outside the linear regime. The loss tangent, tan δ, for each data set in Figure 6.13, is shown in Figure 6.14. Recall that a loss tangent less than one implies the material exhibits solid-like behavior.

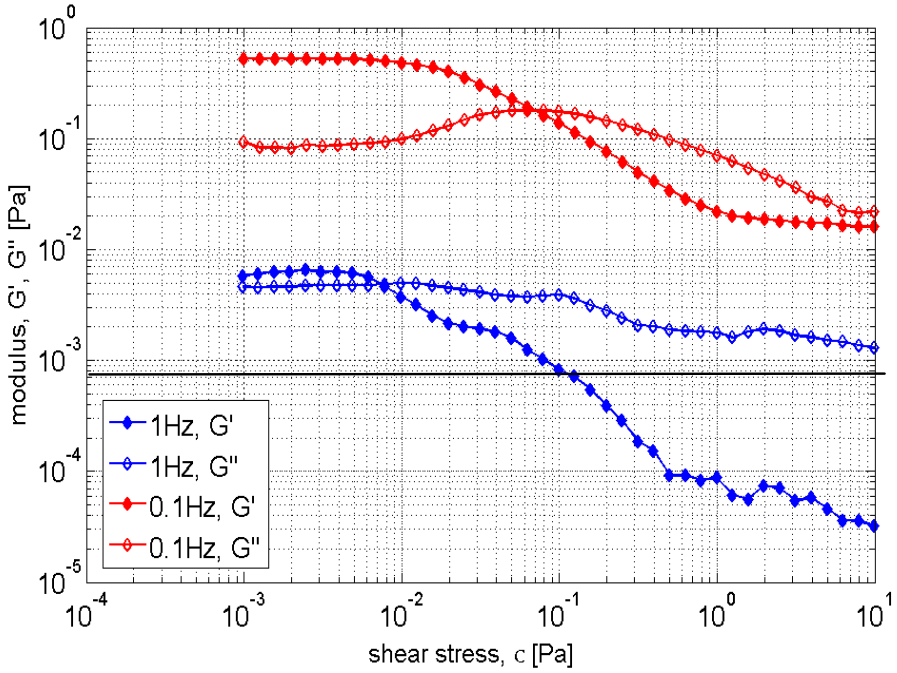

Figure 6.13: Stress sweeps in 0.1% agarose at a frequency of 0.1 Hz and 1 Hz at room temperature. Both G' and G'' become nonlinear at stresses greater than 0.01 Pa; thus, all cone and plate experiments were run with an applied stress of approximately 0.01 Pa.

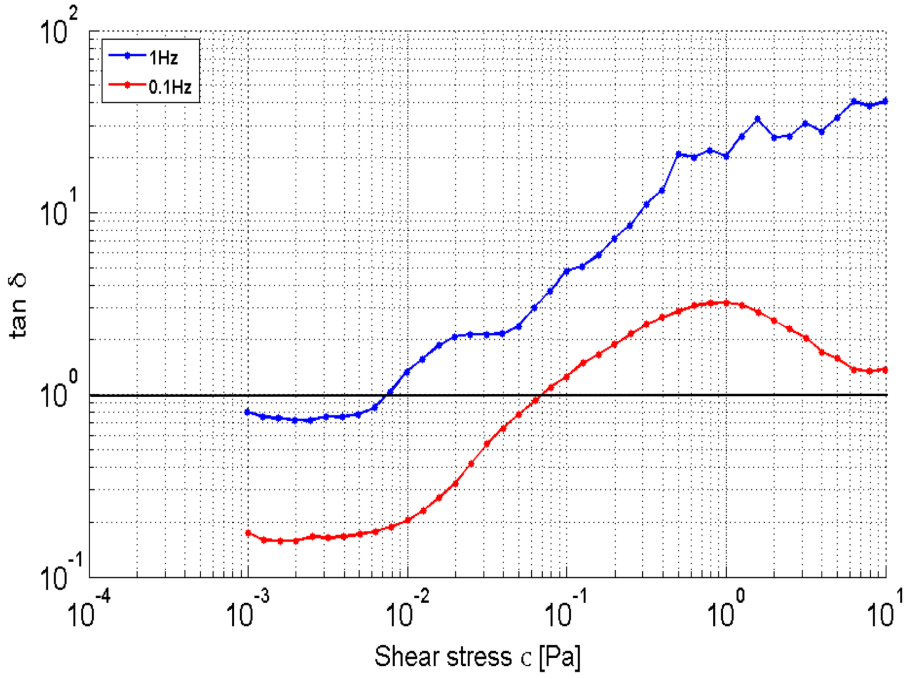

Figure 6.14: Loss tangent in 0.1% agarose at a frequency of 0.1 Hz and 1 Hz at room temperature. When *tan* $\delta < 1$, the material exhibits solid-like behavior, and when *tan* $\delta > 1$, the material exhibits liquid-like behavior.

Throughout my experiments, the beat frequency of my biomimetic system ranges from 0.65 Hz to 16 Hz, but the stress is likely always greater than 0.01 Pa as a cilia tip velocity even as slow as 5 μm/s would apply a stress of ~0.2 Pa. Because of this, and because typical experimental practices to explore higher frequencies such as time-temperature superposition do not work well for agarose, the values for the storage and loss moduli must be estimated utilizing the parameters I have discussed.

The agarose utilized in the following experiments was created by adding low gelling temperature agarose in powder form (Sigma-Aldrich, cat no. A0701) to 150mM sodium chloride. For example, a 0.1% solution requires the addition of 20 mg agarose to 19.98 g NaCl. I typically use a 50 mL conical tube to contain the solution. The tube is wrapped with parafilm to prevent evaporation and tumbled in a 68°C oven for approximately two hours.

Solutions are aliquoted into 2-10 mL aliquots and stored at 4°C for up to one week. Prior to utilizing agarose in an experiment, it must be heated to 65°C such that the liquid form can be easily pipetted. Fluorescent microspheres can then be added to the heated agarose solution, usually at a concentration of 1:300, and this solution is then added to core-shell cilia arrays.

6.3.2 Flow velocity dependence on biomimetic cilia beat frequency

How does the presence of an elastic component to the fluid alter the relationship between cilia beat frequency and flow velocity? Biological cilia in the human lung beat at a frequency of ~8-10 Hz (Chilvers and O'Callaghan, 2000; Hill et al., 2010). This frequency varies from species to species. Does the motivation for assuming a beat frequency stem solely from the mechanical properties of the cilium and its dynein motors, the interaction between cilia and mucus, or both? We can turn this question around and instead ask whether the mucus' viscoelasticity is tuned perfectly for the natural beat frequency of cilia. Does the fact that mucus is a viscoelastic fluid play a role in the response of mucus to cilia beat frequency? To my knowledge, no one has yet explored how altering the beat frequency of biological cilia affects mucus transport rates, though as I mentioned previously, altering the fluid itself does affect transport rates (King et al., 1974).

In this section, I explore the relationship between frequency and flow velocity for 0.1% agarose. Recall from Section 6.2.1, that in a purely viscous fluid, an increase in cilia beat frequency results in an increase in flow velocity, as shown in Figure 6.7 in Section 6.2.1. This relationship is exhibited to an extent in agarose. Figure 6.15 illustrates the dependence

of flow velocity on frequency at five different heights above the core-shell cilia tips located at $z = 10\ \mu$m): $z = 20\ \mu$m, $z = 30\ \mu$m, $z = 40\ \mu$m, $z = 70\ \mu$m, and $z = 100\ \mu$m.

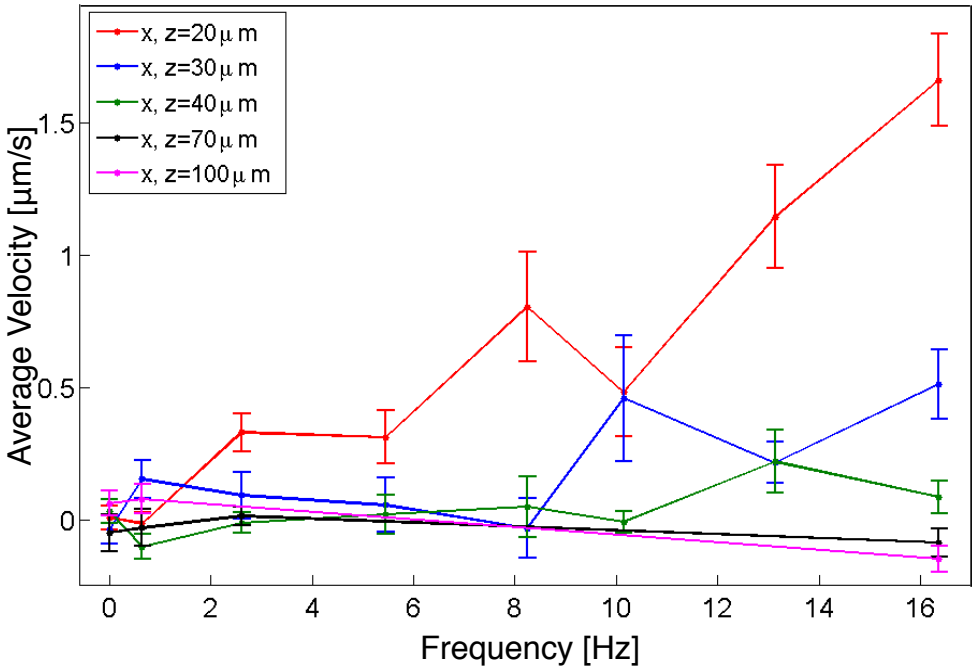

Figure 6.15: Flow velocity in the x-direction tends to increase as the beat frequency of an array of core-shell cilia increases, though not necessarily linearly. Displayed in the plot is the relationship between velocity and beat frequency for five different heights above the cilia tips (located at $z = 10\ \mu$m). For a purely viscous fluid, the relationship would be perfectly linear.

To better understand the velocity-frequency relationship in a viscoelastic fluid, we can build from our purely viscous understanding. In Figure 6.15, notice first the increase in flow velocity which occurs as beat frequency increases. This relationship is similar in viscous fluids; however, in viscous fluids, the proportionality is linear. We can attempt a linear least squares fit to the velocities at $z = 20\ \mu$m; this fit is shown in Figure 6.16. From this fit, a linear relationship does not appear to be a good descriptor of the phenomena. The curve itself has a wave-like form such that the velocity increases and decreases from one

frequency to the next, though globally, flow velocity increases.

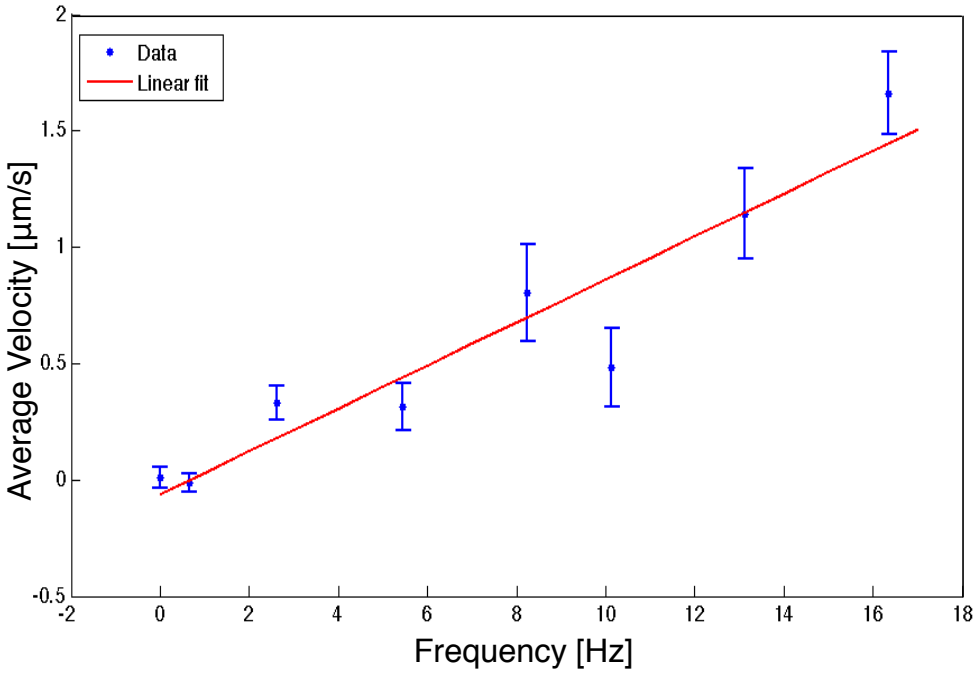

Figure 6.16: To better understand the velocity-frequency relationship in a viscoelastic fluid, we can build from our purely viscous understanding by performing a linear least squares fit to the flow velocity versus core-shell beat frequency. In a viscous fluid, velocity is linearly dependent on cilia beat frequency. In this viscoelastic fluid, 0.1% agarose, the fit does not adequately explain the velocity-frequency relationship. (Data was taken at $z = 20\ \mu$m.)

Besides the global increase in flow velocity as a result of increased frequency, it is also interesting to note the change in flow velocity for a given frequency as a function of increased height above the cilia layer. As shown in Figure 6.15, for the flow at $z = 20\ \mu$m, $z = 30\ \mu$m, and $z = 40\ \mu$m, the onset of a net velocity appears to occur at increased frequency. For example, at $z = 20\ \mu$m, flow begins at a beat frequency of ~2.1 Hz. At $z = 30\ \mu$m, flow is not present until a beat frequency of ~10 Hz, and at $z = 40\ \mu$m, significant flow is not seen until ~13 Hz. For the larger heights (>70 μm), little to no net flow is present. The top boundary of the flow cell for this experiment is located at approximately

$z = 150\,\mu$m. Recall for the purely viscous fluid, when driven at a higher frequency (at 16 Hz specifically), flow is present throughout the entire flow cell, except at the height where the direction of flow begins to reverse due to the cell's enclosed nature (as shown in Figure 6.9). To further investigate flow velocity as a function of frequency, additional data would be collected in both 0.1% agarose and in a viscoelastic fluid with a lower viscoelasticity. The benefit of a lower viscoelasticity would be in the larger flow velocities produced at lower frequencies and larger flow velocities (above diffusion) produced at increased heights above the cilia tips. In this way, a more detailed map of the relationship between velocity, frequency, and height could be achieved.

6.3.3 Directed transport and the flow profile

In addition to the relationship between flow velocity and cilia beat frequency in viscoelastic fluids, the relationship between flow velocity and height, at a given frequency, is also of interest. When biological cilia come into contact with the mucus layer, what mechanical interactions occur? The mucus layer is thought to begin at the cilia tips and extend 15-20 μm above cilia tips in the upper airways (Boucher, 2004). Does the entire mucus layer move? Must the entire mucus layer translate to clear our lungs of pathogens? Understanding the fluid dynamics within the lung could result in improvements in drug targeting and delivery. Before delving into a complex system of layered fluids, however, it is important to first understand the simpler case with only a viscoelastic fluid filling the space throughout and above the cilia layer, which is the topic of discussion in this section.

In Section 6.2.2, I discussed our understanding of the fluid dynamics in the vertebrate

embryonic node, a purely viscous fluid environment. The flow profile (flow velocity as a function of height) was fit to a model called Poiseuille-Couette flow that averaged over an entire array of cilia and treated them as a single plane translating in one dimension at a given velocity. A pressure gradient was included due to the enclosed nature of the node (and experimental flow cell). Moving forward with that flow profile in mind, I expect in a viscoelastic flow profile to encounter a faster velocity near the cilia tips, as we encountered in the viscous fluid, which will decay as the distance from the cilia tips increases. Because the flow cell is sealed, recirculation of fluid may also occur in the viscoelastic case. However, depending on the elastic nature of the fluid, the effect of the core-shell cilia may be short-lived, and a rapid decrease in flow velocity may occur as we move farther from the cilia tips.

Figure 6.17 is the flow profile in 0.1% agarose with the core-shell cilia beating at 16.3 Hz. Note the sharp decay in velocity as a function of height. In just ten microns (between $z = 20$ μm and $z = 30$ μm, the velocity decreases by 70%. In the viscous flow profile, the data shows little, if any, decay in velocity from 20 to 30 μm above cilia tips; the Poiseuille-Couette fit discussed in Section 6.2.2 indicates the velocity falls only 8%. Again, we utilize our model for viscous flow to draw conclusions concerning driven flow in a viscoelastic fluid.

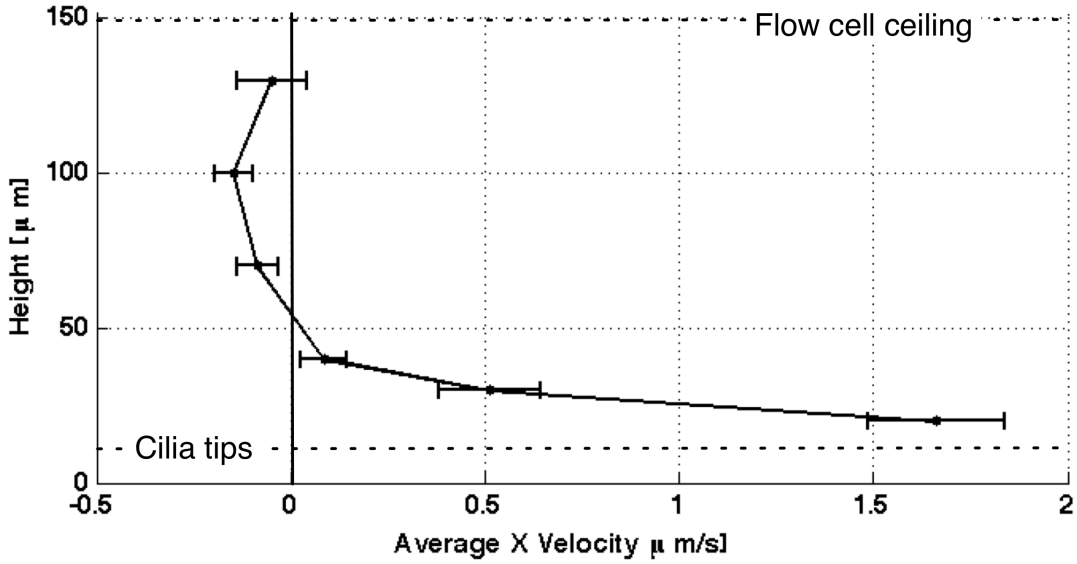

Figure 6.17: The flow profile (velocity as a function of height plotted with height on the y-axis) for core-shell biomimetic cilia driven at 16.3 Hz has a number of expected characteristics. The cilia tips are located at $z = 10$ μm, and just above the tips, the flow has the fastest velocity. Due to the enclosed nature of the flow cell, there does exist a recirculation as height increases. The total height of the flow cell is approximately 150 μm. In addition, the flow velocity decays from its maximum fairly quickly, reaching nearly zero velocity within 20 μm.

To determine whether or not the viscoelastic flow profile was similar in nature to the purely viscous flow profile, the same fit performed on viscous flow (Equation 6.17) was applied to this flow profile. The height of the flow cell is taken as 150 μm, and the viscosity is the zero-shear viscosity of 0.1% agarose (490 cP). Fit parameters include the velocity of the 'moving plate' used to represent the cilia layer, u_0, and the pressure gradient within the flow cell, ∇p. As can be seen in Figure 6.18, the fit (indicated by the dashed red line, 'Fit 1', with $u_0 = 1.5$ μm/s and $\nabla p = 194$ Pa/m) does not accurately represent the nature of the flow, and in the algorithm's attempt to fit both the pressure gradient and velocity at the cilia tips, neither feature is captured well. The velocity is underestimated near the cilia tips, and the recirculation does not occur to the extent predicted by the fit. In attempting to correct

the underestimation of u_0, I will set $u_0 = 3$ μm/s and utilize ∇p as the only fit parameter. Again, as one can see from the figure, the pressure gradient increases to compensate for the increased velocity, and the fit ('Fit 2') is poor. Conversely, I set $\nabla p = 0.0001$ Pa/m, utilizing u_0 as the only fit parameter to capture the low pressure gradient. This third fit ('Fit 3') also results in an underestimated u_0, and still does not accurately capture the shape of the velocity profile.

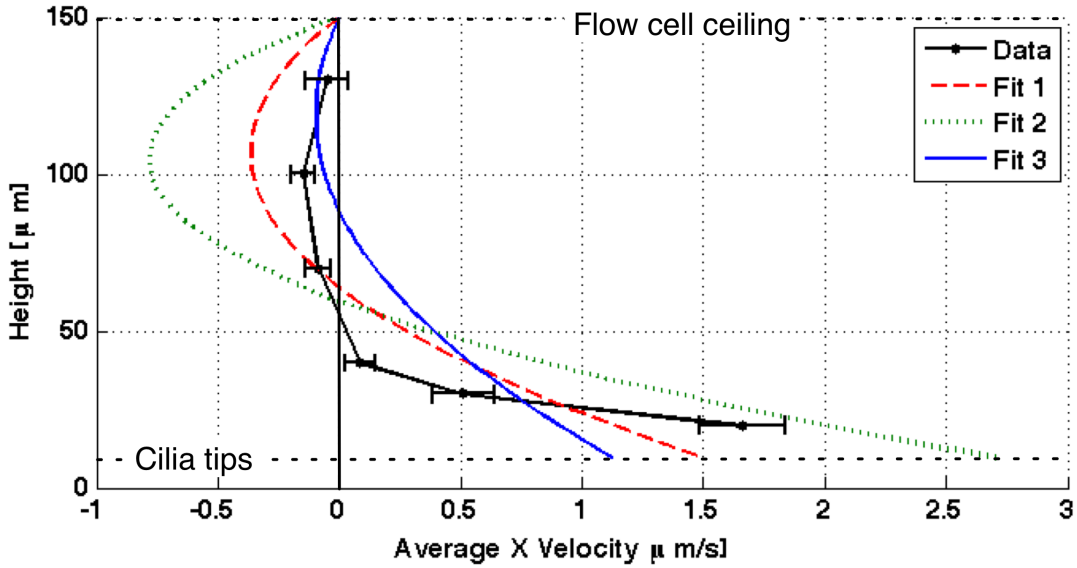

Figure 6.18: The flow profile (velocity as a function of height plotted with height on the y-axis) for core-shell biomimetic cilia driven at 16.3 Hz is not accurately described by the PC model. Three fits using the Poiseuille-Couette flow model are illustrated to indicate the model's inability to accurately describe both the pressure gradient and velocity at the cilia tips. Fit 1 utilizes ∇p and u_0 as fitting parameters, giving values $u_0 = 1.5$ μm/s and $\nabla p = 194$ Pa/m. Fit 2 holds $u_0 = 2.7$ μm/s, considering ∇p a fitting parameter ($\nabla p = 378$ Pa/m). Fit 3 holds $\nabla p = 100$ Pa/m, fitting $u_0 = 1.12$ μm/s.

Alternatively, solving for the y-intercept (value of height z when $u(z) = 0$) of the PC model gives $2u_0\eta/h\nabla p$. By setting the y-intercept equal to the approximate y-intercept implied by the data, we notice that u_0 and ∇p are not two independent parameters. Assuming a constant viscosity and flow cell height, altering one parameter will affect the other, and

applying a fit to one portion of the data (the pressure gradient or velocity at the cilia tips) will result in a curve which does not accurately represent the data in its entirety.

The viscous model for cilia-driven flow does not adequately explain viscoelastic cilia-driven flow, thus a new coarse-grained model must be used for the viscoelastic flow profile in Figure 6.17. Figure 6.19 illustrates the flow profile when the cilia are driven at a frequency of 0.65 Hz. The lower frequency produces nearly zero flow velocity; however, as z increases, the flow velocity appears to alternate direction. This figure is similar to the simulation of Stokes' modified second problem discussed in Section 6.1.4 where an oscillating plate drives shear waves through the fluid. As the height increases, the amplitude of a shear wave originally propagated by the plate decreases. Thus, at lower frequencies which drive little to no net fluid flow cilia produce a flow profile similar to that of Stokes' modified 2nd problem. At higher frequencies, cilia produce a net flow that decays quickly and has some small amount of recirculation, but does not follow PC flow. The coarse-grained model that is relevant to explain driven flow in a viscoelastic fluid may be a combination of an oscillating plane that is also driven at some constant velocity and includes a slight recirculatory flow such as what might be seen with a driven cavity problem that includes an oscillating lid.

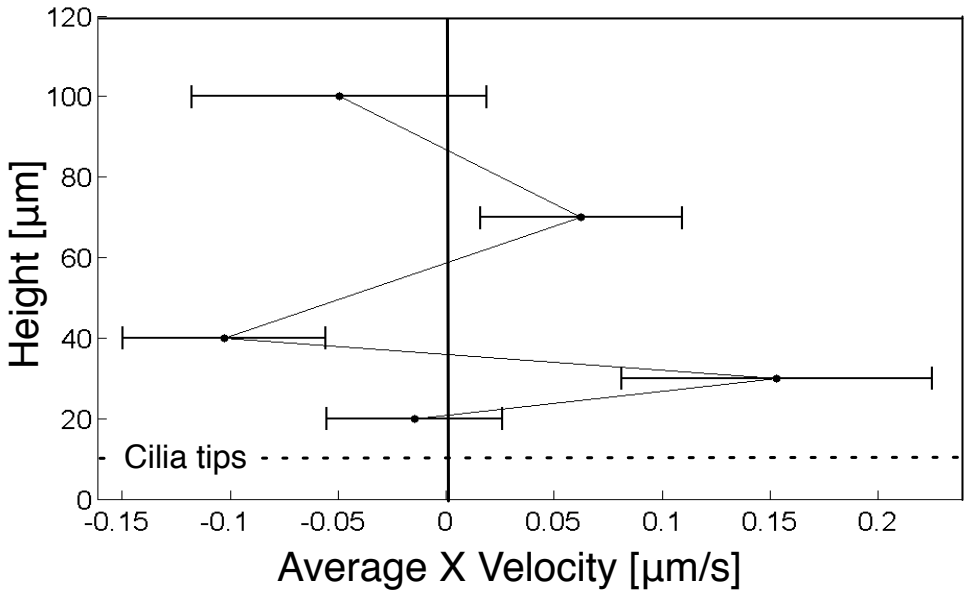

Figure 6.19: Biomimetic cilia driven at 0.65 Hz produce little net flow. As height increases, the velocity appears to alternate direction and decrease.

Modeling of this phenomenon to further our understanding of this coarse-grained cilia model is currently being conducted in collaboration with Dr. Greg Forest and Dr. Paula Vasquez in the Applied Mathematics Program at the University of North Carolina at Chapel Hill. To gain a more detailed picture of the flow driven by core-shell cilia in a viscoelastic fluid, more data must be taken at smaller height intervals above cilia tips and in fluids which are considered less viscoelastic in order to gain better resolution in the velocity measurements. I plan to continue with this research after this doctoral thesis.

I also investigated biomimetic cilia-driven fluid flow in 0.25% agarose, a fluid with a larger viscosity and elasticity. This concentration of agarose is comparable in terms of gross viscoelasticity to pathological COPD sputum as I discussed in Section 6.3.1. At room temperature, the temperature at which 0.25% agarose is comparable to COPD sputum, core-shell cilia are incapable of driving a net transport, even in the same plane as the cilia tips,

though the tracer particles do oscillate in place in response to the cilia motion. To determine whether this lack of transport was due to the inadequacy of a particular biomimetic cilia array or due to the effect of the increased viscoelasticity of the fluid, I increased the temperature of the viscoelastic fluid, investigating cilia-driven flow at both 35°C and 65°C. As temperature increased, the tracer particles experienced a net displacement in response to the beating cilia. Figure 6.20 is a collection of minimum intensity projections of tracer particle paths at the cilia tips and 20 μm above the cilia tips as the temperature increases. The cilia were driven at 16.3 Hz, and to ensure the flow at 65°C was not caused by drift, data was taken with the cilia motionless, verifying that the motion was indeed diffusive.

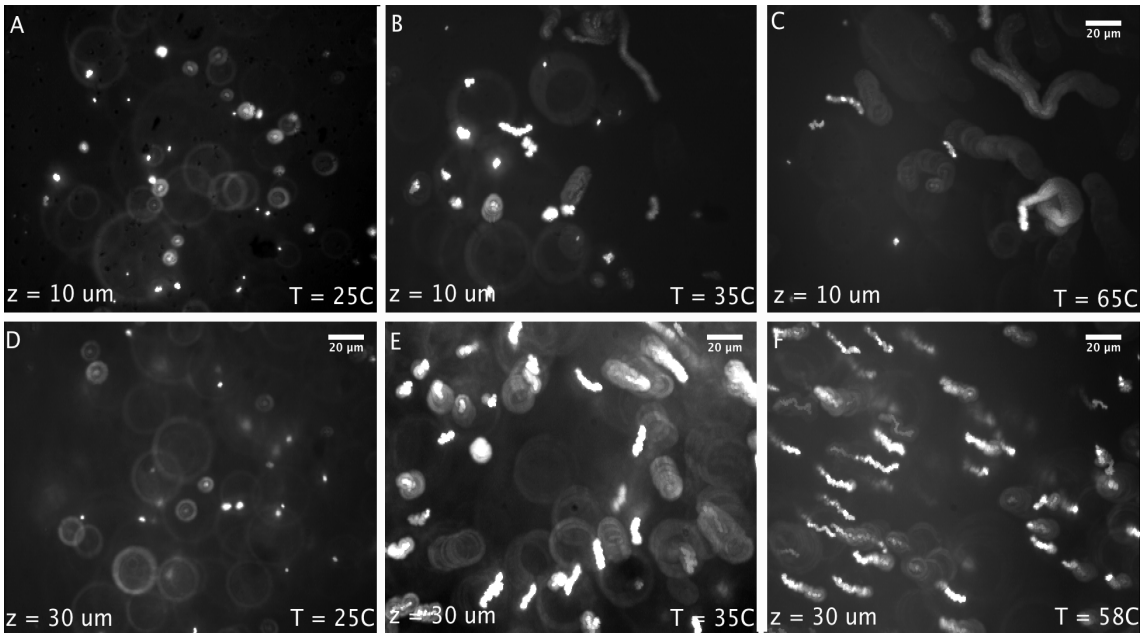

Figure 6.20: Core-shell cilia driven at 16.3 Hz produce no net transport in 0.25% at room temperature, but as the temperature is increased to 65°C, tracers begin to move, and a net flow arises. The onset of driven, directed flow at higher temperatures implies that the fluid itself prevents the occurrence of cilia-driven flow, and as I discuss in the text, the viscoelasticity of the fluid causes a diminished cilium amplitude. The three minimum intensity projections display the paths of fluorescent tracer particles over 30 s at the cilia tips, $z = 10\,\mu$m, and 20 μm above the cilia tips, $z = 30\,\mu$m, for three different temperatures: (a/d) 25°C, (b/e) 35°C, (c/f)~ 65°C.

Imaging the cilia tips in brightfield mode at 25°C and 65°C indicates a large increase in amplitude with the increase in temperature, corresponding with the increased flow velocity. The amplitude increased by approximately 200% with an increase in temperature of 25°C to ~58°C. The viscoelasticity of 0.25% agarose is highly dependent on temperature. At 25°C, 0.25% agarose clearly behaves as a viscoelastic solid ($G' > G''$). However, as the temperature increases, the storage modulus decreases until at 65°C, $G'' > G'$, as shown in Figure 6.21.

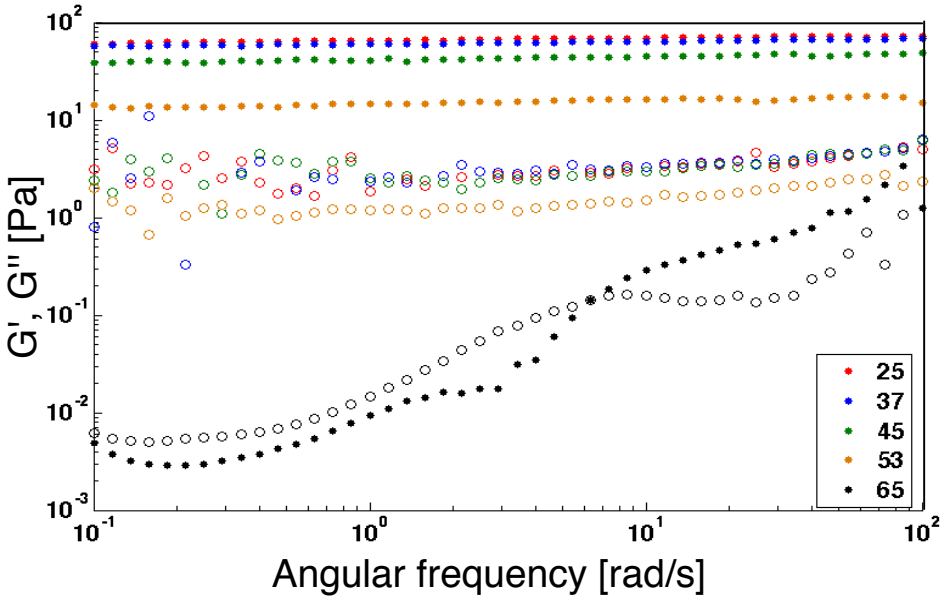

Figure 6.21: At lower temperatures, the storage modulus G' (closed circles) is greater than the loss modulus G'' (open circles), indicating that the fluid behaves as a viscoelastic solid. However, as temperatures near 65°C, $G' < G''$, and 0.25% agarose exhibits more liquid-like behavior.

6.3.4 Implications for biology and technology

The development of a fabrication technique for arrays of artificial cilia which are of a similar size to biological cilia and which are capable of propelling viscoelastic fluids like

their biological counterpart is a remarkable addition to our current set of experimental tools for the investigation of cilia-driven flows. Preliminary analysis of these biomimetic cilia-driven flows in a viscoelastic fluid similar to healthy HBE mucus indicate the effects of cilia are still felt by the fluid as far as thirty microns above the cilia tips. The density of an array of biomimetic cilia is two million cilia per square centimeter. Biological cilia are approximately 200 times more dense than biomimetic cilia; thus the effects of biological cilia are likely to be further reaching than our biomimetic cilia. Figure 6.22 shows a micrograph of a human bronchial culture six weeks old from Boucher et al. (2004). Notice the distinct fluid layers which have been labeled in the image. The mucus layer ranges from approximately $16-21$ μm thick in this culture (Boucher, 2004), well within the thirty micron range affected by my biomimetic cilia array, perhaps indicating the effects of airway cilia may be felt throughout the entire mucous layer. Before reaching such a hypothesis definitively, however, a fluid composition more similar to the layered fluid found in the lung should be utilized to further explore interactions between cilia and the mucous layer.

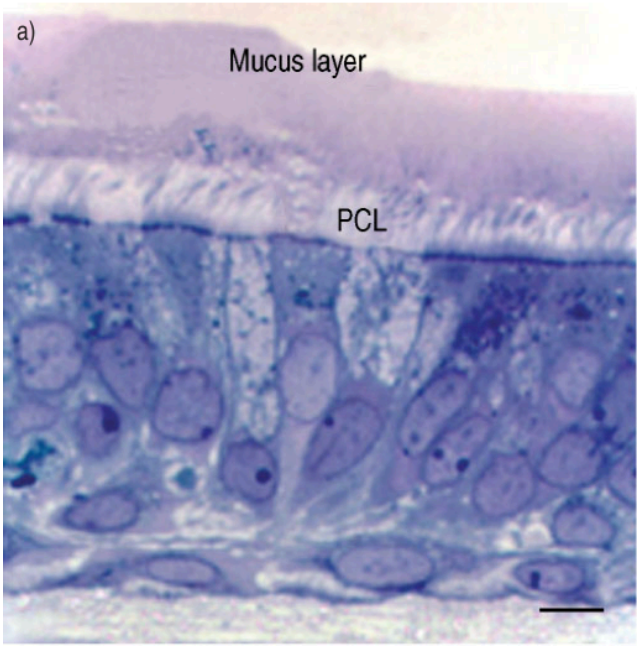

Figure 6.22: Reprinted from Boucher et al. (2004). A light micrograph of a six week old human bronchial culture indicates the location of the periciliary layer and the mucus layer. The scale bar is 10 μm (Boucher, 2004).

In addition, our measurements of biomimetic cilia-driven flow in a viscoelastic fluid similar to pathological COPD sputum indicate that no net transport is present. For patients who suffer from airway inflammations, the amount of mucins produced by epithelial mucous cells is greatly increased. With COPD specifically, the fourth leading cause of death in the United States, the development of a chronic cough occurs to assist in clearing the thicker mucus as the typical cilia-assisted mucociliary clearance method is ineffective in smaller diameter airways. This lack of clearance causes recurrent infections in the lung, which are also exhibited by patients who suffer from cystic fibrosis. Individuals with cystic fibrosis suffer from a nearly complete lack of mucociliary clearance (Williams et al., 2006), as mucus concentrations reach 8%. This lack of clearance is exhibited by my biomimetic system, making this system a potential platform to study the effects of pharmaceuticals on

breaking up highly concentrated mucus and the mucociliary clearance process before utilizing animal models or human patients. In the future, biomimetic cilia arrays could also be fabricated in small diameter microfluidic channels to represent the geometries of the human lung, thus providing a more physiologically relevant way to study clearance in both the larger and smaller airways.

In technology, increasingly viscoelastic fluids, such as biofluids, are being investigated within microfluidic systems. Nghe et al. recently reported on several behaviors exhibited by viscous fluids in microfluidic systems, including the breakdown of polymers, how polymer solutions flow, and shear banding and instabilities (Nghe et al., 2011). For further exploration of viscous and viscoelastic fluids at the micron scale, devices which can be integrated within a channel to efficiently manipulate such materials must have large dynamic responsiveness. Several methods have been devised to accomplish these tasks including silicon diffuser micropumps which utilize an oscillating diaphragm to move more viscous fluids (up to 900 cP) through a channel (Andersson et al., 2011), and oscillating bubbles generated by piezoelectric discs inside a channel to mix glycerol solutions of varying viscosities (Wang et al., 2011). However, pumping diaphragms require cleanroom microfabrication techniques such as deep reactive ion etching, and oscillating bubbles are currently capable of mixing fluids with viscosities only up to 45 cP. Earlier in this chapter, I discussed the ability of our FFPDMS cilia to both pump and mix fluids simultaneously, and my core-shell biomimetic cilia are now poised to be applied for this same function in high viscosity and viscoelastic fluids.

Core-shell cilia are excellent microactuators in highly viscous and viscoelastic fluids

primarily due to their ability to maintain sufficient amplitude. Figure 6.23 depicts the change in amplitude as a function of applied magnetic field in PBS (circles), 0.1% agarose (squares), and 0.25% agarose (triangles) for the frequencies of 0.65 Hz (open symbols) and 16.3 Hz (filled symbols). (Amplitude is measured as half of the major axis of the ellipse swept out by cilia performing an upright circular beat.) As discussed in Section 4.3.3, the saturation magnetization of Ni is around 150 mT; this is evident in the figure as the amplitude of Ni core-shell cilia does not increase when magnetic fields approaching 100 mT are applied. For the lower applied fields ($<$ 10 mT), the relationship between amplitude and magnetic field appears to be linear, but due to Ni's saturation magnetization, the curve begins to flatten out. Because of this sharp initial increase in amplitude followed by a very gradual increase due to magnetic field saturation, I can fit logarithmic curves to each set of amplitude data to determine the largest possible amplitude at magnetic saturation (based on material type and frequency) at room temperature. These fits are shown in Figure 6.23. With more data across multiple samples, the fits can become more accurate, especially at higher fields for the less viscoelastic fluids and lower fields for the more viscoelastic fluids, and relationships for the coefficients of the applied field (x in the legend in units of mT) based on fluid type and frequency may emerge. As they currently stand, these fits do supply me with an experimental limit for my biomimetic system for these particular fluids.

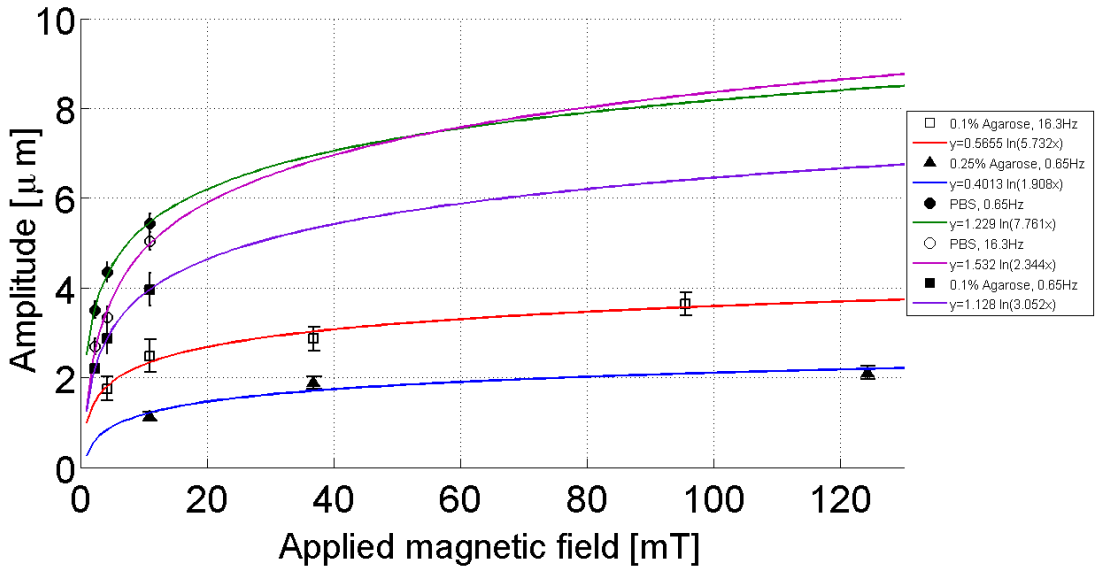

Figure 6.23: Amplitude as a function of applied magnetic field for DPBS (circles), 0.1% agarose (squares), and 0.25% agarose (triangles) for the frequencies of 0.65 Hz (open symbols) and 16.3 Hz (filled symbols). All measurements were taken above the same patch of biomimetic cilia. Plotted for each data set is a logarithmic fit, indicating the maximum amplitude possible at magnetic field saturation.

By considering only a single magnetic field, 11 mT, and comparing the amplitudes across fluids (across the different viscoelasticities), it becomes immediately apparent that the lack of flow produced by cilia in 0.25% may be associated with the diminished amplitude exhibited by the cilia. At 0.65 Hz, the difference in amplitude between PBS and 0.25% agarose is ~79%, whereas the difference in amplitude between PBS and 0.1% agarose is only ~27%. Our ability to detect and measure these amplitudes even in fluids with high viscosities or viscoelasticities lend my core-shell cilia to an entirely new application–that of measuring the rheology of fluids at the microscale. In the next chapter, I discuss the application of my core-shell cilia as microrheometers, capable of detecting fluid changes as sensitive as the formation of a blood clot utilizing only ten microliters of whole blood.

Chapter 7

Core-shell Biomimetic Cilia as a Rheometer

In addition to the manipulation of fluids at the microscale, biomimetic cilia show potential as a technology for measuring fluid properties such as viscosity and elasticity. The dynamic response to an applied magnetic field depends on the viscoelasticity of the fluid in which the cilia beat. As I discussed in Section 6.3.4, for the same applied field, a fluid with larger viscous and elastic components will cause a decrease in core-shell cilia amplitude. However, because core-shell cilia are highly responsive, this diminished amplitude is still easily detected and measured even in viscoelastic fluids, making core-shell cilia an ideal candidate for microrheometry measurements.

Not only can core-shell cilia be utilized to measure a static fluid or the differences between the rheology of two fluids, but they can also measure the time evolution of a single fluid. As the fluid becomes more viscoelastic around a cilium, the amplitude of the cilium decreases for a constant driving force. More specifically, in a viscoelastic fluid such as a blood clot, as the clot forms around biomimetic core-shell cilia, the amplitude at the onset of clot formation is very different from the amplitude after clot formation has occurred.

This difference in amplitude may be due to a number of factors. The fibers surrounding a cilium may create a higher viscosity fluid due to the large number of no-slip boundary conditions created by fibrin formation (Spero et al., 2011). A second possibility is that the fibers create a physical cage surrounding the cilium, restricting its movement through physical interactions. Understanding blood clot formation and structure is vital as clotting or bleeding disorders are a leading cause of morbidity in the world (Hess et al., 2008) and is currently a very active area of research. As core-shell cilia are responsive to changes in clot formation, I have utilized core-shell arrays to develop a method for the measurement of blood clot formation. The core-shell system requires only ten microliters of fluid to obtain clotting times which are traditionally obtaining using coagulation tubes of blood and may be utilized at the site of injury.

The design and creation of a blood coagulation system utilizing core-shell arrays fulfills a need in the field of medical diagnostics for a low-cost, hand-held, quantitative measure of blood clotting times and clot elasticities. Our device development is motivated by both the far-reaching effects of coagulation disorders and the shortcomings of current medical diagnostics. I have used core-shell arrays to obtain blood coagulation times for both animal plasma and whole blood, and I will present this data, comparing and contrasting my results with current measurement techniques. I have found that because of their highly responsive nature, core-shell cilia appear more sensitive to the onset of clot formation than traditional light scattering methods, also known as turbidity measurements, and reproduce the capabilities of current measurement techniques (thromboelastography) while allowing point-of-care operation.

7.1 Core-shell actuators for use as microrheometers

The vibrating cantilever is an ideal candidate for microrheometry measurements, as the size is easily controlled during the fabrication procedure, the response of the cantilever may be varied depending on the type of material used in its construction and the fluid in which it is immersed. For optimum performance, a microcantilever's stiffness may be matched to its application. To determine a fluid's viscosity and elasticity, both the phase between the driving force and microcantilever and the amplitude (or deflection) of the microcantilever should be known. Typical rheometers utilize both amplitude and phase to determine the viscous and elastic responses of the fluid. The portion of the actuator's response in-phase with the driving force corresponds to the elastic component of the fluid, and the portion of the actuator's response out-of-phase with the driving force by $\pi/2$ corresponds to the viscous component of the fluid (Barnes, 2000). Additionally, actuator response (both amplitude and phase) in air can be measured and compared to actuator response in a specified fluid to determine dynamic moduli. In 2010, Christopher et al. utilized this method in various linear viscoelastic materials with a MEMS microrheometer which essentially mimicked a macroscale cone and plate rheometer. The microrheometer was modeled mechanically as a mass suspended between two springs, oscillating in a viscoelastic fluid treated as a spring and dashpot in parallel with a single relaxation time (Christopher et al., 2010). (The Maxwell model is a spring and dashpot in series.)

For core-shell microactuators, the measurement of amplitude as a function of frequency is done using brightfield microscopy; however, there is currently no method in place for the

measurement of phase. Future project instrumentation could include a synced magnetics element and video capture system such that the rotation of the magnetics is triggered at the start of the video and is always known at a particular instant, allowing for the calculation of the phase delay. Additionally, with a synced magnetics and video system, utilizing an electromagnet to drive core-shell cilia would allow for more control over the sinusoidal input signal. For current analysis of the deflection in a purely viscous fluid, we consider only the amplitude of the rod and assume the rod is in-phase with the driving force. Following Brucker's treatment, the amplitude of a microcantilever exhibiting small deflection is given as (Brücker et al., 2007)

$$A(\omega) = F_0 \left(\left(\frac{60}{11} \frac{EI}{L^3} \right)^2 + \left(\frac{52}{33} \frac{\pi \eta L}{ln(L/2D)} \right)^2 \omega^2 \right)^{-1/2} \tag{7.1}$$

Recall that E is the elastic modulus, I is the second moment of inertia, η is the fluid viscosity, and L and D are the length and diameter of the cantilever. Note that the model considers only small deflections, and the amplitude of core-shell cilia is not small, but on the order of half the actuator's length (several microns).

For core-shell cilia, 10 μm long and 0.55 μm in diameter, the decay of amplitude as a function of frequency in PBS (η_0 = 1 cP) and 2.5 M sucrose (η_0 = 100 cP) is shown in Figure 7.1. The data is indicated by open (PBS) and filled (sucrose) circles. Fits were performed on each data set utilizing the model above with fitting parameters F_0, E, and η. The fit of the model to PBS data appears to follow the trend fairly well, and lies within experimental error. Fitting parameters for the PBS fit are F=0.32 nN, E= 2.0 MPa, and η=10.3 cP. The viscosity fit parameter is a factor of ten larger than it should be, indicating

either that the cilium is more damped than the model suggests or that the experimentally obtained amplitude is underestimated and should be larger than was measured. If the cilia are more damped than the model suggests, an additional term may be needed to account for an internal damping or potential effects on the rod from the no-slip boundary condition at the floor. When performing these experiments, efforts are made to drive the microrods in an upright conical beat, though often the microactuator tips may drop closer to the floor during part of a beat. The amplitude is measured experimentally with videos captured at 120 frames per second (8 ms between frames). Cilia tips spend a very short period of time at maximum amplitude (the period of motion at 16 Hz is ~60 ms and 7 frames are captured for each beat), and the motion at higher frequencies can be blurred, making it difficult to approximate the precise location of a cilium tip. For 2.5 M sucrose, the fit appears to match the data very well. However, the fit parameter η=36.2 cP, a large difference from the expected 100 cP measured on a cone and plate rheometer. Also measured on the cone and plate rheometer was a mixture of 75% 2.5 M sucrose - 25% PBS. The viscosity of this fluid mixture was ~24 cP. When exchanging fluids, efforts are made to entirely replace the previous fluid; however, fluid mixtures do occur during fluid exchange as the fluid cell size surrounding the array of microactuators is less than 50 μL. Thus, it is reasonable to assume the fluid surrounding the cilia array was a mixture of PBS and sucrose. The factor of ten increase in fluid viscosity is not seen in the fit of the model to data taken in 2.5 M sucrose, though the elastic modulus does increase compared to buffer by 1/4, implying the rod is stiffer in sucrose than in buffer. Note that the model I fit to both buffer and sucrose data makes a number of assumptions to obtain the constants in Equation **??**,

including that of a small amplitude deflection, a sinusoidally-varying driving force, and a uniform, homogeneous microactuator. Thus, the fits I receive based on these assumptions are reasonable.

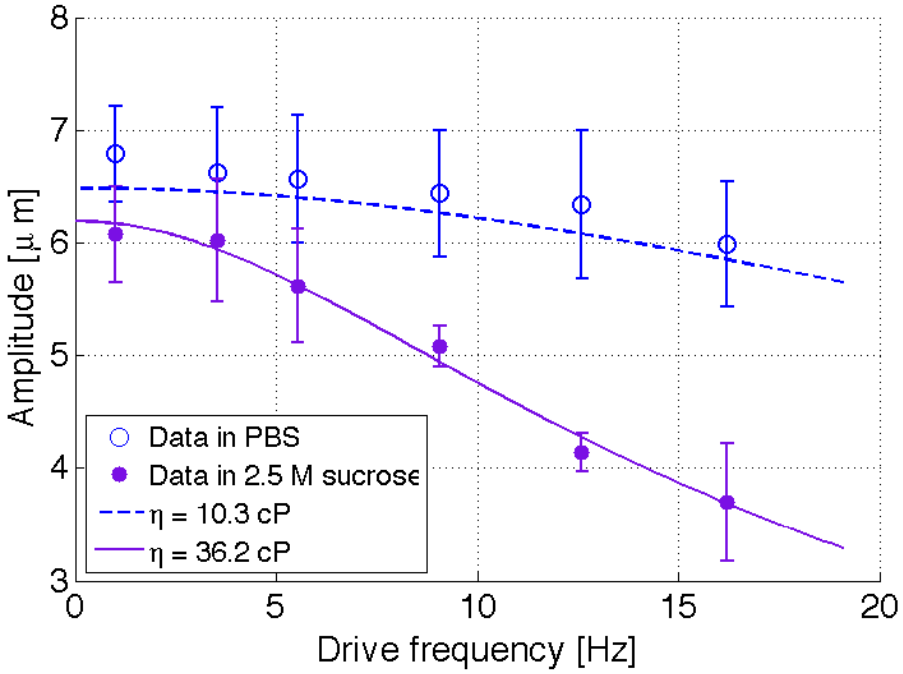

Figure 7.1: Data for core-shell rod amplitude dependence on frequency in two fluids of differing viscosities, PBS (open circles), η_0 = 1.05 cP, and 2.5 M sucrose (filled circles), η_0 = 100 cP. The rod geometry is approximately 10 μm long by 0.55 μm diameter, and the experimentally applied magnetic field ranged from 13-18 mT. The solid and dashed lines on the plot are a fit of Equation 7.1 to the data with fit parameters magnetic force, elastic modulus, and fluid viscosity. The parameters for the PBS fit are F=0.32 nN, E= 2.0 MPa, and η=10.3 cP. The parameters for the fit to sucrose data are F=0.38 nN, E=2.5 MPa, and η=36.2 cP.

In buffer, the need for a larger viscosity parameter to fit cilia amplitude in the model implies the model considers the core-shell rods more damped than they are or experimental measurements underestimate rod amplitude. There is still much work to be done in creating a better model, one that includes the contributions of elasticity as well, before core-shell rods can be used as a robust microrheometry technique. The application of core-shell cilia

to the measurement of coagulation times is unrestricted by the need for future work, as measurements across blood samples may initially be compared relative to one another.

7.2 Coagulation cascade and coagulopathies

The formation of blood clots, which act to stem the flow of blood from damaged blood vessels, is known as coagulation. Coagulation ultimately forms fibrin strands that bundle together and form networks to block blood flow. At least twenty different clotting proteins work together to create these fibrin networks, some as zymogens which are precursors of inactive proteolytic enzymes and some as cofactors that accelerate reactions. A detailed discussion of the clotting cascade can be found in Appendix A, as well as a table, Table A.1, listing the coagulation proteins in the order of their appearance in the coagulation process (Jesty, 2008). Figure 7.2 is an overview of the coagulation cascade, illustrating the primary pathway for blood clot formation.

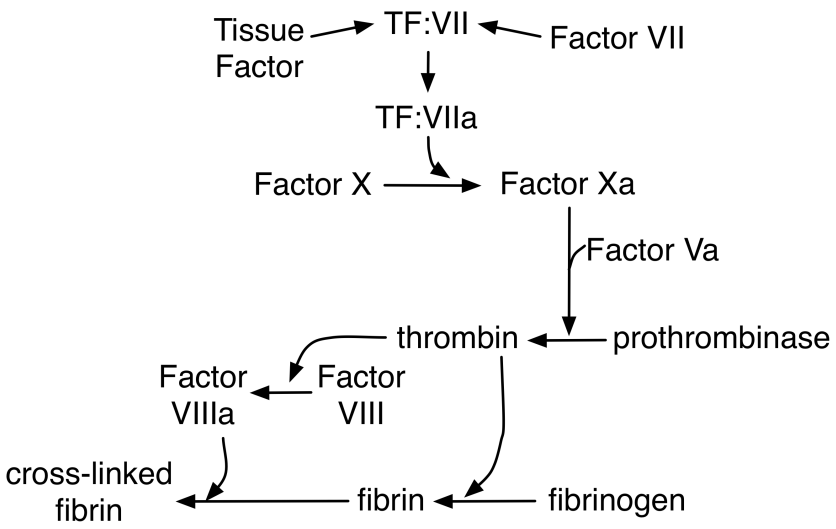

Figure 7.2: Schematic depicting the integral coagulation factors and cofactors in the primary pathway for blood coagulation initiation. A deficiency in factor VIII may cause hemophilia, and if a variant of factor V is present, then factor Va will not be present, and an individual may suffer from thrombosis (Jesty, 2008; Mann and Ziedins, 2005).

If certain factors in the coagulation cascade are deficient or defective, the cascade will be disrupted and coagulopathies, which are clotting or bleeding disorders, can occur. Clotting may occur too slowly as in hypocoagulability where a possible end result, if untreated, is an increased bleeding or hemorrhaging, or too quickly as in hypercoagulability where the result, if untreated, is an increased risk of developing blood clots, also known as thrombosis. A deficiency or defect in factors VIII or IX, which are responsible for crosslinking fibrin and activating factor X, respectively, may cause hemophilia in patients (Mann and Ziedins, 2005). Conversely, if a variant of factor V, called factor V Leiden, is present in place of factor V, then factor Va will never be inactivated, and a patient will be at a much higher risk for thrombosis. Coagulation disorders such as these may be hereditary like hemophilia, acquired like liver disease, or the result of traumatic injury, also known as trauma induced coagulopathy (TIC). Worldwide, trauma is the leading cause of death

for people under age 36, and of those individuals, TIC is involved in 25%. One in four trauma patients is now identified as being admitted to an emergency room or department with a coagulopathy and a corresponding four fold mortality increase and increased organ dysfunction and failure (Hess et al., 2008; Niles et al., 2008).

The mechanism for early coagulopathy is unknown, but many potential factors are thought to contribute including tissue trauma, shock, blood loss, blood dilution, acidemia (low blood pH levels), hypothermia, and fibrinolysis (Brohi et al., 2007; Hess et al., 2008; Niles et al., 2008). The presence of tissue damage such as that obtained from a crushing injury like an automobile accident or explosion, initiates both coagulation and fibrinolysis as damage to the endothelium releases tissue plasminogen activator (tPA) and exposes collagen type III and tissue factor (TF). Fibrinolysis occurs as tPA is a protein that catalyzes plasminogen to plasmin, the enzyme that breaks down blood clots. Because of collagen and TF's increased presence along with other factors such as VIIa, thrombin and fibrin formation occur, and coagulation becomes an additional result of tissue damage. This tissue trauma drives not only fibrinolysis and coagulation, but also shock, which in turn dilutes coagulation. Attempts to resuscitate patients with intravenous fluids compound the dilution of coagulation factors, reducing the patient's blood clotting ability. Additionally, any uncontrolled bleeding will lead to acidemia and hypothermia, both of which impair and inhibit the activity of coagulation factor complexes, further worsening the coagulopathy. While this area of research is still very active, it is clear that trauma compromises healthy coagulation. Figure 7.3 diagrams several of the potential mechanisms responsible for trauma induced coagulopathy (Brohi et al., 2007; Hess et al., 2008).

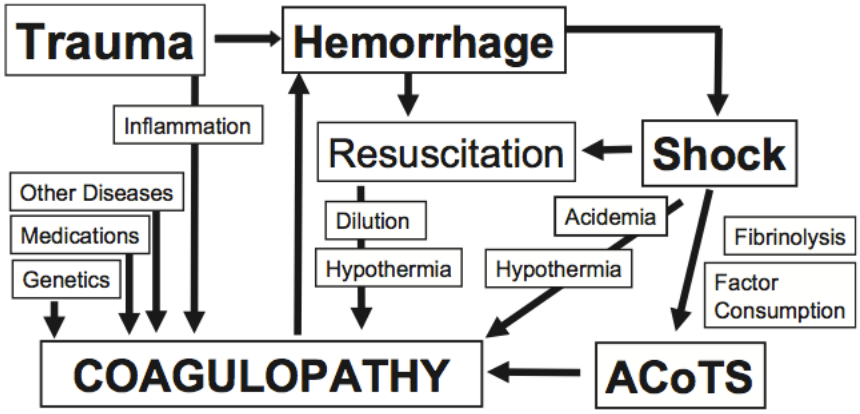

Figure 7.3: Reprinted from Hess et al. (2008). Diagram of mechanisms responsible for trauma induced coagulopathy. Tissue damage drives both fibrinolysis and coagulation, causing hemorrhaging and shock. This is typically met with resuscitation attempts which dilute the needed coagulation factors. All of this leads to the development of a coagulopathy (Hess et al., 2008). (ACoTS stands for Acute Coagulopathy of Trauma-Shock.)

My purpose in describing factors involved in trauma induced coagulopathy is to illustrate the saliency of early and immediate coagulopathy detection with a sensitive point-of-care (POC) device. Blunt injuries such as those obtained from a non-penetrating trauma or force like a baseball bat or an auto accident account for 90% of civilian emergency room admissions (Niles et al., 2008). At or near the site of injury, treatments given immediately after injuries are sustained, which are intended to resuscitate the patient, contribute to the development of a coagulopathy by diluting coagulation factors. Intravenous fluids containing excess ionic chloride reduce the activity of the Xa-Va complex shown in Figure 7.2 by 50-90% at pH levels 7.2-6.8. Reduced activity levels lead to prolonged clotting times as well as a reduced clot strength (Hess et al., 2008). Statistics such as these indicate that diagnostic tests with the ability to rapidly assess hemostasis-related parameters immediately after injuries occur are critical to the treatment and therapy of patients suffering from TIC. These diagnostic tests also must be at or near the site where injuries are sustained

to avoid the opportunity for treatment which could aggravate the coagulopathy, such as the administration of intravenous fluids and inadvertent dilution of coagulation factors. Current measurement techniques for coagulation are discussed in the following section.

7.2.1 Current measurement techniques

Multiple clinical diagnostics currently exist to investigate the clotting time and/or the strength of a blood clot: (i) activated partial thromboplastin time (APTT) and prothrombin time (PT), and (ii) Thromboelastography (TEG) and Rotation Thromboelastography (ROTEM). The APTT and PT tests are coagulation tests that measure the time for citrated blood or plasma samples to clot and can lead to the diagnosis of a clotting disorder. When used in combination, the tests assist in determining which pathway to clotting is deficient, the intrinsic or extrinsic. The intrinsic pathway, or contact activation pathway, is measured by the APTT test, and the extrinsic pathway, or tissue factor pathway, is measured by the PT test. Both pathways are discussed in more detail in Appendix A.

These two coagulation tests are both plasma-based assays, requiring much in the way of blood processing as citrate must be added to avoid clotting before the assay is performed, and the sample must be spun down to separate the plasma and blood cell components. In addition, results from these tests are based on only the very small amount of thrombin generated during the initial coagulation step. Because of this, PT and APTT tests have been considered insufficient in predicting patient bleeding (Segal and Dzik, 2005).

TEG and ROTEM are in a class of assays known as viscoelastic haemostatic assays (VHA) and utilize whole blood to provide information about not only clotting time and the

formation of fibrin, but also clot strength and fibrinolysis. Assays which use whole blood are preferable because they include not only the plasma contributions to the clot, but also the contributions from red and white blood cells and platelets. In addition, further processing steps are unnecessary. Mechanically, both TEG and ROTEM utilize a pin and cup system where the relative phase of the pin and cup provides a measurement of the parameters previously mentioned. Figure 7.4 depicts this pin and cup along with a schematic of a TEG/ROTEM output curve (Johansson et al., 2009). For TEG measurements, the pin is a stationary torsion wire, and whole blood (360 μL) is added directly to the cup. The cup is rotated through an angle of 4.75° over 10s (0.0013 Hz or 6 rotations/min), and as the clot forms between the cup and pin, the pin begins to rotate with the cup. The amplitude of this rotation is measured and the trace in Figure 7.4 is generated. For ROTEM, the cup is initially stationary, and the pin which is attached to an optical detector, rotates through 4.75° (Johansson et al., 2009).

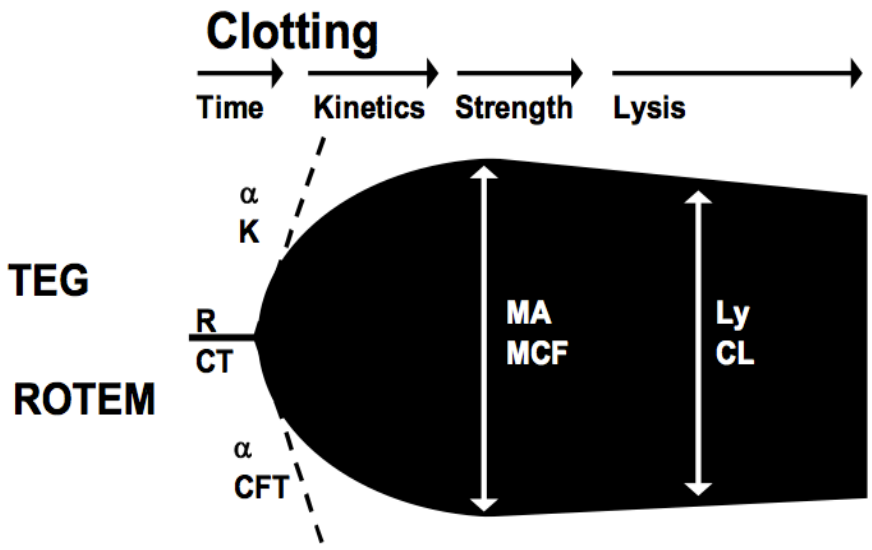

Figure 7.4: Reprinted from Johansson et al. (2009). A schematic of a typical TEG (upper portion) and ROTEM (lower portion) measurement. The variables indicated on the curve are reaction time R and clotting time CT, clot formation time K and CFT, alpha angle α, maximum amplitude MA and maximum clot firmness MCF, and clot lysis Ly and CL (Johansson et al., 2009).

Because the TEG and ROTEM measurements are very similar in nature, I will restrict my discussion to TEG. I note here that measurements taken by TEG in the determination of clotting time are quantitative; however, measurements which parametrize blood clot strength are qualitative in nature, utilizing relative measurements based on the definition of a normal blood sample. In Figure 7.4, the R time is the time to initial fibrin formation and indicated by the point at which the trace's amplitude begins to increase. Initial fibrin formation is considered detectable when the amplitude of the pin reaches 2 mm (Johansson et al., 2009). The K time is the time for a clot to reach a specified level of clot strength (or a pin amplitude of 20 mm), which is not equal to the time for a clot to reach its maximum strength (or maximum amplitude MA). The time for a clot to reach MA is called the time to maximum amplitude, or TMA. Both the R and K times are prolonged with the presence of

anticoagulants, and shortened with the presence of higher levels of fibrinogen. Finally, the alpha angle α supplies information on the kinetics of a clot's development and measures the rapidity of fibrin build up and cross-linking by measuring the slope of the line formed by the R and K times; larger α typically indicates more fibrinogen is present. The day-to-day variation in VHA measurement is approximately 5-15% depending on the parameter (Johansson et al., 2009).

In addition to clot formation, TEG and ROTEM provide information on clot lysis and the degradation of the clot over time. Variables such as $LY30$ and $LY60$ indicate the percent lysis after 30 and 60 minutes, respectively, by measuring the reduction of area under the TEG curve from the time of MA to the amplitude of oscillation at 30 or 60 minutes. Figure 7.5 consists of several different TEG tracing shapes which indicate various coagulation dysfunctions. Figure 7.5B may be the result of a Factor V variant; Figure 7.5C may be the result of a deficiency in Factor VIII.

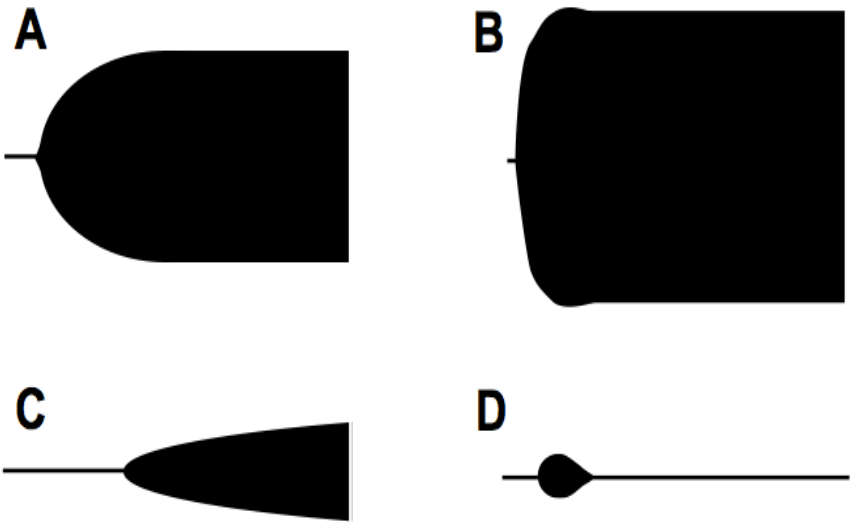

Figure 7.5: Reprinted from Johansson et al. (2009). (A) Normal. (B) Hypercoagulability, the propensity to develop thrombosis (blood clots); could potentially result from the presence of a variant of Factor 5. (C) Hypocoagulability, the lack of blood clotting; could potentially result from a deficiency or defect in Factor VIII. (D) Primary hyperfibrinolysis, enhanced fibrinolytic activity which may lead to bleeding (Johansson et al., 2009).

Viscoelastic haemostatic assays have been shown to be more effective than the PT and APTT tests in providing relevant diagnostic information and guiding therapy for trauma cases in more than twenty clinical studies and three randomized clinical trials (Johansson et al., 2009). When compared to PT/APTT tests, the utilization of VHA has reduced the number of required transfusions and re-examinations. Johansson et al. in 2009 provided a thorough review of studies from 1985-2009, evaluating the inefficiency of PT/APTT coagulation test results as compared to TEG and ROTEM results (Johansson et al., 2009).

Though TEG and ROTEM results provide more relevant diagnostic information than traditional coagulation tests, neither technology is capable of being applied to the field where need is greatest. Diagnostic tests are critical for rapid evaluation of hemostasis-related parameters, especially in events of trauma, and thus should be near the scene of

trauma, prior to and during patient movement. TEG and ROTEM instruments can be accessible near the point of care in a hospital, but must be leveled on a firm table for accurate measurement, and thus are incapable of becoming true point-of-care (POC) devices.

This need for a quantitative POC technology can be addressed by creating a handheld device consisting of a core-shell biomimetic cilia array onto which a drop of whole blood may be deposited. Such an array with rods 2 μm in diameter and 25 μm tall can be fabricated to any specificied area, limited at the lower end to 0.5 mm and at the higher end by the size of the polycarbonate track-etched template and electrodeposition system used in the fabrication process (described in Chapter 4). This handheld device would consist of an array of core-shell rods situated within a well, a small magnetics system to drive the rods, an LED for light transmission through the array, a photodiode for light and rod amplitude detection, and an input port for the addition of whole blood. Figure 7.6 is a schematic of the potential handheld device. Measurements of coagulation times have been taken with core-shell arrays utilizing the standard magnetic set-up described in Section 5.2.1 and employing a planar beat shape. These measurements are discussed in the following section.

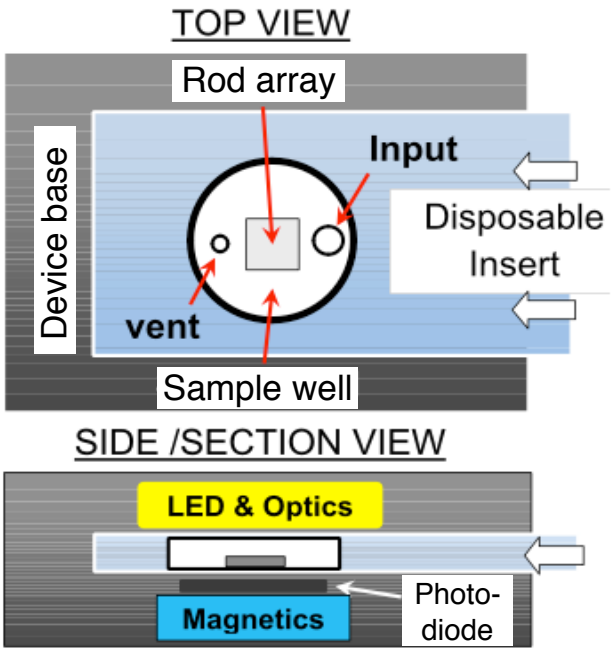

Figure 7.6: A low-cost disposable test strip containing the core-shell rod array and input port for whole blood. The handheld base into which the strip is inserted would not be disposable and would contain an LED, photodiode, and magnetics system.

7.3 Measuring clotting times with core-shell cilia

For testing, citrated animal plasmas were obtained from Haemoscope, a company which manufactures the TEG Hemostasis System discussed in the previous section. The animal plasmas, Level 1 and Level 2 (Lot # 070-0901 and 0930-0802, respectively), are standardized control samples routinely used for TEG calibration testing. A citrated plasma is one that has lost its ability to clot on its own; much, if not all, of the calcium, which plays a part in the clotting cascade, has been chelated by sodium citrate. To release it and restore clotting abilities, calcium chloride ($CaCl_2$) is added to the citrated plasma, binding the citrate and increasing calcium levels (Walser, 1961). The two different levels of plasma represent two different clotting abilities. Level 1 plasma is considered a normal plasma, such that

the clotting time and strength is consistent with that of a normal plasma sample. Level 2 plasma is considered abnormal, such that the onset of clotting time is prolonged and the clotting strength is less than that of normal plasma.

Before any clotting can occur on a core-shell array, the array is prepared as described in the Materials and Fabrication chapter by Figure 4.13. The core-shell rods utilized here are much larger (2 μm diameter by 25 μm long) than the core-shell rods used as biomimetic cilia (0.5 μm diameter by 10 μm long), though the aspect ratio is similar. For this application, rods are larger in order to both detect small changes in amplitude through the clot's slight opacity and utilize a 10x or 20x microscope objective to obtain amplitudes over a wider field of view.

After the last step in the fabrication process – dissolution of the polycarbonate template with dichloromethane (Figure 4.13E) – the array is rinsed with ethanol, deionized water, and finally PBS. Approximately 8-10 μL of PBS remains to cover the array, keeping it wet and preventing rod collapse. The array is placed onto a heated microscope stage (Bioscience Tools, model TC-E50x30) and warmed to approximately 37°C, the optimal temperature for clotting. Similar to the set-up we use to achieve the tilted conical beat pattern, a permanent neodymium magnet (K&J Magnetics, cat. no. BX084-N52) is affixed to a rotating motor, such that the edge of the magnet passes over the core-shell array. The magnetic field is approximately 45 mT, applying enough torque on the rods to detect changes in the rod amplitude with a 10x microscope objective. If the magnetic field is too strong, the longer core-shell rods will bend such that they become physically near enough to be attracted to one another. This attraction does not occur only at magnetic saturation, but can

become evident around fields of 80 mT or greater. Such contact should be avoided to maintain that the change in rod amplitude is due only to the changing environment around the rods. Figure 7.7 shows brightfield images of an array with Level 1 plasma when the rods are upright and when they are tilted due to the applied magnetic field. Less light intensity is detected by the camera when the array is tilted, as the nickel portion of the rod blocks the light.

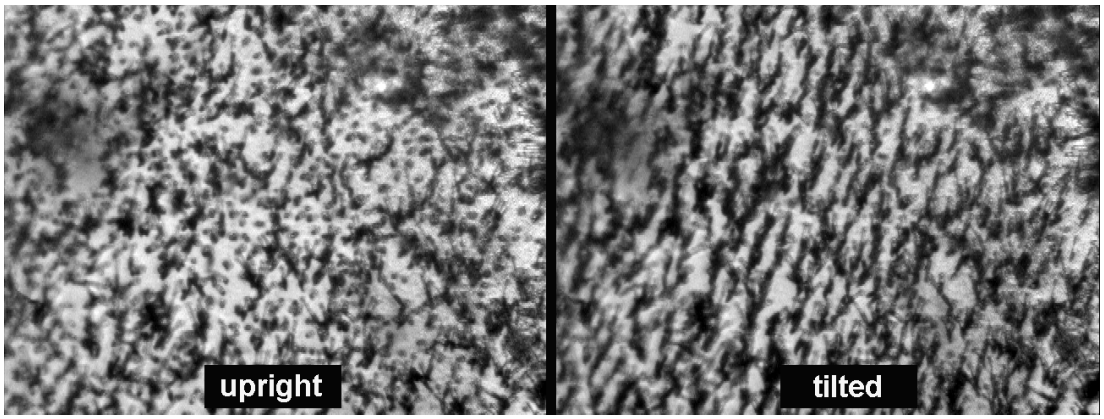

Figure 7.7: Brightfield images show the arrays ability to change the brightness of a frame by tilting in response to an applied magnetic field such that the nickel tube portion of the rod blocks transmitted light. The modulation of intensity is due to this period motion of the rods.

Data presented here are from three experiments with three different core-shell arrays. Once a clot has been formed over an array, the array is no longer usable for other experiments as it is impossible to remove the formed clot. For the three arrays, two Level 1 plasmas and one Level 2 plasma were used to illustrate reproducibility and sensitivity in the measurement of clotting times.

Before adding Level 1 and Level 2 plasmas to a core-shell array, $CaCl_2$ (8 μL) is added to the 8-10 μL PBS previously covering the array. The appropriate plasma (68 μL) follows

and is mixed gently by pipetting with the $CaCl_2$. Immediately after plasma addition, core-shell rods are driven at a frequency of 2 Hz, and video data of their motion is captured at 30 frames per second for at least thirty minutes using a Pulnix camera, model TM-6710CL (JAI, Inc.). To process these videos, I use open source software ImageJ and measure the average light intensity of each frame, producing the raw data shown in Figure 7.8, which has been normalized to unity.

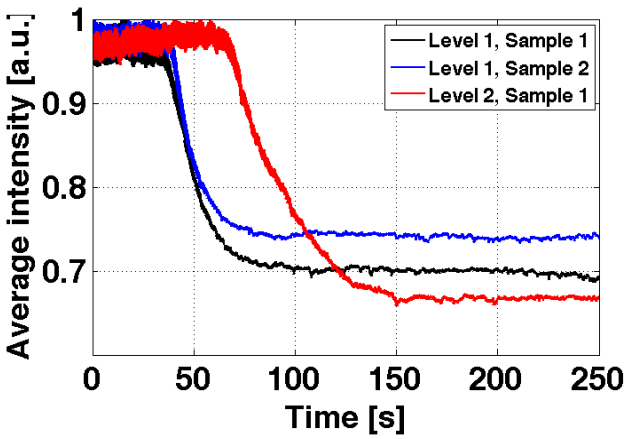

Figure 7.8: Average intensity versus time data indicate the time to the onset of clotting for two Level 1 (black, blue curves) and one Level 2 (red curve) plasma samples added to core-shell rod arrays. Level 2 plasma begins clotting approximately 30 seconds after both Level 1 plasmas. Time zero for the black and blue Level 1 curves is 13 s and 15 s, respectively, prior to the start of the video. For the red Level 2 curve, time zero is 25 s prior to the start of the video.

Due to the time delay between adding the plasma to the core-shell arrays and starting the video capture, the time prior to time zero varies for each clot from 13-25 seconds. Note that the time at which clotting commences is similar for the two Level 1 plasma samples and prolonged for the Level 2 plasma sample by at least 30 s. From the raw data shown in Figure 7.8, we observe intensity changes in two different ways: (i) a decrease in rod amplitude as the clot forms provides a mechanical measurement of coagulation, and (ii) a decrease in

global intensity as the clot forms provides a light scattering (turbidity) measurement of coagulation. The global change in intensity is reminiscent of a traditional clotting time measurement called turbidity, which utilizes the amount of scattered and absorbed light as measured by a spectrophotometer to define the onset of clot polymerization (Gabriel et al., 1992). We can write the average transmitted intensity detected by the camera as

$$I_{avg}(t) = A(t)T(t) \tag{7.2}$$

where $A(t)$ is the transmitted light intensity due to the rod motion and $T(t)$ is the transmitted light intensity due to the scattering and absorption by the clot itself. We can further write the rod modulated intensity as a function of the intensity A_0 when rods are upright, blocking minimal light, and the intensity A_m when rods are tilted at some angle θ, blocking maximum light,

$$I_{avg}(t) = [A_0 + A_m sin(\theta(t))]\, T(t). \tag{7.3}$$

The two different measures of clot formation can be separated by utilizing a moving average to determine the global intensity change, and as light intensities are multiplicative, dividing by this average to obtain the amplitude change as a function of time. Figure 7.9 illustrates how the raw data is separated into the two types of measurements (mechanical and light scattering) for Level 1 and Level 2 clotting data. The mechanical amplitude measurement appears to be more sensitive to the onset of clotting than the turbidity measurement as the rod amplitude begins to decrease at least ten seconds before the turbidity

measurement indicates a global decrease in intensity. Typical turbidity measurements are performed with large sample volumes on highly expensive and accurate spectrophotometers (Wolberg et al., 2002). Core-shell cilia arrays provide an accurate and inexpensive way to analyze clot structure which is shown to be more sensitive to the onset of fibrin formation than a measure of change in intensity.

In addition to higher sensitivity to clot formation than turbidity measurements, core-shell arrays can provide at the minimum a qualitative measure of clot structure similar to that provided by turbidity and TEG. From the change in turbidity as a function of wavelength, the mass-length ratio μ, mass per unit length of fibrin fibers which form a clot, can be obtained (Carr and Hermans, 1978). This mass-length ratio is an important parameter in the characterization of clot structure as it may be used to monitor fibrin diameter and mass density changes, both of which alter clot structure (Gabriel et al., 1992). Changes in the fibrin mass-length ratio (and therefore clot structure) can occur with disease or drug treatments and are thus clinically of interest. Turbidity can detect the effect of increased thrombin levels by measuring a decreased mass-length ratio (Gabriel et al., 1992). Analogously in TEG, a decreased mass-length ratio and increased thrombin concentration may be determined by the alpha angle, which measures the rapidity of fibrin build up. A larger alpha angle typically corresponds to higher levels of the fibrin monomer fibrinogen (shown as a TEG tracing in Figure 7.5B) (Johansson et al., 2009), which may be the result of an increased thrombin concentration and smaller mass-length ratio. This alpha angle may be measured with a core-shell array as I discuss below.

Comparing this mechanical measurement which stems from the post amplitude to the

TEG tracing in Figure 7.4, we see the R time (the time to initial clot formation indicated in the TEG tracing by a sudden widening of the curve is indicated in our mechanical measurement by a sudden narrowing of the curve. This narrowing occurs after a longer time frame in the Level 2 sample, as this control sample is representative of a hypocoagulable sample (as shown by the TEG tracing in Figure 7.5C).

With TEG measurements, the time for a clot to reach its maximum strength, or maximum amplitude, is called TMA, time to maximum amplitude; this time is indicated on the tracing in Figure 7.4 by the time for the curve to reach its widest point. With the mechanical post measurements, TMA is analogous to the time for the curve to reach its narrowest point, which I could label as the time to minimum amplitude. At this point, the clot is considered fully formed and the amplitude of a core-shell rod is highly restricted by its surroundings.

The K time illustrated on the TEG tracing is the time for a clot to reach a specified strength, which is also the time for the pin in the TEG set-up to reach a given amplitude. This specified amplitude is another method for the comparison of blood clot kinetics across multiple samples. In the future we may or may not choose to set an amplitude to monitor for the core-shell system, though the K time amplitude will be smaller than the time zero amplitude of the rods.

The final variable TEG utilizes to parametrize results is the alpha angle, measuring the rapidity of fibrin build up once clotting has initiated. The alpha angle is the slope of the line connecting the R and K times (Johansson et al., 2009). With our data in Figure 7.9, a measurement of the angle at which the amplitude decreases, beginning at initial clot formation, would give us information similar to that obtained by the TEG tracing.

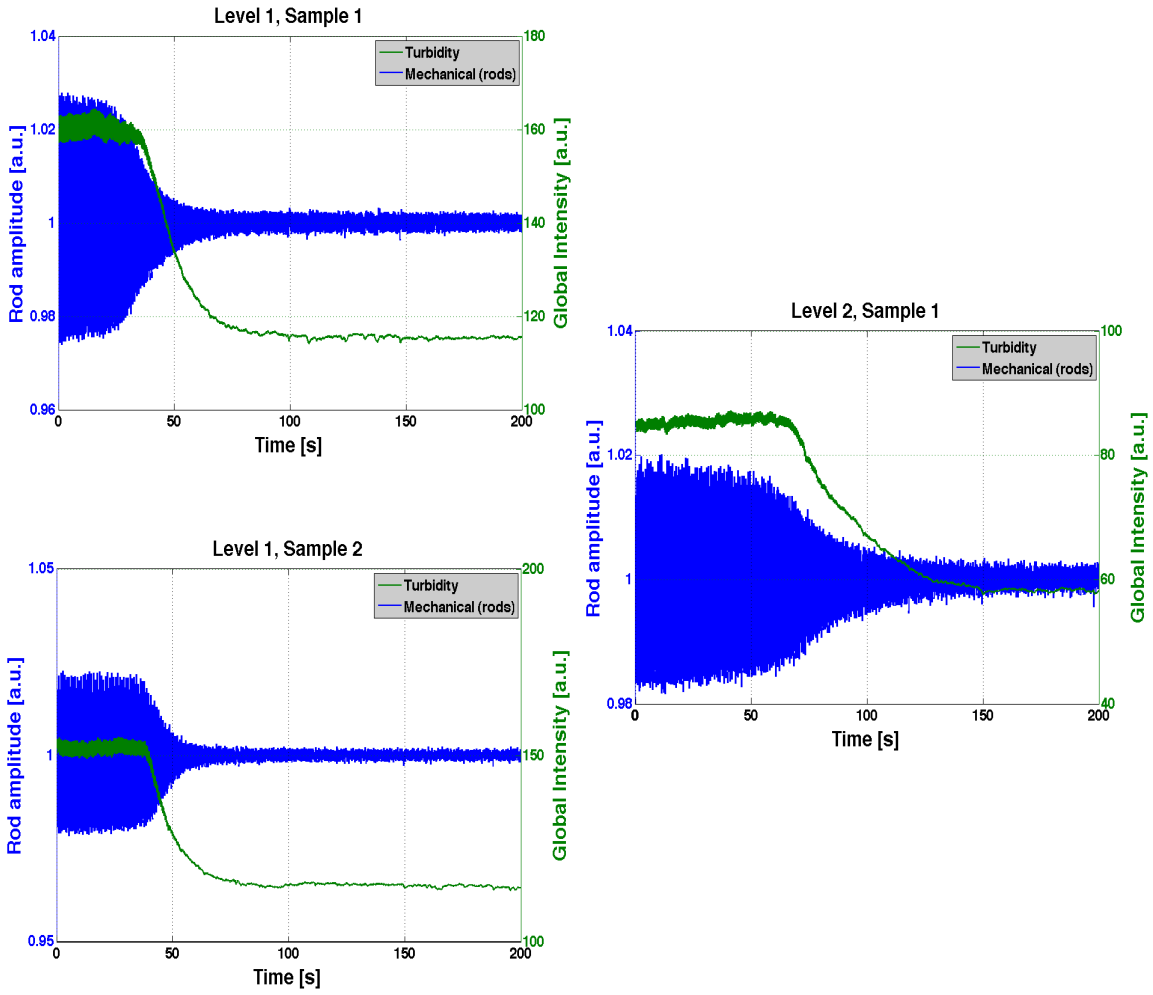

Figure 7.9: Intensity due to rod amplitude and turbidity (light scattering) versus time during clot formation. The left axes apply to the blue curves, which show rod amplitude versus time measured in arbitrary units, and the right axes apply to the green curves, which are similar to a turbidity measurement, or how the global intensity changes over time due to light scattering and absorption.

The approximate onset of clotting times (R times) indicated by the two different intensity measurements (adjusted for the time zero offsets mentioned previously) and those indicated by Haemoscope, the company from which the Level 1 and Level 2 control plasmas were obtained, are listed in Table 7.1. The range of the onset of clotting times are provided by Haemoscope readily. However, in order to compare all parameters gathered

with my measurement system to TEG data, I would need to utilize a pin-and-cup TEG system to collect such data for the same plasma levels.

Table 7.1: Onset of plasma clotting times

	Haemoscope (TEG)	Amplitude (core-shell arrays)	Turbidity (core-shell arrays)
Level 1, Sample 1	0–180 s	39 s	49 s
Level 1, Sample 2	0–180 s	42 s	54 s
Level 2, Sample 1	60–180 s	80 s	91 s

Note that the long time mechanical measurement of coagulation remains well above noise, as shown in Figure 7.10, and that the drive frequency can still be extracted from the intensity as measured by the rod amplitude.

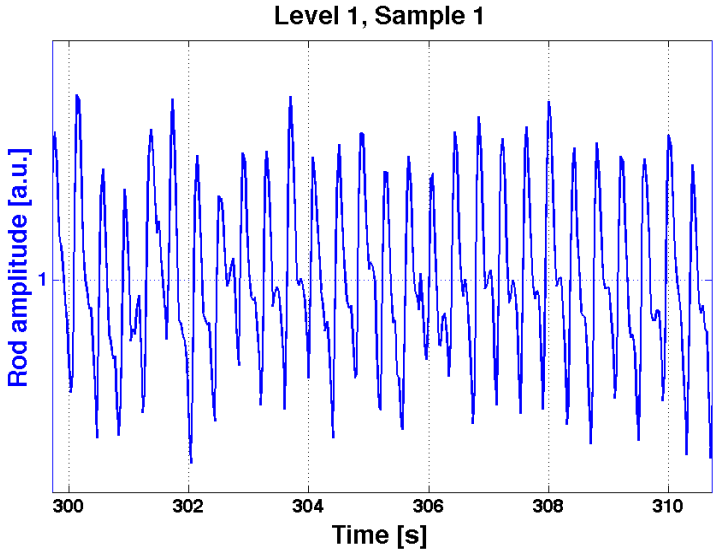

Figure 7.10: After full formation of the Level 1 plasma clot, the drive frequency of the core-shell rods can still be detected from the intensity as modulated by the mechanical change in amplitude.

Core-shell cilia have also been used to successfully measure the clot formation within whole blood. Figure 7.11 shows the change in amplitude as a function of time for a whole

blood sample. Future experiments should improve on imaging techniques, as obtaining a brightfield image of the core-shell cilia through red blood cells is difficult, and to obtain such an image, the sample thickness must be less than ~0.5 mm and the sample volume less than ~10 μL.

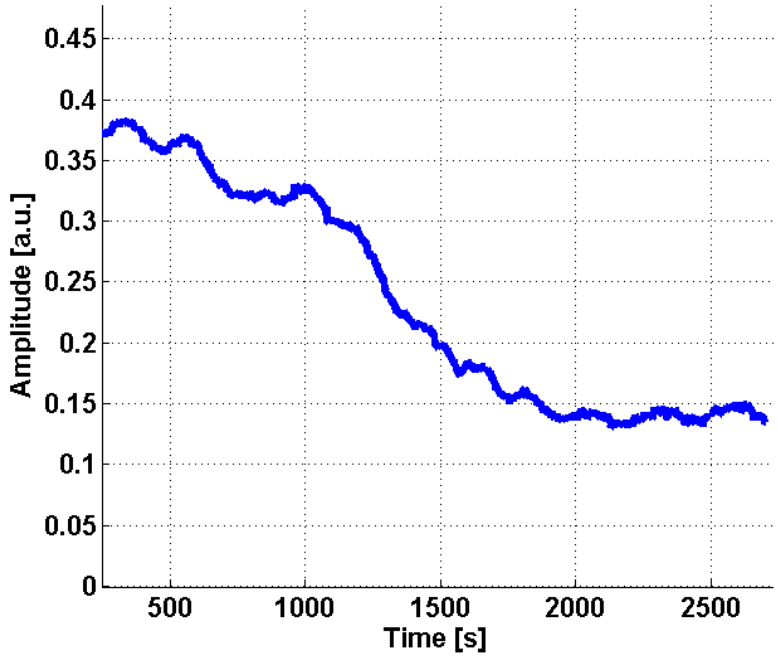

Figure 7.11: The change in amplitude of core-shell cilia during the formation of a clot in whole blood. The decrease in amplitude may be due to an increase in local viscosity or an increase in elasticity, both of which I see in Section 6.3.4 with varying agarose concentrations.

7.4 Future work

Before core-shell cilia can become a robust and reliable method for the measurement of clot formation and lysis, more work on both the determination of viscoelastic parameters from amplitude and phase measurements and the normalization of measurements across

multiple core-shell arrays must be performed. Currently, normalizing all core-shell arrays such that each array responds identically has not been done. The applied magnetic field for each array is different, typically because the magnet setup is broken down and removed from the microscope between experiments. Evaluating whether the response of individual arrays is identical with an identically applied magnetic field is an important step to take in the characterization of these arrays as POC devices capable of measuring absolute viscoelastic parameters. Without a guarantee that this is so, quantitatively accurate measurements of clotting strengths are not attainable, though the ability to measure clotting times remains unaffected. The relationship between the amplitude data and Equation 7.3 should be further explored. The variation in tilt angle θ across different blood samples for a constant applied magnetic field could become an important variable in understanding the contributions of viscosity and elasticity. If normalization across all core-shell arrays is not an option, though I think it will be, the difference in initial tilt angles (θ) could serve as a calibration method such that quantitative values could be obtained across different arrays.

Additionally, it would be beneficial to incorporate the measurement of phase in experiments to understand in greater detail the ultimate strength of a blood clot and the time evolution of the viscoelastic parameters of a clot, such as viscosity and elasticity. TEG measurements utilize the amplitude A of the cup to determine the strength of a clot by defining the shear elastic modulus as

$$G = \frac{\left(\frac{5000 \times A}{100 - A}\right)}{1000} \tag{7.4}$$

in units of dynes/cm^2. A TEG cup with a normal blood sample typically has an amplitude

of 50 mm, for which G = 500 Pa. This equation is not a quantitative measure of elasticity, but is qualitative, utilizing a normal sample as a standard. A smaller amplitude may be the result of hypocoagulability, or the lack of blood clotting capability (see Figure 7.5C). The shear modulus of pure plasma was measured by Shih et al. in 2010 as approximately 585±127 Pa. Humans typically have a concentration of 40% red blood cells; this increase in red blood cells decreases the shear modulus by a factor of three, to 168±26 Pa (Shih et al., 2010).

Before viscosity and elasticity can be found for plasma or whole blood, it is important to gain a deeper understanding of the effects on core-shell cilia amplitude of a changing viscosity or elasticity within purely viscous and viscoelastic fluids. To achieve this understanding in purely viscous fluids, the amplitude of core-shell cilia should be evaluated in a wider variety of fluid viscosities. The model discussed in Section 7.1 is sufficient for understanding the qualitative effect of viscosity on core-shell cilia, but overestimates fluid viscosity of buffer by a factor of ten, indicating either that cilia are more damped and the model requires an additional term to account for this extra damping or that the cilium amplitude is not sufficiently visualized with 120 frames per second video capture. The second possibility can be explored by utilizing a camera with a frame rate greater than 200 frames per second to decrease the time between frames to less than 5 ms. The first possibility could be determined by evaluating whether or not PDMS rods exhibit internal damping or the sample floor (less than 10 μm from the cilium tip) affects the motion of the cilium tip. Cilia amplitude in fluids of differing viscoelasticities was discussed in Section 6.3, but this understanding is not yet robust and does not translate to data obtained in clotting blood or

plasma, neither of which are homogeneous fluids in the linear regime. Nonlinear rheological behavior as measured by a given probe cannot be used to predict the response of the fluid to a second probe such as core-shell cilia (Macosko, 1994); thus, an average of plasma and whole blood response to core-shell cilia of a specific size and shear rate over a number of experiments should be determined before an analytical relationship between amplitude and clot viscoelasticity (or clot strength) can be formulated. Additionally, a sinusoidal driving force should be utilized to extract in-phase and out of phase actuator response as in future experiments, depending on whether or not the mechanism causing amplitude reduction is an increased local viscosity or an increased elasticity, a portion of the actuator's response will be in-phase with the driving force. The in-phase response will correlate with the storage modulus of the clot; an increase in stiffness is often associated with an increase in fiber thickness (Collet et al., 2005). Utilizing core-shell cilia as a microscale probe may provide us with an understanding of the microscale properties of blood clot and how those properties affect clot formation.

Appendix A

Blood coagulation

Coagulation is the formation of blood clots, which stem the flow of blood from damaged blood vessels. Coagulation ultimately forms fibrin strands that bundle together and form networks to block blood flow. At least twenty different clotting proteins work together to create these fibrin networks, some as zymogens which are precursors of inactive proteolytic enzymes and some as cofactors that accelerate reactions. A number of them are listed in Table A.1 in Appendix A, in the order of their appearance in the coagulation process (Jesty, 2008). Two highly important proteins are tissue factor and thrombomodulin, which are responsible for the initiation and shut down of the entire clotting process.

Table A.1: Coagulation factors and cofactors (Jesty, 2008)

Common name	Alternate names	Function
Tissue factor (TF)	Thromboplastin Factor III	initiator; with factor VIIa, activates factors IX and X
Factor XII	Hageman factor	protease zymogen
Factor XI	Plasma thromboplastin antecedent	protease zymogen
Factor X	Stuart-Prower factor	protease zymogen
Factor IX	Christmas factor	protease zymogen
Factor VIII	Antihemophilic factor	with factor IXa, activates factor X
Factor VII	Proaccelerin	activates factors IX and X
Factor V	Labile factor	with factor Xa, activates prothrombin
Prothrombin	Factor II	protease zymogen
Fibrinogen	Factor I	clot formation, fibrin precursor
Factor XIII	Fibrin-stabilizing factor	zymogen of transglutaminase
Thrombomodulin		with thrombin, activates protein C
Protein C		protease zymogen
Protein S		with protein C, activates factors Va and VIIIa
Antithrombin III	Antithrombin Heparin cofactor	protease inhibitor
Tissue factor pathway inhibitor	Extrinsic pathway inhibitor	protease inhibitor

Injury to a blood vessel's inner lining, or endothelium, exposes the protein von Willebrand factor which is responsible for recruiting collagen and other coagulation factors. Additionally, platelets aggregate at the site of injury and are activated, releasing a number of platelet factors, factor Va, and ADP. (Lowercase *a* indicates the active form.) The presence of these factors activates other platelets, serving to increase calcium levels, a higher concentration of which activates protein kinase C. Phospholipase A_2 is activated by protein kinase C and in turn increases the binding affinity of membrane glycoproteins IIb and IIIa to fibrinogen. This phase is known as primary hemostasis.

In the phase of secondary hemostasis the coagulation cascade occurs, of which there are two potential pathways called the intrinsic and extrinsic pathways. The intrinsic pathway is also known as the contact activation pathway and is the pathway responsible for blood or plasma's ability to clot when contacting a surface. The main factors involved include XII, prekallikrein, and high molecular weight kininogen. These generate factor XIIa which activates factor XI. Factor XIa activates factor IX, and with factor VIIIa, factor X is activated. The clotting pathway follows the final common pathway (starting with factor X), which is shared by the extrinsic pathway.

The extrinsic pathway is also called the tissue factor (TF) pathway, and is the primary and "normal" pathway for blood coagulation initiation. TF is a protein in the tissue beneath the endothelium, and following injury, TF comes into contact with proteins present in the plasma including factor VII. TF and factor VII form a complex (TF:VII) which is catalyzed by factor Xa in a positive feedback reaction. Complex TF:VIIa then activates factors IX and X into IXa and Xa. Factors Va, which comes primarily from platelets, and Xa also form a complex called the prothrombinase complex and are responsible for activating prothrombin to thrombin. Thrombin is responsible for both the activation of platelets and factor XIII and conversion of fibrinogen to fibrin. The final step in the coagulation cascade is the crosslinking of fibrin which occurs by factor XIIIa.

If certain factors are deficient or defective, the coagulation cascade will be disrupted and coagulopathies, which are clotting or bleeding disorders, can occur. Clotting may occur too slowly as in hypocoagulability where a possible end result, if untreated, is an increased bleeding or hemorrhaging, or too quickly as in hypercoagulability where the

result, if untreated, is an increased risk of developing blood clots, also known as thrombosis. A deficiency or defect in factors VIII or IX, which are responsible for crosslinking fibrin and activating factor X, respectively, may cause hemophilia in patients. If a variant of factor V, called factor V Leiden, is present in place of factor V, then factor Va will never be inactivated, and a patient will be at a much higher risk for thrombosis.

Bibliography

Afzelius, B. (2004). Cilia-related diseases. *The Journal of Pathology*, 204(4):470–477.

Ahmed, S. and Jones, F. (1990). A review of particulate reinforcement theories for polymer composites. *Journal of materials science*, 25(12):4933–4942.

Albensoeder, S., Kuhlmann, H., and Rath, H. (2001). Three-dimensional centrifugal-flow instabilities in the lid-driven-cavity problem. *Physics of fluids*, 13:121.

Andersson, H., van der Wijingaart, W., Nilsson, P., Enoksson, P., and Stemme, G. (2011). A valve-less diffuser micropump for microfluidic analytical systems. *Sensors and Actuators B: Chemical*, 72(3):259–265.

Artale, V., Boffetta, G., Celani, A., Cencini, M., and Vulpiani, A. (1997). Dispersion of passive tracers in closed basins: Beyond the diffusion coefficient. *Physics of Fluids*, 9:3162.

Babiano, A., Basdevant, C., and LE, R. (1990). Relative dispersion in two-dimensional turbulence. *Journal of Fluid Mechanics*, 214:535–557.

Barnes, H. (2000). *A Handbook of Elementary Rheology*. The Univerisyt of Wales Institute of Non-Newtonian Fluid Mechanics.

Barsi, L., Buki, A., Szabo, D., and Zrinyi, M. (1996). Gels with magnetic properties. In *Progress in Colloid and Polymer Science*, volume 102, pages 57–63. Springer, Berlin.

Bhushan, B. (2009). Biomimetics: lessons from nature–an overview. *Philosophical Transactions of the Royal Society A: Mathematical, Physical and Engineering Sciences*, 367(1893):1445.

Boucher, R. (2004). New concepts of the pathogenesis of cystic fibrosis lung disease. *European Respiratory Journal*, 23(1):146.

Brohi, K., Cohen, M., and Davenport, R. (2007). Acute coagulopathy of trauma: mechanism, identification and effect. *Current opinion in critical care*, 13(6):680.

Brücker, C., Bauer, D., and Chaves, H. (2007). Dynamic response of micro-pillar sensors measuring fluctuating wall-shear-stress. *Exp Fluids*, 42(5):737–749.

Bye, J. (1966). Numerical solutions of the steady-state vorticity equation in rectangular basins. *J. Fluid Mech*, 26(part 3):577–598.

Cao, H., Tie, C., Xu, Z., Hong, J., and Sang, H. (2001). Array of nickel nanowires enveloped in polyaniline nanotubules and its magnetic behavior. *Applied Physics Letters*, 78:1592.

Carr, M. and Hermans, J. (1978). Size and density of fibrin fibers from turbidity. *Macromolecules*, 11(1):46–50.

Cartwright, J., Piro, N., Piro, O., and Tuval, I. (2007). Embryonic nodal flow and the dynamics of nodal vesicular parcels. *Journal of The Royal Society Interface*, 4(12):49.

Caykara, T., Yoruk, D., and Demirci, S. (2009). Preparation and chracterization of poly(n-tertbutylacrylamide-co-acrylamide) ferrogel. *Journal of Applied Polymer Science*, 112(2):800–804.

Cebers, A. (2005). Flexible magnetic filaments. *Current opinion in colloid & interface science*, 10(3-4):167–175.

Chilvers, M. and O'Callaghan, C. (2000). Analysis of ciliary beat pattern and beat frequency using digital high speed imaging: comparison with the photomultiplier and photodiode methods. *Thorax*, 55(4):314.

Christopher, G., Yoo, J., Dagalakis, N., Hudson, S., and Migler, K. (2010). Development of a mems based dynamic rheometer. *Lab Chip*, 10(20):2749–2757.

Collet, J., Shuman, H., Ledger, R., Lee, S., and Weisel, J. (2005). The elasticity of an individual fibrin fiber in a clot. *Proceedings of the National Academy of Sciences of the United States of America*, 102(26):9133.

Collin, D., Auernhammer, G., Gavat, O., Martinoty, P., and Brand, H. (2003). Frozen-in magnetic order in uniaxial magnetic gels: Preparation and physical properties. *Macromolecular Rapid Communications*, 24(12):737–741.

Cordente, N., Respaud, M., Senocq, F., Casanove, M., Amiens, C., and Chaudret, B. (2001). Synthesis and magnetic properties of nickel nanorods. *Nano Letters*, 1(10):565–568.

Cornell, R. and Schwertmann, U. (2003). *The iron oxides: structure, properties, reactions, occurrences, and uses*. Wiley-VCH.

Cribb, J. (2010). *Driven and Thermal Microparticle Rheology of Complex Biopolymer Systems*. PhD thesis, University of North Carolina at Chapel Hill.

den Toonder, J., Bos, F., Broer, D., Filippini, L., Gillies, M., de Goede, J., Mol, T., Reijme, M., Talen, W., and Wilderbeek, H. (2008). Artificial cilia for active micro-fluidic mixing. *Lab Chip*, 8(4):533–541.

Encinas-Oropesa, A., Demand, M., Piraux, L., Ebels, U., and Huynen, I. (2001). Effect of dipolar interactions on the ferromagnetic resonance properties in arrays of magnetic nanowires. *Journal of Applied Physics*, 89(11):6704–6706.

Evans, B., Fiser, B., Prins, W., Rapp, D., Shields, A., Glass, D., and Superfine, R. (2012). A highly tunable silicone-based magnetic elastomer with nanoscale homogeneity. *Journal of Magnetism and Magnetic Materials*, 324(4):501–507.

Evans, B., Shields, A., Carroll, R., Washburn, S., Falvo, M., and Superfine, R. (2007a). Magnetically actuated nanorod arrays as biomimetic cilia. *Nano Lett*, 7(5):1428–1434.

Evans, B. A. (2008). *Design, Fabrication, and Actuation of Biomimetic Cilia*. PhD thesis, University of North Carolina at Chapel Hill.

Evans, B. A. and Superfine, R. (2011). *Biomimetic Based Applications*, chapter 17. Intech, Rijeka, Croatia.

Evans, P., Hendren, W., Atkinson, R., and Pollard, R. (2007b). Nickel-coated gold-core nanorods produced by template assisted electrodeposition. *Journal of the Electrochemical Society*, 154:K79.

Fahrni, F., Prins, M., and van IJzendoorn, L. (2009a). Magnetization and actuation of polymeric microstructures with magnetic nanoparticles for application in microfluidics. *Journal of Magnetism and Magnetic Materials*, 321(12):1843–1850.

Fahrni, F., Prins, M. W. J., and Ijzendoorn, L. J. V. (2009b). Micro-fluidic actuation using magnetic artificial cilia. *Lab Chip*, 9(23):3413–3421.

Fauci, L. and Dillon, R. (2006). Biofluidmechanics of reproduction. *Annual review of fluid mechanics*, 38:371–394.

Ferre, R., Ounadjela, K., George, J., Piraux, L., and Dubois, S. (1997). Magnetization processes in nickel and cobalt electrodeposited nanowires. *Physical Review B*, 56(21):14066–14075.

Fiser, B., Shields, A., Falvo, M., and Superfine, R. (2012). Highly responsive core-shell microactuator arrays as biomimetic cilia. [in preparation].

Francois, N., Allo, S., Jacobo, S., and Daraio, M. (2007). Composites of polymeric gels and magnetic nanoparticles: Preparation and drug release behavior. *Journal of Applied Polymer Science*, 105(2):647–655.

Fuhrer, R., Athanassiou, E., Luechinger, N., and Stark, W. (2009). Crosslinking metal nanoparticles into the polymer backbone of hydrogels enables preparation of soft, magnetic fielddriven actuators with musclelike flexibility. *Small*, 5(3):383–388.

Furst, E., Suzuki, C., Fermigier, M., and Gast, A. (1998). Permanently linked monodisperse paramagnetic chains. *Langmuir*, 14(26):7334–7336.

Gabriel, D., Muga, K., and Boothroyd, E. (1992). J. biol. chem.-1992-gabriel-24259-63. *The Journal of Biological Chemistry*, 267(34):24259–24263.

Galicia, J., Sandre, O., Cousin, F., Guemghar, D., Menager, C., and Cabuil, V. (2003). Designing magnetic composite materials using aqueous magnetic fluids. *Journal of Physics-Condensed Matter*, 15(15):S1379–S1402.

Gere, J. and Timoshenko, S. (1990). *Mechanics of Materials*. PWS Publishing Company, 3rd edition.

Goodwin, J. and Hughes, R. (2008). *Rheology for Chemists, An Introduction*. The Royal Society of Chemistry, 2 edition.

Guild, F. and Young, R. (1989). A predictive model for particulate-filled composite materials. *Journal of materials science*, 24(1):298–306.

Hess, J., Brohi, K., Dutton, R., Hauser, C., Holcomb, J., Kluger, Y., Mackway-Jones, K., Parr, M., Rizoli, S., and Yukioka, T. (2008). The coagulopathy of trauma: a review of mechanisms. *The Journal of trauma*, 65(4):748.

Hill, D., Swaminathan, V., Estes, A., Cribb, J., O'Brien, E., Davis, C., and Superfine, R. (2010). Force generation and dynamics of individual cilia under external loading. *Biophysical journal*, 98(1):57.

Hirokawa, N., Okada, Y., and Tanaka, Y. (2009). Fluid dynamic mechanism responsible for breaking the left-right symmetry of the human body: The nodal flow. *Annu. Rev. Fluid Mech.*, 41:53–72.

Hirokawa, N., Tanaka, Y., Okada, Y., and Takeda, S. (2006). Nodal flow and the generation of left-right asymmetry. *Cell*, 125(1):33–45.

Howard, J. (2001). *Mechanics of Motor Proteins and the Cytoskeleton*. Sinauer Associates, Inc.

Jackson, J. D. (1998). *Classical Electrodynamics*. Wiley, 3rd edition.

Jesty, J. (2008). Blood coagulation.

Johansson, P., Stissing, T., Bochsen, L., and Ostrowski, S. (2009). Thrombelastography and tromboelastometry in assessing coagulopathy in trauma. *Scand J Trauma Resusc Emerg Med*, 17(1):1–8.

Judy, J., Muller, R., and Zappe, H. (1995). Magnetic microactuation of polysilicon flexure structures. *Microelectromechanical Systems, Journal of*, 4(4):162–169.

Khatavkar, V., Anderson, P., den Toonder, J., and Meijer, H. (2007). Active micromixer based on artificial cilia. *Physics of fluids*, 19:083605.

Khoo, M. and Liu, C. (2001). Micro magnetic silicone elastomer membrane actuator. *Sensors and Actuators A: Physical*, 89(3):259–266.

Kim, Y., Ahn, H., Nam, S., Lee, S., Shim, H., and Kim, W. (2008). Honeycomb pattern array of vertically standing core-shell nanorods: Its application to li energy electrodes. *Applied Physics Letters*, 93:103104.

King, M., Gilboa, A., Meyer, F., and Silberberg, A. (1974). On the transport of mucus and its rheologic simulants in ciliated systems. *The American review of respiratory disease*, 110(6):740.

Kisker, H., Gessmann, T., Wurschum, R., Kronmuller, H., and Schaefer, H. (1995). Magnetic properties of high purity nanocrystalline nickel. *NanoStructured Materials*, 6(5-8):925–928.

Kryszewski, M. and Jeszka, J. (1998). Nanostructured conducting polymer composites - superparamagnetic particles in conducting polymers. *Synthetic Metals*, 94:99–104.

Kudo, H., Sawada, T., Kazawa, E., Yoshida, H., Iwasaki, Y., and Mitsubayashi, K. (2006). A flexible and wearable glucose sensor based on functional polymers with soft-mems techniques. *Biosensors and Bioelectronics*, 22(4):558–562.

Kumar, S. and Chakarvarti, S. (2004). Sem morphology and xrd characterization of ni microstructure arrays synthesized by dc electrodeposition in porous polycarbonate templates. *Journal of Materials Science*, 39(9):3249–3251.

LaCasce, J. and Bower, A. (2000). Relative dispersion in the subsurface north atlantic. *Journal of marine research*, 58:863–894.

Lahav, M., Weiss, E., Xu, Q., and Whitesides, G. (2006). Core-shell and segmented polymer-metal composite nanostructures. *Nano Lett.*, 6(9):2166–2171.

Lefort, J. (1852). Memoire sur les oxydes ferroso-ferriques et leurs combinasions. *Comptes Rendus de l'Academie des Sciences*, 34:488–491.

Li, L., Yang, Y., Li, G., and Zhang, L. (2006). Conversion of a bi nanowire array to an array of bi–bi2o3 core–shell nanowires and bi2o3 nanotubes. *Small*, 2(4):548–553.

Lin, H., Watanabe, Y., Kimura, M., Hanabusa, K., and Shirai, H. (2003). Preparation of magnetic poly(vinyl alcohol) (pva) materials by in situ synthesis of magnetite in a pva matrix. *Journal of Applied Polymer Science*, 87(8):1239–1247.

Liu, A., Bornside, D., Armstrong, R., and Brown, R. (1998). Viscoelastic flow of polymer solutions around a periodic, linear array of cylinders: comparisons of predictions for microstructure and flow fields. *Journal of Non-Newtonian Fluid Mechanics*, 77(3):153–190.

Liu, C. (1998). Development of surface micromachined magnetic actuators using electroplated permalloy. *Mechatronics*, 8(5):613–633.

Liu, M., Liu, X., Wang, J., Wei, Z., and Jiang, L. (2010). Electromagnetic synergetic actuators based on polypyrrole/fe 3 o 4 hybrid nanotube arrays. *Nano Research*, 3(9):670–675.

Liu, Z., Xia, G., Zhu, F., Kim, S., Markovic, N., Chien, C., and Searson, P. (2008). Exploiting finite size effects in a novel core/shell microstructure. *Journal of Applied Physics*, 103:064313.

Macosko, C. W. (1994). *Rheology Principles, Measurements, and Applications*. Wiley-VCH.

Mann, K. and Ziedins, K. (2005). *Textbook of Hemophilia*, chapter Overview of hemostasis. Blackwell Publishing.

Massart, R. (1981). Preparation of aqueous magnetic liquids in alkaline and acidic media. *IEEE Transactions on Magnetics*, 17(2):1247–1248.

Massart, R., Dubois, E., Cabuil, V., and Hasmonay, E. (1995). Preparation and properties of monodisperse magnetic fluids. *Journal of Magnetism and Magnetic Materials*, 149(1-2):1–5.

Mayer, C., Cabuil, V., Lalot, T., and Thouvenot, R. (2000). Magnetic nanoparticles trapped in ph 7 hydrogels as a tool to characterize the properties of the polymeric network. *Advanced Materials*, 12(6):417–420.

Metzner, A., White, J., and Denn, M. (1966). Constitutive equations for viscoelastic fluids for short deformation periods and for rapidly changing flows: significance of the deborah number. *AIChE Journal*, 12(5):863–866.

Mitran, S., Forest, M., Yao, L., Lindley, B., and Hill, D. (2009). Extensions of the ferry shear wave model for active linear and nonlinear microrheology. *Journal of non-Newtonian fluid mechanics*, 154(2-3):120–135.

Mitsumata, T., Ikeda, K., Gong, J., Osada, Y., Szabo, D., and Zrinyi, M. (1999). Magnetism and compressive modulus of magnetic fluid containing gels. *Journal of Applied Physics*, 85(12):8451–8455.

Mooney, M. (1951). The viscosity of a concentrated suspension of spherical particles. *Journal of Colloid Science*, 6(2):162–170.

Neugebauer, D., Neuwinger, J., Jockenhövel, F., and Nieschlag, E. (1990). '9+ 0' axoneme in spermatozoa and some nasal cilia of a patient with totally immotile spermatozoa associated with thickened sheath and short midpiece. *Human Reproduction*, 5(8):981.

Nghe, P., Terriac, E., Schneider, M., Li, Z., Cloitre, M., Abecassis, B., and Tabeling, P. (2011). Microfluidics and complex fluids. *Lab Chip*, 11(5):788–794.

Niles, S., McLaughlin, D., Perkins, J., Wade, C., Li, Y., Spinella, P., and Holcomb, J. (2008). Increased mortality associated with the early coagulopathy of trauma in combat casualties. *The Journal of trauma*, 64(6):1459.

Nonaka, S., Shiratori, H., Saijoh, Y., and Hamada, H. (2002). Determination of left–right patterning of the mouse embryo by artificial nodal flow. *Nature*, 418(6893):96–99.

Nonaka, S., Tanaka, Y., Okada, Y., Takeda, S., Harada, A., Kanai, Y., Kido, M., and Hirokawa, N. (1998). Randomization of left-right asymmetry due to loss of nodal cilia generating leftward flow of extraembryonic fluid in mice lacking kif3b motor protein. *Cell*, 95(6):829–837.

Oh, K., Chung, J., Devasia, S., and Riley, J. (2009). Bio-mimetic silicone cilia for microfluidic manipulation. *Lab Chip*, 9(11):1561–1566.

Oh, K., Smith, B., Devasia, S., Riley, J., and Chung, J. (2010). Characterization of mixing performance for bio-mimetic silicone cilia. *Microfluidics and Nanofluidics*, 9(4):645–655.

Okada, Y., Takeda, S., Tanaka, Y., Belmonte, J., and Hirokawa, N. (2005). Mechanism of nodal flow: a conserved symmetry breaking event in left-right axis determination. *Cell*, 121(4):633–644.

Olsson, R., Samir, M., Salazar-Alvarez, G., Belova, L., Ström, V., Berglund, L., Ikkala, O., Nogués, J., and Gedde, U. (2010). Making flexible magnetic aerogels and stiff magnetic nanopaper using cellulose nanofibrils as templates. *Nature Nanotechnology*, 5(8):584–588.

Pan, J., Wang, Q., and Snell, W. (2005). Cilium-generated signaling and cilia-related disorders. *Lab Invest*, 85(4):452–463.

Peng, X., Jin, J., and Ichinose, I. (2007). Mesoporous separation membranes of polymer-coated copper hydroxide nanostrands. *Adv. Funct. Mater.*, 17(11):1849–1855.

Pirmoradi, F., Cheng, L., and Chiao, M. (2010). A magnetic poly (dimethylesiloxane) composite membrane incorporated with uniformly dispersed, coated iron oxide nanoparticles. *Journal of Micromechanics and Microengineering*, 20:015032.

Pokroy, B., Epstein, A., Persson-Gulda, M., and Aizenberg, J. (2009). Fabrication of bioinspired actuated nanostructures with arbitrary geometry and stiffness. *Adv. Mater.*, 21(4):463–469.

Pol, V., Pol, S., and Gedanken, A. (2008). Core-shell nanorods of sns-c and snse-c: Synthesis and characterization. *Langmuir*, 24(9):5135–5139.

Purcell, E. (1977). Life at low reynolds number. *Am. J. Phys*, 45(3):11.

Resendiz-Hernandez, P., Rodriguez-Fernandez, O., and Garcia-Cerda, L. (2008). Synthesis of poly(vinyl alcohol)-magnetite ferrogel obtained by freezing-thawing technique. *Journal of Magnetism and Magnetic Materials*, 320(14):e373–e376.

Roca-Cusachs, P., Rico, F., Martinez, E., Toset, J., Farré, R., and Navajas, D. (2005). Stability of microfabricated high aspect ratio structures in poly (dimethylsiloxane). *Langmuir*, 21(12):5542–5548.

Sahu, B., Taylor, C., and Leang, K. (2010). Emerging challenges of microactuators for nanoscale positioning, assembly, and manipulation. *Journal of Manufacturing Science and Engineering*, 132:030917–1–030917–16.

Satir, P. and Christensen, S. (2008). Structure and function of mammalian cilia. *Histochemistry and cell biology*, 129(6):687–693.

Satir, P. and Sleigh, M. (1990). The physiology of cilia and mucociliary interactions. *Annual review of physiology*, 52(1):137–155.

Segal, J. and Dzik, W. (2005). Paucity of studies to support that abnormal coagulation test results predict bleeding in the setting of invasive procedures: an evidence-based review. *Transfusion*, 45(9):1404–1406.

Shah, A., Ben-Shahar, Y., Moninger, T., Kline, J., and Welsh, M. (2009). Motile cilia of human airway epithelia are chemosensory. *Science*, 325(5944):1131.

Shi, D., Komatsu, K., Uemura, T., and Fujimori, T. (2011). Analysis of ciliary beat frequency and ovum transport ability in the mouse oviduct. *Genes to Cells*, 16:282–290.

Shields, A. (2010). *Biomimetic Cilia Arrays - Fabrication, Magnetic Actuation, and Driven Fluid Transport Phenomena*. PhD thesis, University of North Carolina at Chapel Hill.

Shields, A., Fiser, B., and Evans, B. (2010). Biomimetic cilia arrays generate simultaneous pumping and mixing regimes. *Proceedings of the National Academy of Sciences of the United States of America*, 107(36):15670–15675.

Shih, C., Liu, T., and Huang, C. (2010). In vitro assessments of viscoelastic properties of fibrin clot by using acoustic radiation force on a solid sphere. *Ultrasonics Symposium (IUS), 2010 IEEE*, pages 479–482.

Singh, H., Laibinis, P., and Hatton, T. (2005). Synthesis of flexible magnetic nanowires of permanently linked core shell magnetic beads tethered to a glass surface patterned by microcontact printing. *Nano Lett*, 5(11):2149–2154.

Smith, D., Blake, J., and Gaffney, E. (2008). Fluid mechanics of nodal flow due to embryonic primary cilia. *Journal of The Royal Society Interface*, 5(22):567–573.

Spero, R., Sircar, R., Schubert, R., Taylor, R., Wolberg, A., and Superfine, R. (2011). Nanoparticle diffusion measures bulk clot permeability. *Biophysical Journal*, 101(4):943–950.

Stroock, A., Dertinger, S., Ajdari, A., Mezić, I., Stone, H., and Whitesides, G. (2002). Chaotic mixer for microchannels. *Science*, 295(5555):647.

Suh, J., Glander, S., Darling, R., Storment, C., and Kovacs, G. (1997). Organic thermal and electrostatic ciliary microactuator array for object manipulation. *Sensors and Actuators A: Physical*, 58(1):51–60.

Tanaka, Y., Okada, Y., and Hirokawa, N. (2005). Fgf-induced vesicular release of sonic hedgehog and retinoic acid in leftward nodal flow is critical for left–right determination. *Nature*, 435(7039):172–177.

Teran, J., Fauci, L., and Shelley, M. (2010). Viscoelastic fluid response can increase the speed and efficiency of a free swimmer. *Physical review letters*, 104(3):038101.

Tewari, P. and McLean, A. (1972). Temperature dependence of point of zero charge of alumina and magnetite. *Journal of Colloid and Interface Science*, 40(2):267–272.

Vadala, M., Rutnakornpituk, M., Zalich, M., Pierre, T. S., and Riffle, J. (2004). Block copolysiloxanes and their complexation with cobalt nanoparticles. *Polymer*, 45(22):7449–7461.

van Ewijk, G., Vroege, G., and Philipse, A. (1999). Convenient preparation methods for magnetic colloids. *Journal of Magnetism and Magnetic Materials*, 201(1-3):31–33.

van Oosten, C. L., Bastiaansen, C. W. M., and Broer, D. J. (2009). Printed artificial cilia from liquid-crystal network actuators modularly driven by light. *Nature Materials*, 8:677–682.

Venier, P., Maggs, A., Carlier, M., and Pantaloni, D. (1994). Analysis of microtubule rigidity using hydrodynamic flow and thermal fluctuations. *Journal of Biological Chemistry*, 269(18):13353.

Vilfan, M., Potočnik, A., and Kavčič, B. (2010). Self-assembled artificial cilia. *Proceedings of the National Academy of Sciences of the United States of America*, 107(5):1844–1847.

Vincent, J., Bogatyreva, O., Bogatyrev, N., Bowyer, A., and Pahl, A. (2006). Biomimetics: its practice and theory. *Journal of The Royal Society Interface*, 3(9):471.

Walser, M. (1961). Ion association. vi. interactions between calcium, magnesium, inorganic phospate, citrate and protein in normal human plasma. *The Journal of Clinical Investigation*, 40(4):723–730.

Wang, S., Huang, X., and Yang, C. (2011). Mixing enhancement for high viscous fluids in a microfluidic chamber. *Lab Chip*, 11:2081–2087.

Williams, O., Sharafkhaneh, A., Kim, V., Dickey, B., and Evans, C. (2006). Airway mucus: from production to secretion. *American Journal of Respiratory Cell and Molecular Biology*, 34(5):527.

Wilson, K., Harris, L., Goff, J., Riffle, J., and Dailey, J. (2002). A generalized method for magnetite nanoparticle stericc stabilization utilizing block copolymers containing carboxylic acids. *European Cells and Materials*, 3(Suppl. 2):206–209.

Wolberg, A., Gabriel, D., and Hoffman, M. (2002). Analyzing fibrin clot structure using a microplate reader. *Blood coagulation & fibrinolysis*, 13(6):533.

Worthington, W. and Cathcart, R. (1963). Ependymal cilia: distribution and activity in the adult human brain. *Science*, 139(3551):221.

Zhang, Y., Lo, C., Taylor, J., and Yang, S. (2006). Replica molding of high-aspect-ratio polymeric nanopillar arrays with high fidelity. *Langmuir*, 22(20):8595–8601.